

Artifact Suppression in cine DENSE MRI using Deep Learning

A dissertation presented to
the faculty of School of Engineering and Applied Science
University of Virginia

in partial fulfillment
of the requirements for the degree
Doctor of Philosophy

By

Mohamad Abdi

August 2022

Approval Sheet

This dissertation is submitted in partial fulfillment of the requirements for the degree of
Doctor of Philosophy

Mohamad Abdi

Author

The dissertation has been read and approved by the examining committee:

Frederick H. Epstein

Advisor

Craig H. Meyer

Kenneth C. Bilchick

Gustavo K. Rohde

Xue Feng

Accepted for the School of Engineering and Applied Science:



Jennifer L. West, School of Engineering and Applied Science
August 2022

Dedication

To my greatest supporters and the safest corners of my life: my sister Negar, and my parents Mandana, and Mahmoud.

Acknowledgements

I thank everyone who has been involved in this work.

Mohamad Abdi

Table of Contents

Approval Sheet.....	ii
Dedication.....	iii
Acknowledgements.....	iv
List of Figures.....	ix
List of Symbols.....	xv
List of Abbreviations.....	xviii
Abstract.....	xx
Chapter 1 : Introduction.....	23
1.1 Nuclear Magnetic Resonance.....	23
1.1.1 Gradient fields.....	25
1.2 Cardiac Magnetic Resonance.....	26
1.3 Myocardial Strain CMR.....	26
1.4 Myocardial Strain Measurement using DENSE.....	28
1.4.1 Mathematical description of the DENSE signals.....	29
1.4.2 Artifact-generating echoes in DENSE.....	31
1.4.3 Phase-cycling method.....	32
1.4.4 Through-plane dephasing.....	33
1.4.5 Displacement measurement.....	34
1.4.6 Background phase corrections.....	34
1.4.7 Displacement encoding methods.....	35
1.4.8 Image Analysis.....	37

1.5 Breath-hold DENSE acquisitions	38
1.6 Free-breathing DENSE	40
1.6.1 Diaphragm navigator-gated DENSE	40
1.6.2 Free-breathing DENSE using match-making and self-navigation	42
1.7 Respiratory motion artifacts in DENSE MRI	45
1.8 Deep learning	46
1.9 Statement of research objectives	48
1.10 References	49
Chapter 2 : Suppression of Artifact-Generating Echoes in Cine DENSE Using Deep Learning.	57
2.1 Abstract	57
2.2 Introduction	58
2.3 Methods	59
2.3.1 U-Net design.....	60
2.3.2 Training dataset	61
2.3.3 Determination of the optimal training domain	62
2.3.4 Data augmentation with remodulation of the displacement-encoding frequency	63
2.3.5 DENSE artifact suppression network.....	64
2.3.6 Comparison to k-space zero-filling	65
2.3.7 Evaluation of the method using DENSE data without phase-cycling.....	65
2.4 Results	66
2.4.1 k-t is the optimal training domain	66
2.4.2 Data augmentation with remodulation of the displacement-encoding frequency enhances T ₁ -echo suppression.....	67
2.4.3 DAS-Net outperforms k-space zero-filling	68
2.4.4 Strain data from non-phase-cycled images processed by DAS-Net are in close agreement with ground-truth	70

2.5 Discussion.....	71
2.6 References	74
Chapter 3 : Compensation for Respiratory-Motion-Induced Signal Loss and Phase Corruption in Free-breathing Self-navigated Cine DENSE using Deep Learning.....	81
3.1 Abstract	81
3.2 Introduction	82
3.3 Theory	84
3.4 Methods.....	88
3.4.1 Phantom Experiments.....	88
3.4.2 Bloch-equation DENSE simulations incorporating cardiac and respiratory motion....	90
3.4.3 Acquisition of training data for the convolutional neural network	94
3.4.4 Architecture of the deep learning model	94
3.4.5 Training of the constant-phase correction deep learning model (DENSE-RESP-NET)	95
3.4.6 Testing of the methods using prospectively acquired free-breathing DENSE.....	97
3.4.7 Evaluation of the deep learning model.....	98
3.5 Results	99
3.5.1 Validation of the DENSE signal model that accounts for the effects of respiratory motion using a moving, non-deformable phantom.....	99
3.5.2 Simulated respiratory motion-induced artifacts in DENSE images of a deforming digital phantom and their correction using the proposed model	99
3.5.3 The deep learning model can correct the respiratory motion-induced artifacts in self-navigated free-breathing DENSE	100
3.6 Discussion	104
3.7 Conclusion.....	107
3.8 References	107
Chapter 4 : Compensation for respiratory-induced stimulated-echo artifacts in free-breathing adaptive-matchmaker DENSE applied in healthy subjects and heart failure patients.....	111

4.1 Abstract	111
4.2 Introduction	111
4.3 Methods	113
4.3.1 Prospective in vivo cine DENSE imaging.....	113
4.3.2 Evaluation of deep learning model on adaptive free-breathing cine DENSE	114
4.4 Results	115
4.5 Discussion	120
4.6 Conclusion.....	122
4.7 Reference.....	123
Chapter 5 : Summary, Discussion, Limitations, Conclusion	125
5.1 Summary of the work	125
5.2 Discussions	127
5.2.1 Artifact-generating T ₁ -echo.....	127
5.2.2 Suppression of T ₁ -echo using DAS-Net.....	130
5.2.3 Respiratory motion-induced phase shifts	132
5.2.4 Motion compensations with DENSE-RESP-NET.....	133
5.3 Limitations of this work	135
5.4 Future directions.....	137
5.5 Conclusion.....	138
5.6 References	138
Appendix: List of Publications	140

List of Figures

Figure 1.1 – Diagram showing the components of cine DENSE acquisitions using spiral trajectories. Cine DENSE is electrocardiogram-gated. Upon the detection of R-wave, saturation pulses are applied to null the signal from fat followed by a set of displacement encoding pulses. The acquisition module consists of a small flip angle RF pulse to tip down a small portion of the position-modulated longitudinal magnetization onto the transverse plane and generate the stimulated echo followed by a displacement rephrasing gradient and spiral readout gradients. ... 29

Figure 1.2 – The T_1 -echo suppression using phase-cycling method and phase decoding of the resulting stimulated echoes. A) For each displacement measurement, the phase-cycled images are acquired where the stimulated echo phase is shifted by 180° . For each measurement, the magnitude and phase images in addition to the real (instead of complex) k-space data are shown. The subtraction of the k-space images leads to suppression of the T_1 -echo (marked by yellow arrows) and artifact-free stimulated echo images. B) The raw stimulated echo phase is processed by the inverse of the displacement encoding matrix to calculate the back-ground phase corrected tissue displacements. 36

Figure 1.3 – Analysis of DENSE images include segmentation for a region-of-interest, un-wrapping of the phase information within the region-of-interest to compute the true phase values, and interpolation of the displacement field using the true phase values. The displacement fields are then used to calculate strain data. Circumferential strain (E_{cc}) shown in panels J and L is the most common strain parameter used for assessment of cardiac function with DENSE. 38

Figure 1.4 – Example DENSE magnitude and phase images from breath-hold (A) and free-breathing (B) acquisitions 39

Figure 1.5 – Diaphragm navigator-gated DENSE enables free-breathing acquisitions. Additional coronal (A) and sagittal (B) scout images are acquired to find the position of diaphragm. The navigator bands are placed on the right dome of diaphragm (marked by yellow arrows in A and B). A scout scan is performed to track the position of right dome. A small window at end-expiration position of the diaphragm is used to accept or reject the acquired free-breathing data. Data that fall within the accept widow is used for image reconstruction. One limitation of this method is the variable image quality. Example images are shown in panels E and F illustrating this limitation. 41

Figure 1.6 – Diagram showing the general approach for motion estimation using self-navigation. Data from different heartbeats are assigned to different motion states. Multiple low-resolution image navigators are reconstructed from data within each motion states. The image navigators are used in rigid registration algorithm to estimate the motion between different states and between different navigators within each state. The estimated motion is used for motion compensation. 43

Figure 1.7 – Two examples showing motion compensation using self-navigation in DENSE. The estimated motion from self-navigation is used to correct the linear phase errors in the first and the second acquisitions after suppression of the T_1 -echo. While blurring/ghosting artifacts are corrected in the first acquisitions, the motion compensation failed to correct the all types of artifacts including the signal loss in the second acquisition. This example demonstrates that motion compensations should be extended to account for all types of respiratory motion artifacts in stimulated echo imaging. 44

Figure 1.8 - Example magnitude images, phase image, and k-space showing three types of respiratory-motion-induced artifacts in DENSE on a phantom. 1) Stripe artifacts (A-C) are caused by imperfect suppression of the T_1 -echo due to motion. 2) Position shift of tissue leads to approximately linear phase errors in k-space. In segmented DENSE, liner phase errors manifest in the form of blurring/ghosting artifacts (E). 3) The encoding of the tissue motion to the phase of the stimulated echo leads to phase shifts in image domain and constant phase errors in k-space. In segmented DENSE, this manifests in the form of signal loss (H) and phase corruptions (I) in image domain. 46

Figure 2.1 - Diagram illustrating the use of deep learning to suppress the artifact-generating T_1 -echo (T_1E) in DENSE images. Artifact-free images with suppressed T_1 -echoes obtained from complementary phase-cycled DENSE acquisitions were used to train the DAS-Net. Once trained, the DAS-Net takes non-phase-cycled images as input, and its output is a DENSE image where the T_1 -echo and associated artifacts have been suppressed. STE: Stimulated echo. 60

Figure 2.2 - U-Nets were trained using DENSE data formatted in k-t planes (UN_{kt}), spatial planes (UN_{xy}), and k-space planes (UN_{kk}). (A) An example showing DENSE magnitude and phase images, the k-space magnitude data, and k-t planes after application of the UN_{kt} , UN_{xy} and UN_{kk} U-Nets. (B) Bar-plots and error bars (representing the standard deviation) of RMSE and SSIM computed from the output of each U-Net and the ground-truth data for end-systolic images of $N=30$ test datasets show that the UN_{kt} network provides the best performance. 67

Figure 2.3 - Demonstration of data augmentation using remodulation of the displacement-encoding frequency. (A) Authentic data are shown in left column of (A), acquired with an encoding frequency of 0.06 cycles/mm. Using the frequency remodulation method, the authentic data in the left column was phase remodulated to generate the synthetic image shown in the middle column, with encoding frequency of 0.10 cycles/mm. Compared to the authentic image, the synthetic image are reasonably realistic. (B) Training a U-Net with 30 authentic and 30 augmented datasets (UN_{30A}) results in lower RMSE and higher SSIM than training with only 30 authentic datasets (UN_{30}), and provides similar RMSE and SSIM as training with 60 authentic datasets (UN_{60}). The error bars represent standard deviation. 68

Figure 2.4 - The DAS-Net is effective for suppression of the T_1 -echo. In (A), example magnitude images, phase images, k-space data, and k-t planes are shown for input images, ground truth using phase-cycling, DAS-Net, and images after k-space zero-filling. As observed in (A) and quantified for all datasets in (B), the DAS-Net provided lower RMSE and higher SSIM values than zero-filling. 69

Figure 2.5 - Circumferential strain measurements are similar for non-phase-cycled DENSE images using DAS-Net for T_1 -echo suppression (8-heartbeat protocol) and phase-cycled DENSE images (14-heartbeat protocol). (A) Example magnitude images, phase images, and k-space data are shown for the 8-heartbeat protocol without DAS-Net processing (8-HB protocol), the 8-heartbeat protocol with DAS-Net processing (8HB DAS-Net processed), and the 14-heartbeat protocol with phase-cycling (14-HB protocol). The end-systolic circumferential strain maps of the DAS-Net processed and the 14-heartbeat protocol data are shown in the bottom row. (B) Multiphasic segmental circumferential strain-time curves of the DAS-Net processed 8-HB protocol and the 14-HB protocol images are shown. (C) Bland-Altman analysis shows good agreement between the 8HB DAS-Net processed and 14-HB protocols for end-systolic segmental circumferential strain (E_{cc}) from the six test subjects..... 70

Figure 2.6 - (A) Example multiphasic segmental radial strain (E_{rr})-time curves from the DAS-Net processed 8-HB protocol and the 14-HB protocol are shown, as are example end-systolic radial strain maps. (B) The Bland-Altman analysis for segmental end-systolic E_{rr} for the six test subjects is shown..... 74

Figure 3.1 - Effect of respiratory motion on the DENSE signal. (A) Schematic diagram showing the left and right ventricles in a short-axis view. (B) In the absence of respiratory motion, cardiac contraction causes displacement of myocardial tissue and this displacement, $\Delta r = \Delta rC$, is encoded into the phase of the DENSE stimulated-echo. During a free-breathing acquisition (C), the displacement of myocardial tissue is due to both heart deformation and respiratory motion. There are two types of respiratory motion: (1) that which changes the heart's position prior to displacement encoding, $\Delta rR1$, and that which occurs between displacement encoding and readout, $\Delta rR2$. $\Delta rR1$ leads to a position shift of the magnetization amplitude, while $\Delta rR2$ gets encoded into the phase of the stimulated echo in addition to leading to a position shift of the magnetization amplitude..... 85

Figure 3.2 - Respiratory motion encoded into the phase of the stimulated-echo in segmented DENSE leads to signal loss and phase corruption artifacts. The respiratory-motion-induced phase shift leads to signal loss and phase corruptions in segmented DENSE acquisitions where different segments are impacted by different respiratory-motion-induced phase shifts..... 87

Figure 3.3 - Phantom experiment and Bloch equation simulations used to validate the DENSE motion model that accounts for breathing. Diagrams illustrating (A) the phantom experiment used to validate the DENSE motion model where the phantom can be moved in the scanner between the displacement-encoding pulses and the readout, and (B) the modules embedded in a Bloch-equation-based DENSE simulator, including the simulation of cardiac motion and the two types of respiratory motion..... 89

Figure 3.4 - Experimental and simulation results demonstrating that motion in the displacement-encoding direction is encoded into the phase of the stimulated echo and, when the motion is different for different segments, causes signal loss and phase corruption. Phase correction using the signal model of equation (3.4) and the known motion can correct the artifacts. (A) A diagram showing the acquisition of four k-space segments where $\Delta rR2 = 0$ mm for segments one and three and $\Delta rR2 = 35$ mm for segments two and four. (B) DENSE images corresponding to the conditions shown in panel (A) where the object motion is orthogonal and parallel, respectively,

to the displacement-encoding direction. Different types of artifacts are observed when motion is orthogonal or parallel to the displacement-encoding direction, and per-segment linear and constant phase corrections applied in k-space can recover artifact-free stimulated-echo images from the motion-corrupted versions..... 91

Figure 3.5 - Bloch equation simulations using a deforming heart motion phantom demonstrate respiratory-motion induced DENSE artifacts and their correction using the DENSE motion model of Equations (3.3), (3.4), and (3.5). (A) The computational deforming phantom consists of a deforming annulus where the concentric circles define the epicardial and endocardial borders in the heart short-axis view and a static component. (B-F) The motion corrupted DENSE images were simulated using the Bloch equations with typical DENSE sequence parameters and the incorporation of motion. Motion correction based on the known motion and the linear (corresponding to $\Delta rR1$ and $\Delta rR2$) and constant corrections (corresponding to $\Delta rR2$) of Equations (3.4) and (3.5) recover images that are nearly identical to the reference images and preserve the phase-based measurement of heart contraction..... 93

Figure 3.6 - Diagram illustrating the generation of phase-shift-corrupted DENSE images for training a convolutional neural network, DENSE-RESP-NET, to correct the signal loss and phase corruption artifacts in self-navigated free-breathing cine DENSE. Respiratory motion was simulated using sine waves with magnitude and frequency similar to physiological values. The constant phase errors were calculated and applied on per-segment breath-hold DENSE images. The motion-corrupted images were generated by summing the manipulated per-segment images according to equation (3.6). The motion-corrupted and the corresponding breath-hold images were used to train an instance of U-Net with recurrent connections and long-short term memory cells. 96

Figure 3.7 - **DENSE-RESP-NET compensates for the signal loss and phase corruption in self-navigated free-breathing cine DENSE.** Example magnitude and phase images of averaged free-breathing, self-navigated free-breathing, DENSE-RESP-NET processed and ground-truth breath-hold cine DENSE images are shown for an end-systolic frame and a diastolic frame. DENSE-RESP-NET effectively corrects the signal loss and phase corruption, and the results are more pronounced in the diastolic frame where $\Delta rR2$ is greater..... 101

Figure 3.8 - Diastolic phase SNR demonstrates improved image quality in DENSE-RESP-NET corrected self-navigated images compare to uncorrected self-navigated and averaged free-breathing images. Breath-hold DENSE images represent the reference standard. Bar plots and error bars show the mean and standard deviation of the phase SNR calculated according to equation (3.7). The phase SNR values were 8.75 ± 2.67 , 9.07 ± 3.06 , 6.38 ± 2.77 , and 1.29 ± 0.52 (p-value < 0.001) for the breath-hold, the DENSE-RESP-NET self-navigated, the self-navigated free-breathing (without DENSE-RESP-NET), and the averaged free-breathing images respectively. 102

Figure 3.9 - Strain measurement in a healthy subject shows good agreement between the DENSE-RESP-NET corrected data compared to the breath-hold data, whereas the self-navigated and averaged free-breathing data are unreliable in diastole. A) Segmental circumferential strain (E_{cc})-time curves, and B) global circumferential strain rate-time curves of the example in Figure

3.7 are shown for averaged free-breathing, self-navigated free-breathing, DENSE-RESP-NET processed and ground-truth breath-hold images. 103

Figure 3.10 - Bland-Altman analysis of segmental circumferential strain and global circumferential strain rate of the DENSE-RESP-NET corrected data shows improved accuracy and a better agreement with the breath-hold (BH) DENSE data compared to uncorrected self-navigated free-breathing data (self-NAV FB). 104

Figure 4.1 - Example magnitude and phase images from self-navigated adaptive free-breathing (without DENSE-RESP-NET processing), DENSE-RESP-NET processed, diaphragm navigator-gating, reference breath-hold images are shown from a healthy human subject (A) and heart-failure patient (B). While end-systolic images show small improvement in DENSE-RESP-NET processed images compared to self-navigated adaptive data, improvement are significant for the diastolic images. 116

Figure 4.2 – Bar plots of diastolic phase SNR measured according to Equation (4.1) on patients and healthy-subject images. The DENSE-RESP-NET shows significantly better phase SNR compared to the self-navigated adaptive and diaphragm navigator-gated images and comparable values compared to reference breath-hold images. The error bars indicate the standard deviations. 117

Figure 4.3 – Pearson’s correlation and Bland-Altman analysis show better agreements for segmental circumferential strain (E_{cc}) measured on DENSE-RESP-NET processed images compared to the self-navigated adaptive and diaphragm navigator-gated data in healthy subjects. 118

Figure 4.4 – Segmental circumferential strain (E_{cc}) measurements on heart-failure patients show better agreements between DENSE-RESP-NET processed images and reference data compared to those of self-navigated adaptive and diaphragm navigator-gated data using both Pearson’s correlation and Bland-Altman analysis. 119

Figure 4.5 – DENSE-RESP-NET significantly improved diastolic measurements. Global early diastolic circumferential strain rate from DENSE-RESP-NET processed data show significantly better agreement compared to those of self-navigated adaptive and diaphragm navigator-gated images on healthy subjects. Self-navigated adaptive images (with or without DENSE-RESP-NET processing) provided more accurate segmental systolic circumferential strain measurements compared to diaphragm navigator-gated images. 120

Figure 4.6 – Evaluation of global early diastolic circumferential strain rate on heart-failure patient demonstrates the improved accuracy and agreement in favor of DENSE-RESP-NET compared to other methods. 121

Figure 5.1 – Suppression of the T_1 -echo is essential prior to processing the DENSE images as T_1 -echo adversely affects the displacement measurements. Since the source of T_1 -echo is the relaxation of the longitudinal magnetization, it grows over time during each cardiac cycle and because of this, diastolic images are more affected. Examples of strain measurement from DENSE image before and after T_1 -echo suppression using phase-cycling and the corresponding magnitude and phase images from three different cardiac phases are shown. 128

Figure 5.2 – Example magnitude and phase images in addition to k-space data showing the signal separation using ED-PCA method applied on non-phase-cycling images. The performance of ED-PCA is sub-optimal compared to phase-cycling method. 129

Figure 5.3 – Motion from various sources could leads to imperfect suppression of the T_1 -echo using phase-cycling in diaphragm navigator-gated images. DAS-Net could potentially be used after phase-cycling subtraction to suppress the residual T_1 -echo. Example diastolic images from a diaphragm navigator-gated data shows stripe artifacts - possibly due to imperfect phase-cycling subtractions. 131

Figure 5.4 – DAS-Net eliminates the need for phase-cycling acquisitions. DENSE images used to train DAS-Net were acquired using through-plane dephasing gradient. Through-plane dephasing method cannot be used for three-dimensional (2-dimensional in-plane and one-dimensional through-plane) displacement measurement in DENSE. T_1 -echo suppression using DAS-Net is shown for a DENSE image acquired without the through-plane dephasing in addition to T_1 -echo suppression using phase-cycling. 132

Figure 5.5 – Signal loss and phase corruption can affect the diaphragm navigator-gated images as well as self-navigated adaptive free-breathing images. Example magnitude and phase images affected by these artifacts and the application of DENSE-RESP-NET for motion compensation. 135

List of Symbols



p	probability
E	energy state of nuclear spins
k	Boltzmann constant
T	absolute temperature
\hbar	reduced Plank constant
γ	gyromagnetic ratio of protons
B_0	static magnetic field
ω_L	Larmor (angular) frequency
M	magnetization
M_{xy}	in-plane magnetization
M_z	longitudinal magnetization
M_0	magnetization at thermal equilibrium
T_1	longitudinal (spin–lattice) relaxation time
T_2	transverse (spin–spin) relaxation time
G_r	magnetic gradient field
α	flip angle
k_e	displacement encoding frequency
k_e	through-plane dephasing frequency

Δr^c	myocardial displacement
ϕ_b	stimulated echo background phase
k	Spatial frequency variable
m_{STE}	magnitudes of stimulated echo
m_{T_1E}	magnitudes of T ₁ -echo
M_{STE}	Fourier transforms of stimulated echo
M_{T_1E}	Fourier transforms of T ₁ -echo
c_r	displacement-encoding frequency remodulation constant
E_{cc}	circumferential strain
E_{rr}	radial strain
Δr^{R_1}	in-plane translation of the myocardium due to breathing immediately prior to the application of the displacement-encoding pulses
Δr^{R_2}	in-plane displacement due to breathing during the time between application of the displacement-encoding pulses and the readout
\hat{s}_{STE}	displacement-encoded stimulated-echo affected by respiratory motion
$m(k)$	k-space representations of the stimulated-echo
\hat{s}_{STE}^c	stimulated echo affected by per-segment respiratory-induced constant phase shifts
E_t^c	respiratory motion-induced constant phase error
T_R	repetition time of pulse sequence
T_E	echo time of pulse sequence
t	time

r spatial position
 W displacement encoding matrix

List of Abbreviations



NMR	nuclear magnetic resonance
MRI	magnetic resonance imaging
LGE	late-gadolinium enhanced
DENSE	displacement encoding with stimulated-echoes
RF	radiofrequency
STE	stimulated echo
ANOVA	analysis of variance
SSIM	structural similarity index
ED-PCA	eigen-decomposition using principal component analysis
CNN	convolutional neural network
HARP	harmonic phase
SNR	signal to noise ratio
DAS-Net	DENSE artifact suppression network
HB	heartbeat
ste-iNAVs	stimulated echo-based image navigators
ECG	electrocardiogram
FOV	field-of-view

LSTM	Long-short term memory
3T	3 Tesla
1.5T	1.5 Tesla
EF	ejection fraction

Abstract

Myocardial strain imaging adds diagnostic and prognostic value in the assessment of many types of heart disease. Cine displacement encoding with stimulated echoes (DENSE) is among the most accurate and reproducible myocardial strain imaging methods with growing clinical applications. This dissertation research seeks to develop methods to shorten the scan time for cine DENSE and to develop free-breathing cine DENSE methods, both of which would facilitate greater clinical usage of the method.

During DENSE data acquisition, a signal due to T_1 -relaxation (T_1 -echo) is simultaneously acquired along with the displacement-encoded stimulated echo which generates stripe artifacts and leads to inaccurate strain measurement. The T_1 -echo is typically suppressed by acquiring additional phase-cycled data, which despite its effectiveness, leads to increased scan time.

In addition to the T_1 -echo, respiratory motion also leads to undesired artifacts. The standard DENSE image acquisition protocol requires breath-holding to avoid respiratory motion artifacts, and this can be challenging for heart failure and pediatric patients and for those under sedation. This creates a broad need for free-breathing methods. In free-breathing cine DENSE acquisitions, three types of artifacts arise: (a) those due to incomplete suppression of the T_1 -echo, (b) those due to (approximately) rigid translation of the tissue, and (c) encoding of breathing-induced tissue motion into the phase of the stimulated-echo. Previously, methods were developed to compensate for the first and the second types of artifacts in DENSE. The third type of artifact causes unique

respiratory-induced k-space phase errors which correspond to phase shifts in the image domain and lead to signal loss and phase corruption artifacts.

A deep learning model was developed for suppression of the artifact-generating T_1 -echo in cine DENSE for the purpose of eliminating the phase-cycling acquisitions and reducing the scan time limitation. A U-Net (DAS-Net) was trained to suppress the artifact-generating T_1 -echo using phase-cycled data as the ground truth. A data augmentation method was developed that generates synthetic DENSE images with arbitrary displacement encoding frequencies to suppress the T_1 -echo modulated for a range of frequencies. DAS-Net was evaluated on non-phase-cycling cine DENSE images from healthy subjects. Comparisons between DAS-Net processed images and the corresponding phase-cycling reference data using signal-to-noise ratio and strain measurements demonstrated that DAS-Net provides an effective alternative approach for suppression of the artifact-generating T_1 -echo in DENSE MRI, enabling a 42% reduction in scan time compared to DENSE with phase cycling.

A new model was introduced that describes artifacts due to encoding of respiratory motion into the phase of the stimulated echo. Phantom experiment and Bloch-equation simulations were performed to validate the model. The model was used along with the simulation of respiratory motion to generate synthetic images with phase shift artifacts to train a U-Net, DENSE-RESP-NET for compensation of signal loss and phase corruption artifacts. Evaluations of the DENSE-RESP-NET on self-navigated free-breathing cine DENSE from healthy volunteers showed that the DENSE-RESP-NET is an effective method to compensate for breathing-associated signal loss and phase corruption artifacts.

The developed motion compensation method, DENSE-RESP-NET, was used and evaluated in concert with adaptive free-breathing acquisitions and self-navigation applied on

healthy volunteers and heart disease patients. Assessment of motion compensated images for strain and signal-to-noise ratio demonstrated that the proposed motion compensation method outperforms the conventional diaphragm navigator-gated method and provides reliable free-breathing cine DENSE acquisitions for measurement of systolic and diastolic parameters.

Chapter 1 : Introduction

Magnetic resonance imaging (MRI) is a non-invasive imaging technique used to study the anatomy and function of living tissue. Advantages of MRI compared with other non-invasive techniques such as x-ray computed tomography (CT), positron emission tomography (PET), and ultrasound imaging techniques are the absence of radiation risks, better soft-tissue contrast, flexibility for arbitrary imaging plane, high resolution and high signal-to-noise ratio images, and flexibility for imaging different mechanism (relaxometry, displacement, diffusion, perfusion, blood oxygen level-dependent, etc.) in tissue.

MRI is based on nuclear magnetic resonance (NMR) where certain atoms with non-zero nuclear magnetic moment are perturbed by a small oscillating magnetic field (radiofrequency pulses) with a certain frequency characteristic when placed in a strong static magnetic field (B_0 field). The advances during the 1970s with the utilization of magnetic field gradients enabled localization of NMR signal and production of MR images¹.

1.1 Nuclear Magnetic Resonance

The NMR phenomenon only occurs for atoms with odd numbers of protons and/or neutrons where the nuclear magnetic moment is non-zero; these atoms are said to have spins. The probability of the spins being at a specific energy state follows the Boltzmann distribution.

$$p_i \propto e^{-\frac{E_i}{kT}} \quad (1.1)$$

p_i is the probability, E_i is the energy level associated with the spin state, k is the Boltzmann constant, and T is the absolute temperature. In the absence of the static magnetic field B_0 , the

energy level of the system is zero and all the spins are in a single energy state. The magnetic moments of the spins cancel out and the net magnetization is zero. When the system is placed in the static magnetic field B_0 , the energy state of the system splits into multiple levels (the Zeeman splitting). For those nuclei with $\frac{1}{2}$ -spin, the energy level splits in two equal states in magnitude, $\frac{1}{2}\gamma\hbar B_0$, but different in signs, where γ is the gyromagnetic ratio, \hbar is the reduced plank constant, and B_0 is the strength of the static magnetic field B_0 . According to the Boltzmann equation (1.1), the smaller energy state is preferred for the spins to occupy. The ratio of spins that occupy the lower energy state (N_1) to those in the higher energy state (N_2) is defined by the Boltzmann factor in equation (1.2).

$$\frac{p_{-\frac{1}{2}}}{p_{+\frac{1}{2}}} = \frac{N_1}{N_2} = e^{\frac{\Delta E(=\gamma\hbar B_0)}{kT}} \quad (1.2)$$

The difference between N_1 and N_2 creates a net magnetization along the static magnetic field. The net magnetization is denoted by M_0 at thermal equilibrium where the temperature is constant spatially and temporally. The magnetization vector has a natural frequency defined by the Larmor equation in (1.3).

$$\omega_L = \gamma B \quad (1.3)$$

The Larmor frequency depends on the magnitude of the external magnetic field experienced by the nuclei sample (and other factors such as the chemical environment and the magnetic properties of the nuclei). When a weak (in magnitude compared to the static magnetic field) oscillating magnetic field (usually called radiofrequency or RF pulse) with a frequency set at the Larmor frequency is applied on the nuclei sample, the magnetization starts to align with the oscillating field, the phenomena which is known as NMR. With long enough duration of oscillating field (RF pulse), the magnetization can be tipped down onto the transverse plane. When the oscillating field is switched off, the magnetization starts to relax back to its original state, M_0 ; This

process is called relaxation. The transverse and longitudinal components of the magnetization decay and relax respectively with different time constant, the T_2 and T_1 , known as transverse relaxation time and the longitudinal relaxation time respectively. The macroscopic behavior of the magnetization is described using the Bloch equation described in (1.4).

$$\frac{d}{dt}\vec{M}(t) = \gamma (\vec{M}(t) \times B(t)) - \frac{1}{T_2} M_{xy}(t) - \frac{1}{T_1} (M_z(t) - M_0) \quad (1.4)$$

$M(t)$ denotes the magnetization with respect to time, $B(t)$ is the external magnetic field applied on the sample of nuclei, $M_{xy}(t)$ and $M_z(t)$ are the transverse and longitudinal components of magnetization vector respectively.

1.1.1 Gradient fields

Gradient fields are used to link the dynamic of the magnetization described by Bloch equation to its position. In classical description of NMR, the magnetization precesses at a frequency determined by the Larmor equation around the axis defined by the direction of static magnetic field. Gradient fields point toward the static magnetic field and change linearly in with respect to position. This creates the linear magnetic gradient from one end of the material to another end. Magnetization at each point in the material precesses at a frequency different than the neighboring point. With a gradient field, the procession frequency of magnetization at different position can be described in equation 1.5).

$$\omega_L(r) = \gamma(B_0 + G_r r) \quad (1.5)$$

G_r is the gradient field linearly varying with respect to position r . Gradient fields are used for (1) selective excitations where the oscillating field resonates with magnetizations at certain positions, (2) localization of NMR signal, (3) creating dephasing among magnetization at different positions and etc.

1.2 Cardiac Magnetic Resonance

Cardiac magnetic resonance provides non-invasive methods to assess heart and vascular anatomy and function. These methods are used to assess ventricular function and structure, blood hemodynamic, myocardial tissue composition, microstructure, perfusion, coronary microvascular function and etc.

Late gadolinium enhancement (LGE) is routinely used to measure myocardial viability through the assessment of myocardial scar formation and regional myocardial fibrosis after myocardial infarction². Myocardial relaxometry using T_1 , T_2 , and T_2^* mapping is used to assess the presence of diffuse interstitial fibrosis in ischemic and nonischemic cardiomyopathy³, image myocardial edema⁴, and measure iron overload⁵ respectively. Diffusion-weighted and diffusion tensor imaging provide microstructural information myocardial fibers through directional measurement of water motion. This information plays a key role to link the function and structure in various cardiac diseases⁶. Myocardial perfusion imaging enables the assessment of patient condition in coronary artery disease. Velocity-encoded MRI provides information about myocardial hemodynamics which has clinical implications for various cardiac diseases.

1.3 Myocardial Strain CMR

Various cardiac disease can adversely affect the cardiac function. Abnormalities in cardiac function can negatively affect other systems in the body. The precise assessment of cardiac function is important for diagnosis and treatment of diseases. Cardiac MRI provide high resolution and signal-to-noise ratio cross-sectional images and has shown to be a powerful tool for such assessments⁷.

Quantification of cardiac function using MRI has primarily been focused on global parameters derived from anatomical information as indicator of systolic function. Specifically, ejection fraction measurements as the change in ventricular volume during cardiac cycle has been used as an indicator of cardiac function and for classification of heart-failure types⁸. However, there are limitations with ejection fraction. First, ejection fraction as a global parameter does not reflect the regional changes in cardiac function which may have important clinical implications. Second, ejection fraction is a measure of systolic function. Several preliminary studies have shown the value of diastolic function assessments⁹⁻¹¹. Third, while many heart-failure patients have reduced ejection fraction, as many as half of patients presenting with symptoms of heart failure have an essentially preserved ejection fraction¹².

Myocardial strain measurements are more likely to reflect subtle changes in the myocardial contraction pattern due to local tissue alterations than global measures based on volume change. In addition, strain measurement provides information about temporal variations in cardiac function which enables for more comprehensive assessment during both systole and diastole. In addition, fusion of regional strain measurements with other kinds of imaging modalities may help to better distinguish different kinds of failures in cardiac function and guide the therapies¹³.

Conventional cross-sectional methods used to image regional strain include echocardiography and cardiac MRI. Echocardiography of the heart is widely used for assessing global and regional cardiac function. A strength of echocardiography is its relatively high temporal resolution. However, it has important drawbacks, including its dependence on operator experience, and limited acoustic windows due to the presence of bone and lung.

Myocardial wall motion assessment using feature tracking in steady-state free precession MRI provides global and regional strain analysis. While they provide good images of the moving

heart wall, motion analysis is primarily based on inner and outer boundaries as there is little intrinsic structure within the myocardial wall. MRI-based strain imaging methods are those based on magnetization tagging, tissue phase mapping, displacement-encoded, and strain-encoded imaging.

1.4 Myocardial Strain Measurement using DENSE

Displacement encoding with stimulated echoes (DENSE) provide direct displacement measurement of myocardial contraction by encoding the motion into the phase of the stimulated echo^{14,15}. The nature of this method provides accurate measurement of myocardial displacement and strain and studies has shown that DENSE measurements are highly reproducible^{16,17}. In addition, recent advances in post-processing algorithms provided automatic analyses of DENSE images¹⁸.

DENSE employs electrocardiogram-gated segmented acquisitions using spiral trajectories¹⁹. Figure 1.1 shows a diagram of spiral DENSE acquisition. Upon the detection of R-wave, a set of displacement-encoding pulses are applied following a fat-saturation module. The displacement encoding pulses modulates the location into the longitudinal magnetization. The readout module consists of small flip angle RF pulse and displacement rephrasing gradient followed by spiral readout gradient pulses. The RF pulse tips down a portion of modulated longitudinal magnetization onto the transverse plane and generates the stimulated echo. The displacement rephrasing gradient restore the phase that was modulated to the magnetization during the encoding module with respect to the location.

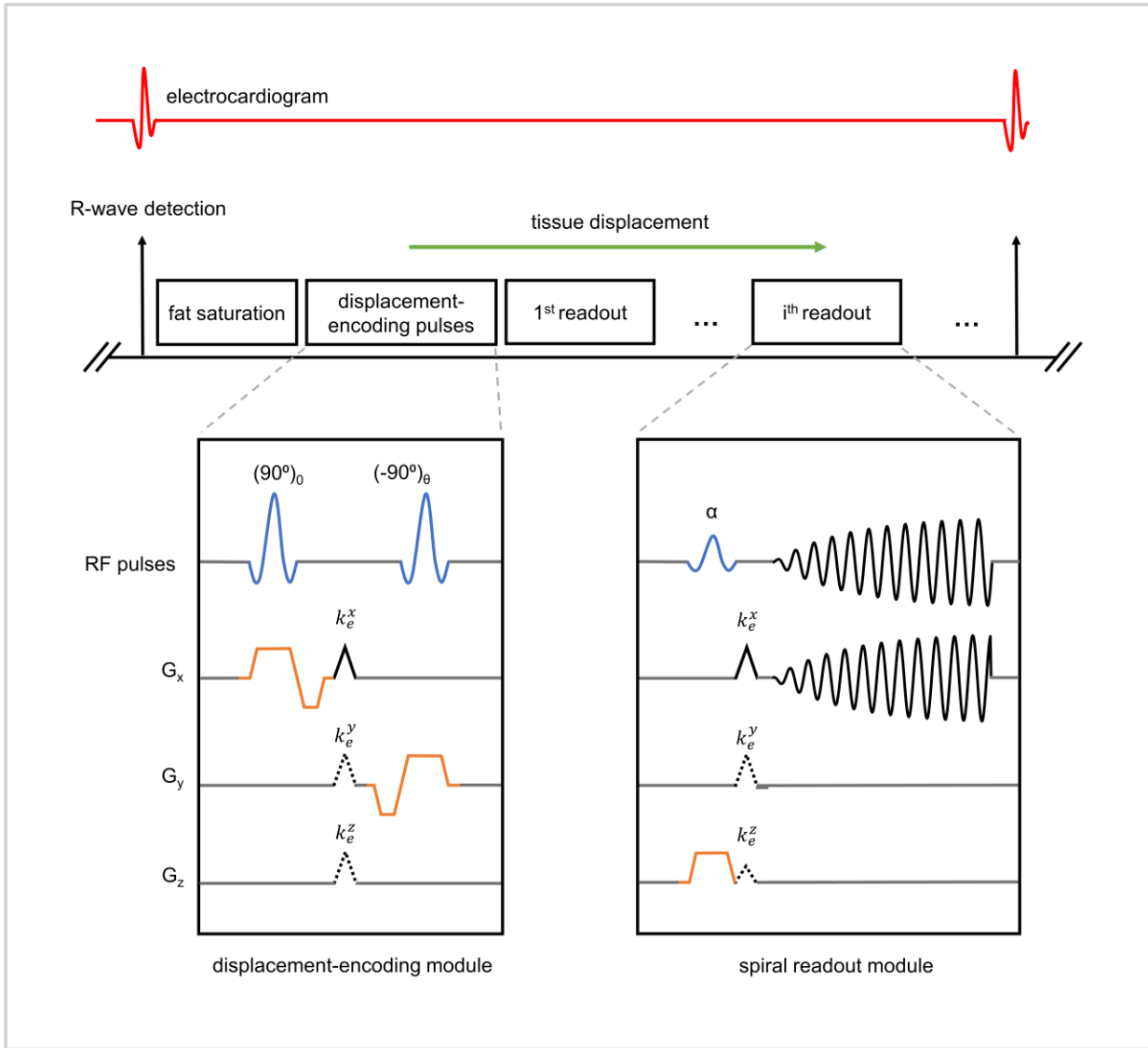


Figure 1.1 – Diagram showing the components of cine DENSE acquisitions using spiral trajectories. Cine DENSE is electrocardiogram-gated. Upon the detection of R-wave, saturation pulses are applied to null the signal from fat followed by a set of displacement encoding pulses. The acquisition module consists of a small flip angle RF pulse to tip down a small portion of the position-modulated longitudinal magnetization onto the transverse plane and generate the stimulated echo followed by a displacement rephrasing gradient and spiral readout gradients.

1.4.1 Mathematical description of the DENSE signals

Assuming thermal equilibrium prior to the application of the displacement encoding module, the magnetization only has a longitudinal component as described in equation (1.6).

$$M_z(r, t) = M_0 \quad (1.6)$$

The first 90-degree RF pulse tip down the magnetization onto the transverse plane. The displacement encoding gradient (G_e) corresponding to a displacement encoding frequency $k_e = \frac{\gamma}{2\pi} G_e t$ generates a position dependent phase shift on the transverse magnetization as described in equation (1.7).

$$M_{xy}(r, t) = M_0 e^{i2\pi\langle k_e, r \rangle} \quad (1.7)$$

γ is the gyromagnetic ratio of proton, and G_e is the gradient pulse magnitude, and $\langle \cdot, \cdot \rangle$ denotes the dot product. The second 90-degree RF pulse would rotate back a portion of transverse magnetization along the longitudinal axis. Assuming the second RF pulse has zero phase shift ($\theta = 0$ according to Figure 1.1), the longitudinal magnetization at the end of displacement encoding module is cosine-modulated as described in equation (1.8).

$$M_z(r, t) = M_0 \cos(2\pi\langle k_e, r \rangle) \quad (1.8)$$

Between the application of displacement encoding pulses and the readout module, the longitudinal magnetization undergoes longitudinal relaxation (T_1 relaxation). The third RF pulse (with flip angle α) projects a portion of the longitudinal magnetization onto the transverse plane as described in equation (1.9).

$$M_{xy}(r, t) = \frac{1}{2} M_0 [e^{i2\pi\langle k_e, r \rangle} + e^{-i2\pi\langle k_e, r \rangle}] e^{-\frac{t}{T_1}} \sin(\alpha) + \left[1 - e^{-\frac{t}{T_1}}\right] M_0 \sin(\alpha) \quad (1.9)$$

In equation (1.8), the cosine term is replaced by its equivalent exponential terms using Euler's formula. In addition to the longitudinal relaxation of the magnetization, the tissue undergoes deformation during the time between displacement encoding and readout modules. The tissue element at the position $r - \Delta r^c$ and at the time when the displacement encoding module is applied moves to the position r at the time of readout, where Δr^c denotes the deformation of the

myocardial tissue element. The transverse magnetization after application of displacement rephrasing gradient can be described in equation (1.10).

$$\begin{aligned}
 M_{xy}(r, t) = & \frac{1}{2} M_0 \sin(\alpha) e^{-i2\pi(k_e \Delta r^c)} + \frac{1}{2} M_0 \sin(\alpha) e^{-i2\pi(k_e, -2r + \Delta r^c)} \\
 & + \left[1 - e^{-\frac{t}{T_1}} \right] M_0 \sin(\alpha) e^{-i2\pi(k_e, r + \Delta r^c)}
 \end{aligned} \tag{1.10}$$

The DENSE pulse sequence generates three echoes: (a) the desired displacement-encoded stimulated echo which is centered in k-space, (b) the complex conjugate echo which is modulated at the frequency $k = 2k_e$ in k-space, and (c) an echo due to T_1 -relaxation of the magnetization which is modulated at the frequency $k = k_e$ in k-space (T_1 -echo). While the displacement-encoded stimulated echo is a desired signal, the other two echoes generate artifacts and should be suppressed.

1.4.2 Artifact-generating echoes in DENSE

The displacement encoded stimulated echo contains the displacement information of the tissue and since it has properties that are refocused, it is considered a desired signal. The other two echoes are generally considered to cause artifacts in magnitude images, lead to inaccurate phase information, and should be suppressed. With the choice of appropriately higher displacement encoding frequency, the complex conjugate stimulated echo can be modulated to a higher frequency than those measured during the readout. The displacement encoding frequency could also be set to a high enough magnitude to shift the T_1 -echo out of acquisition window as well. However, this would lead to signal dephasing in stimulated echo and loss of measurement sensitivity in addition to more phase-wrapping in stimulated echo which can lead to a more challenging post-processing. For these reasons, the T_1 -echo is simultaneously acquired with the stimulated echo during the readout for typical values of displacement encoding frequencies.

The source of T_1 -echo is the relaxation of the longitudinal magnetization and thus, it has larger magnitude in diastolic frames than early systolic frames. The T_1 -echo can grow to a larger magnitude compared to the other echoes in diastolic cardiac frames and because of this, suppression of this echo is essential prior to post-processing of the displacement encoded stimulated echoes. Conventionally, the T_1 -echo is suppressed by using phase-cycling method and the use of through-plane dephasing gradients. In phase-cycling method, additional images are acquired by changing the phase of the second RF pulse (θ) in the DENSE pulse sequence diagram. By inducing a 180-degree phase shift to the stimulated echo in the phase-cycled data, one can suppress the T_1 -echo through subtraction of the two data. The through-plane dephasing of the T_1 -echo is performed by playing a dephasing gradient in addition to the displacement encoding gradient during the time between applications of the first and the second RF pulses. The difference between the two gradients is their direction. While displacement encoding gradient is parallel to the imaging plane, the dephasing gradient is orthogonal to the imaging plane. As the tissue undergoes the deformation throughout the cardiac cycle, the through-plane motion is encoded to the phase of the T_1 -echo and leads to its dephasing. The combination of phase-cycling^{20,21} and through-plane dephasing²² methods is effective for suppression of the T_1 -echo. However, it has some limitations. Phase cycling requires additional acquisitions which leads to longer data acquisition times. In addition, phase-cycling is susceptible to motion. Since typical DENSE acquisition times are comparable to respiration period, respiratory motion can cause the T_1 -echo being originated from different tissue and imperfect suppressions.

1.4.3 Phase-cycling method

Phase cycling acquisitions in DENSE MRI are used to suppress artifact-generating echoes. In phase cycling method, the second RF pulse in the pulse sequence of DENSE imaging is phase

shifted by θ and this phase shift is reflected as a phase shift on the acquired echoes. 2-point and 3-point phase-cycled acquisitions are used in DENSE to suppress the T_1 -echo and the complex conjugate echoes. For in-plane myocardial displacement measurements using typical acquisition parameters, only T_1 -echo is within the acquisition window. The measured signal can be described in equation 6.

$$M_{xy}^{\theta=0}(r, t) = \frac{1}{2} M_0 \sin(\alpha) e^{-i2\pi\langle k_e, \Delta r^c \rangle} + \left[1 - e^{-\frac{t}{T_1}} \right] M_0 \sin(\alpha) e^{-i2\pi\langle k_e, r + \Delta r^c \rangle} \quad (1.11)$$

To suppress the T_1 -echo, the phase of the second RF pulse is shifted by $\theta=180^\circ$ to acquire the phase-cycled data. The phase of the acquired displacement encoded stimulated echo is shifted by $\theta=180^\circ$ in the phase-cycled data as described in equation (1.12).

$$M_{xy}^{\theta=\pi}(r, t) = -\frac{1}{2} M_0 \sin(\alpha) e^{-i2\pi\langle k_e, \Delta r^c \rangle} + \left[1 - e^{-\frac{t}{T_1}} \right] M_0 \sin(\alpha) e^{-i2\pi\langle k_e, r + \Delta r^c \rangle} \quad (1.12)$$

By subtracting the phase-cycling data, the T_1 -echo is suppressed the resulting signal in equation (1.13) is comprised of only the displacement encoded stimulated echo (M_{STE}).

$$M_{STE}(r, t) = M_{xy}^{\theta=0} - M_{xy}^{\theta=\pi} = M_0 \sin(\alpha) e^{-i2\pi\langle k_e, \Delta r^c \rangle} \quad (1.13)$$

Figure 1.2.A shows the magnitude, phase, and k-space images of a phase-cycled data and resulting artifact-free stimulated-echoes computed by subtraction of the phase-cycled data.

1.4.4 Through-plane dephasing

This technique takes the advantage of the through-plane motion of the tissue to induce dephasing on the artifact-generating echoes. The encoding of the through-plane tissue motion into the phase of the acquired signals is done by playing a through-plane dephasing gradient simultaneously with the displacement encoding and displacement rephrasing gradients. The effect of the through-plane dephasing gradient on the acquired signal can be described by modifying the equation (1.11) to equation (1.14).

$$\begin{aligned}
M_{xy}^{\theta=\pi}(r_{xy}, z, t) &= \frac{1}{2} M_0 \sin(\alpha) e^{-i2\pi[(k_e, \Delta r_{xy}^c) + (k_d, \Delta r_z^c)]} \\
&+ \left[1 - e^{-\frac{t}{T_1}}\right] M_0 \sin(\alpha) e^{-i2\pi[(k_e, r_{xy} + \Delta r_{xy}^c) + (k_d, r_z + \Delta r_z^c)]}
\end{aligned} \tag{1.14}$$

k_d is the through-plane dephasing frequency, and Δr_{xy}^c and Δr_z^c are in-plane and through-plane components of myocardial displacement respectively. While encoding of the in-plane displacement is measured as the signal phase, the through-plane encoding leads to dephasing of the T₁-echo signal as the measured signal is summed along the thickness of the imaging plane.

1.4.5 Displacement measurement

After suppression of the artifact-generating echoes, the displacement can be measured by post-processing the displacement encoded stimulated echo images. The stimulated echo phase contains tissue displacement projected along the displacement encoding gradient direction as denoted by the dot product in equation (1.13). To provide multidimensional displacement measurement, the DENSE sequence is repeated to acquire multiple orthogonal displacement measurements. An additional measurement is required to correct for the background phase in the measured stimulated echoes.

1.4.6 Background phase corrections

Equation (1.13) related the stimulated echo phase to the tissue displacement in an ideal scenario where the stimulated echo phase approaches zero by using a very small (or zero in magnitude) displacement encoding gradients. In practice, field inhomogeneities and other nonlinearities²³ (such as eddy currents, Maxwell concomitant terms, and gradient distortions) leads to non-zero phase of the stimulated echo when small encoding gradients are used as described in equation (1.16).

$$M_{STE}(r, t) = M_0 \sin(\alpha) e^{-i[2\pi(k_e \Delta r^c) + \phi_b(r)]} \quad (1.15)$$

The non-zero phase is referred to as background phase and can lead to inaccurate measurements. The non-zero background phase can be measured by setting the displacement encoding gradient to zero as described in equation (1.16).

$$M_{STE}^{\phi_b}(r, t) = M_0 \sin(\alpha) e^{-i\phi_b(r)} \quad (1.16)$$

The background phase can be obtained using a separate measurement by nulling the displacement encoding gradients (simple-encoding method) or it can be subtracted by combining displacement measurements using two different encoding frequencies (balanced-encoding method).

1.4.7 Displacement encoding methods

DENSE uses two types of displacement encoding methods: (a) simple-encoding and (b) balanced-encoding²⁴. The major difference between the two methods is how the reference measurement is acquired. In simple-encoding method, the reference measurement is acquired as a separate acquisition where the displacement encoding gradients are set to zero (the through-plane dephasing gradient is still used to correct for the phase shift corresponding to the through-plane motion). In the balanced encoding method, there is no separate measurement for the background phase. Instead an additional displacement measurement in a new direction is acquired and the background phase is treated as an auxiliary variable in the measurement equation. Independent of the displacement encoding method, multiple displacement measurement can be described using an encoding matrix W . The relationship between the stimulated echo phase, the tissue displacement and the encoding matrix W can be described using equation (1.17).

$$\begin{bmatrix} \phi_1 \\ \vdots \\ \phi_N \end{bmatrix} = W \begin{bmatrix} \phi_{\Delta x} \\ \vdots \\ \phi_b \end{bmatrix} \quad (1.17)$$

The ϕ_i ($i = 1, \dots, N$) are the stimulated echo phase corresponding to the i^{th} displacement measurement, $\phi_{\Delta x}$, $\phi_{\Delta y}$, and $\phi_{\Delta z}$ are the processed (background-phase-corrected) stimulated echo phase proportional to the tissue displacements along different spatial directions, and the ϕ_b is the background phase. The displacements are calculated by solving the equation (1.17) for the displacement values. Figure 1.2 shows the 3-point balanced-encoding magnitude and phase images from a DENSE short-axis slice of left ventricle used to calculate the background phase and the background-corrected phase images proportional to the in-plane displacements.

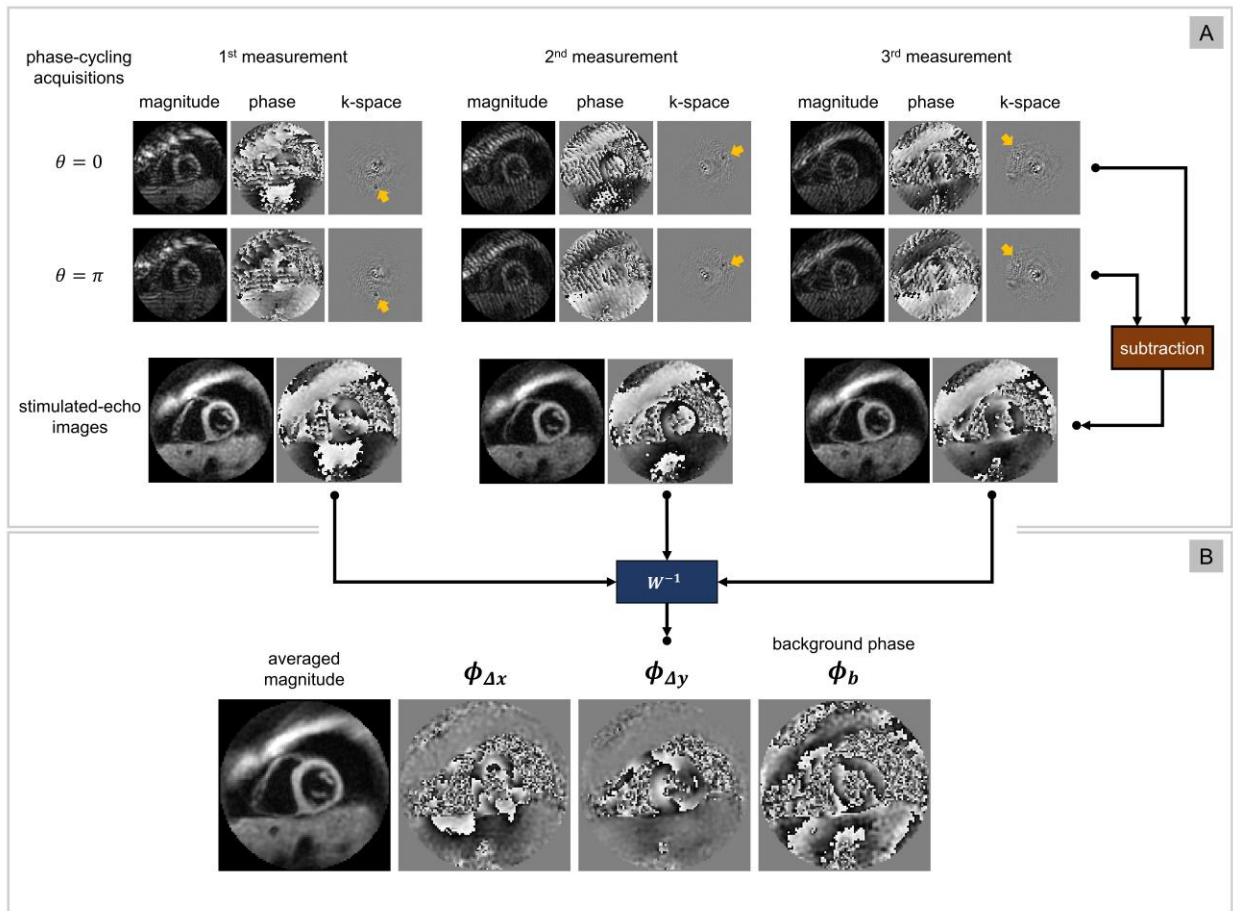


Figure 1.2 – The T_1 -echo suppression using phase-cycling method and phase decoding of the resulting stimulated echoes. A) For each displacement measurement, the phase-cycled images are acquired where the stimulated echo

phase is shifted by 180°. For each measurement, the magnitude and phase images in addition to the real (instead of complex) k-space data are shown. The subtraction of the k-space images leads to suppression of the T₁-echo (marked by yellow arrows) and artifact-free stimulated echo images. B) The raw stimulated echo phase is processed by the inverse of the displacement encoding matrix to calculate the back-ground phase corrected tissue displacements.

1.4.8 Image Analysis

Displacement fields and strain data are calculated by post-processing the phase information from the displacement encoded stimulated echoes. The post-processing consists of three major steps: (1) segmentation for a region-of-interest, (2) unwrapping the phase values within the region-of-interest, and (3) calculation of displacement fields and strain. Figure 1.3 illustrates the steps in post-processing of DENSE images from image to strain information.

There are automatic and semi-automatic approaches for post-processing of the DENSE images. In the semi-automatic approach (shown in Figure 1.3), the myocardial region-of-interest is manually contoured on a magnitude image from a single frame (usually an end-diastolic or early-systolic frame). The contour is propagated through cardiac frames using a motion-guided segmentation algorithm²⁵. The phase values within the segmented region is processed using a phase unwrapping algorithm to calculate the true phase values²⁶. The resulting phase information is used to calculate the displacement field through time using either polynomial interpolations or regularized least square fit. In the automatic approach, deep learning models are used to automatically segment the myocardial region-of-interest and to unwrap the phase values. U-Nets models were trained previously that could perform the segmentation and the phase-unwrapping task accurately which led to elimination of inter-observer variability in DENSE post-processing in addition to reduced processing time and labor¹⁸.

The displacement measurements from DENSE images are in Eulerian frame of reference meaning that at each point and time, the phase is proportional to the number of material elements

moving in or out. The displacement fields are typically more appreciated and are more intuitive when they are described in Lagrangian frame of reference. During DENSE post-processing, the Lagrangian fields (Figure 1.3.K) are calculated by tracking each spatial element through time.

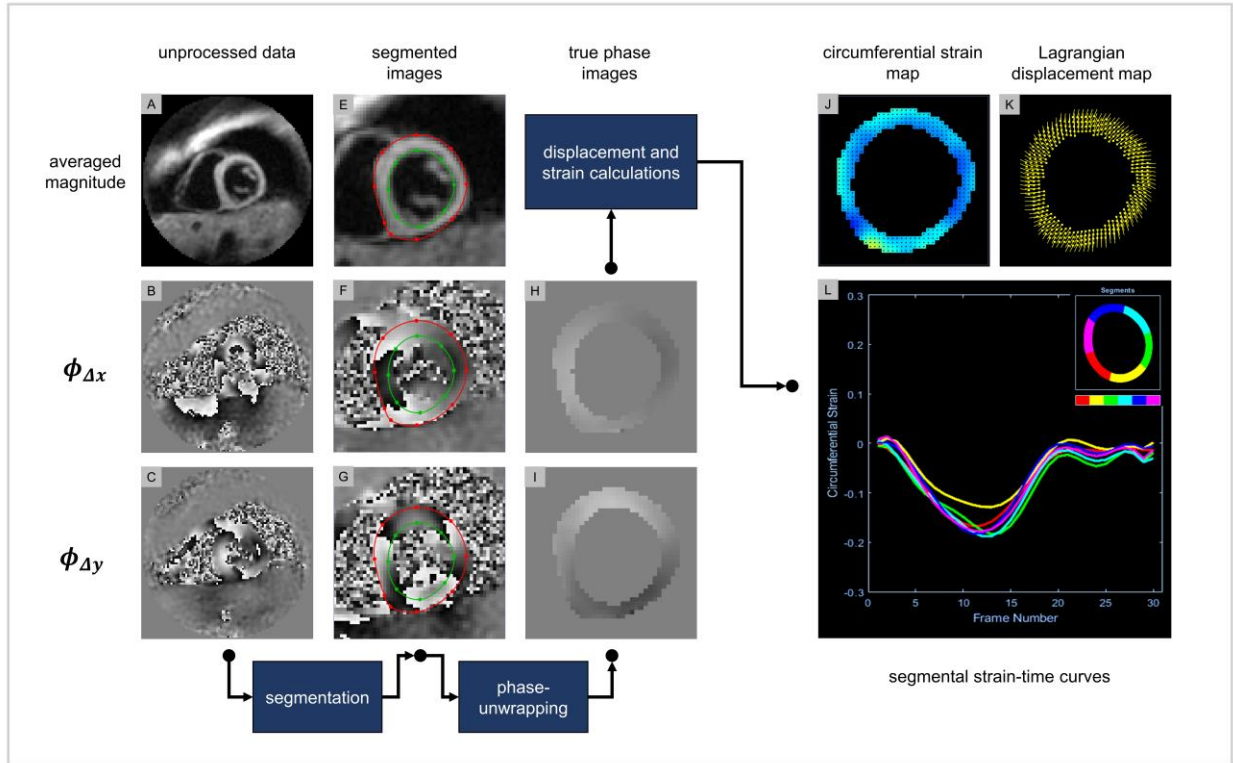


Figure 1.3 – Analysis of DENSE images include segmentation for a region-of-interest, un-wrapping of the phase information within the region-of-interest to compute the true phase values, and interpolation of the displacement field using the true phase values. The displacement fields are then used to calculate strain data. Circumferential strain (E_{cc}) shown in panels J and L is the most common strain parameter used for assessment of cardiac function with DENSE.

1.5 Breath-hold DENSE acquisitions

As it was illustrated in Figure 1.1, the DENSE acquisition is electrocardiogram-gated and use spiral trajectories to sample the k-space. With typical length of spiral readouts, multiple spiral acquisitions are required to sufficiently sample the k-space corresponding to a single cardiac frame. A shorter spiral readout does not sufficiently traverse the k-space, while the longer spiral readout might be adversely affected by artifact due to myocardial motion or T_2 -relaxation of the

transverse magnetization or the artifacts due to myocardial tissue deformation during the readout. Using typical imaging parameters, acquisitions have to iterate through multiple heartbeats to sufficiently sample the k-space. This makes the DENSE acquisitions times in cardiac applications comparable to the respiratory motion period. As shown in Figure 1.4, respiratory motion creates artifacts in the MRI acquisitions and should be avoided for reliable measurements. For this reason, the DENSE acquisitions are performed during breath-holding. Multiple short-axis DENSE slices are required to sufficiently cover the left-ventricle where each slice requires a separate breath-hold scans.

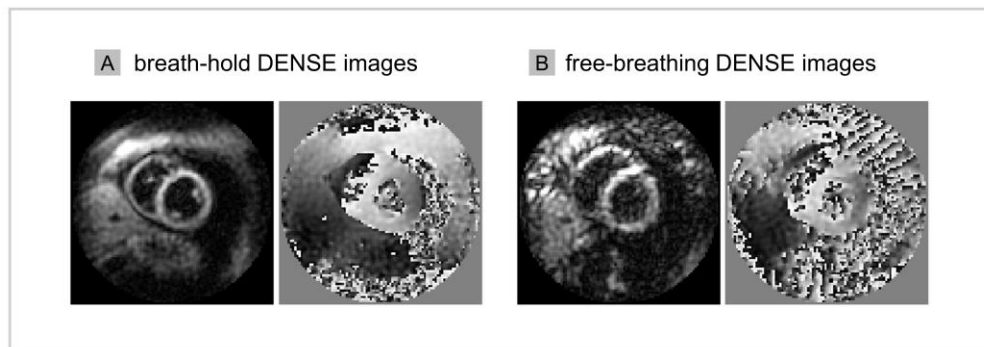


Figure 1.4 – Example DENSE magnitude and phase images from breath-hold (A) and free-breathing (B) acquisitions

Breath-holding could be challenging for multiple reasons. (1) Cardiac MRI examinations can last for 60-90 minutes with multiple breath-holding which can be challenging and discomforting for patients. Usually patients get tired or fall asleep during data acquisitions and fail to perform a perfect breath-holds which can lead to sub-optimal image quality. It is very common during cardiac MRI to repeat the acquisition multiple slices to ensure high quality of the incoming data. This leads to prolonged cardiac MRI scans and more discomfort for patients. (2) In many clinical scenarios, breath-hold acquisitions are challenging or even impossible. For example, drowsiness as side effect of many pain medications can affect the patients' consciousness and

ability to hear the breath-hold instructions. In more extreme examples such as patients that are under sedation or pediatric patients, breath-hold scans are even impossible to perform. These challenges create a broad need for free-breathing DENSE acquisitions.

1.6 Free-breathing DENSE

There have been two major methods developed previously for DENSE MRI that enables free-breathing acquisitions: (1) diaphragm navigator-gated DENSE¹⁹, and (2) self-navigated DENSE²⁷.

1.6.1 Diaphragm navigator-gated DENSE

In diaphragm navigator-gated DENSE, data is continuously acquired during free-breathing. A navigator echo is acquired at the beginning or at the end of each heartbeat to track the superior-inferior position of the diaphragm. Since the respiratory motion during end-expiration is minimal, data that fall within a small acceptance window corresponding to the end-expiration is used for images reconstruction.

The diaphragm navigator-gated acquisitions start by acquiring additional sagittal and coronal scout images (Figure 1.5.A-B) to locate the diaphragm. Additional RF pulses are used to place two intersecting bands at the right dome of the diaphragm (marked by yellow arrows in Figure 1.5.A-B). Navigator echoes are acquired and reconstructed in the readout direction and are displayed as a line of data. After placing the navigator bands, a scout scan is performed to identify the end-expiration position of the diaphragm and select the acceptance window (Figure 1.5.C). Once the navigator set-up is complete, the gated scan is performed with a live tracking of diaphragm position (Figure 1.5.D).

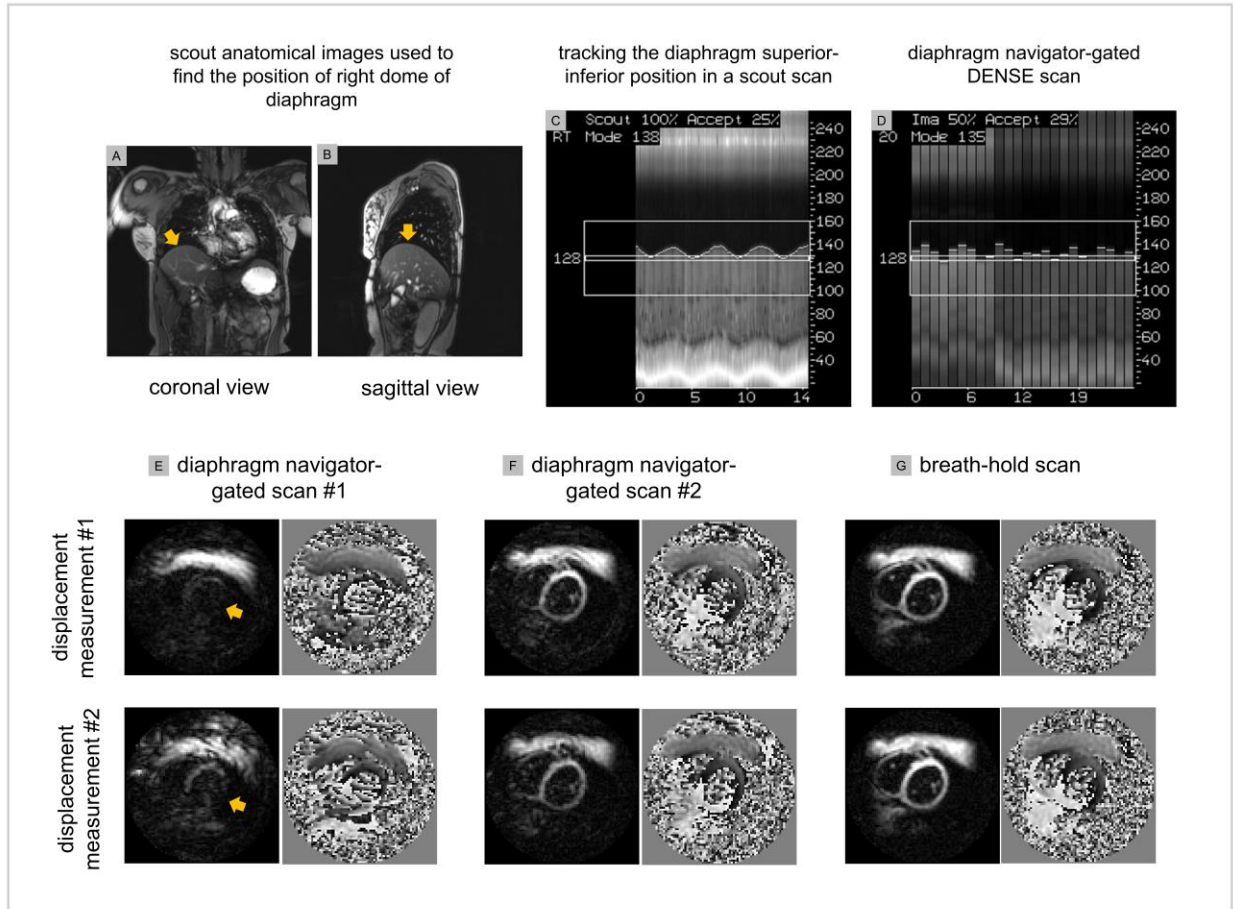


Figure 1.5 – Diaphragm navigator-gated DENSE enables free-breathing acquisitions. Additional coronal (A) and sagittal (B) scout images are acquired to find the position of diaphragm. The navigator bands are placed on the right dome of diaphragm (marked by yellow arrows in A and B). A scout scan is performed to track the position of right dome. A small window at end-expiration position of the diaphragm is used to accept or reject the acquired free-breathing data. Data that fall within the accept widow is used for image reconstruction. One limitation of this method is the variable image quality. Example images are shown in panels E and F illustrating this limitation.

The diaphragm navigator-gated DENSE has some limitations: (1) The quality of the acquired data is variable from scan to scan. Figure 1.5.E-F show DENSE images corresponding to two separate diaphragm navigator-gates scans from the same short-axis slice location. While DENSE images in panel F display comparable quality to the breath-hold scan of the same slice, images in panel E show significant level of artifacts. (2) The navigator set-up is complex and time-consuming. Additional scout scan prolongs the scan time. Typically, multiple scout images are

required to precisely locate the dome of diaphragm. In addition, patients' motion during the scan may require the operator to re-adjust the location of the navigator bands. (3) The imaging efficiency is as low as 20-30%. In the image reconstruction, only data that falls within the acceptance window are used in image reconstruction and the remaining data are discarded. This leads to low acquisition efficiency in diaphragm navigator-gated DENSE. Variations in respiratory pattern due to subjects' motion, deep breath, or subject falling asleep can drastically reduce the acquisitions efficiency or may require re-adjusting the navigator in some cases. These challenges motivated us to pursue alternative free-breathing methods in DENSE.

1.6.2 Free-breathing DENSE using match-making and self-navigation

The self-navigation is an alternative approach that that enables free-breathing acquisitions without diaphragm navigators. In self-navigation, respiratory motion is estimated from acquired data and the respiratory motion errors are corrected using the estimated motion²⁸.

Figure 1.6 shows a general approach used in self-navigated MRI. As shown in panels A and B, acquired free-breathing data from different heartbeats are assigned to different motion states. Low-resolution images are reconstructed by combining the consecutive segments in each motion state (panel C). Typically, segmented acquisitions with golden-angle or uniform rotations through time is used so that consecutive segments form fully-sampled images. Image-based navigators are used in a rigid registration algorithm to estimate the motion between states and also between the navigators within each state (panel D). The estimated motion is used to correct for the respiratory motion errors.

Respiratory motion can also affect the T_1 -echo. In free-breathing acquisitions, the respiratory motion causes tissue motion and the T_1 -echo being originated from different tissue. This can affect the images in the phase-cycled acquisitions. Motion between phase-cycling data

leads to imperfect suppression and residual T_1 -echo after phase-cycling subtractions. Prior to motion compensation using self-navigation, the T_1 -echo needs to be suppressed in free-breathing data. Previously, match-making method was developed that can effectively suppress the T_1 -echo by identifying the phase-cycling pairs at the matched respiratory positions. Residual T_1 -echo energy was shown to have strong correlation with the matched position of the phase-cycled data and is used in the match-making algorithm to identify the phase-cycling pairs. Once T_1 -echo is suppressed, the self-navigation method can be used to correct for the motion artifacts on the stimulated echoes.

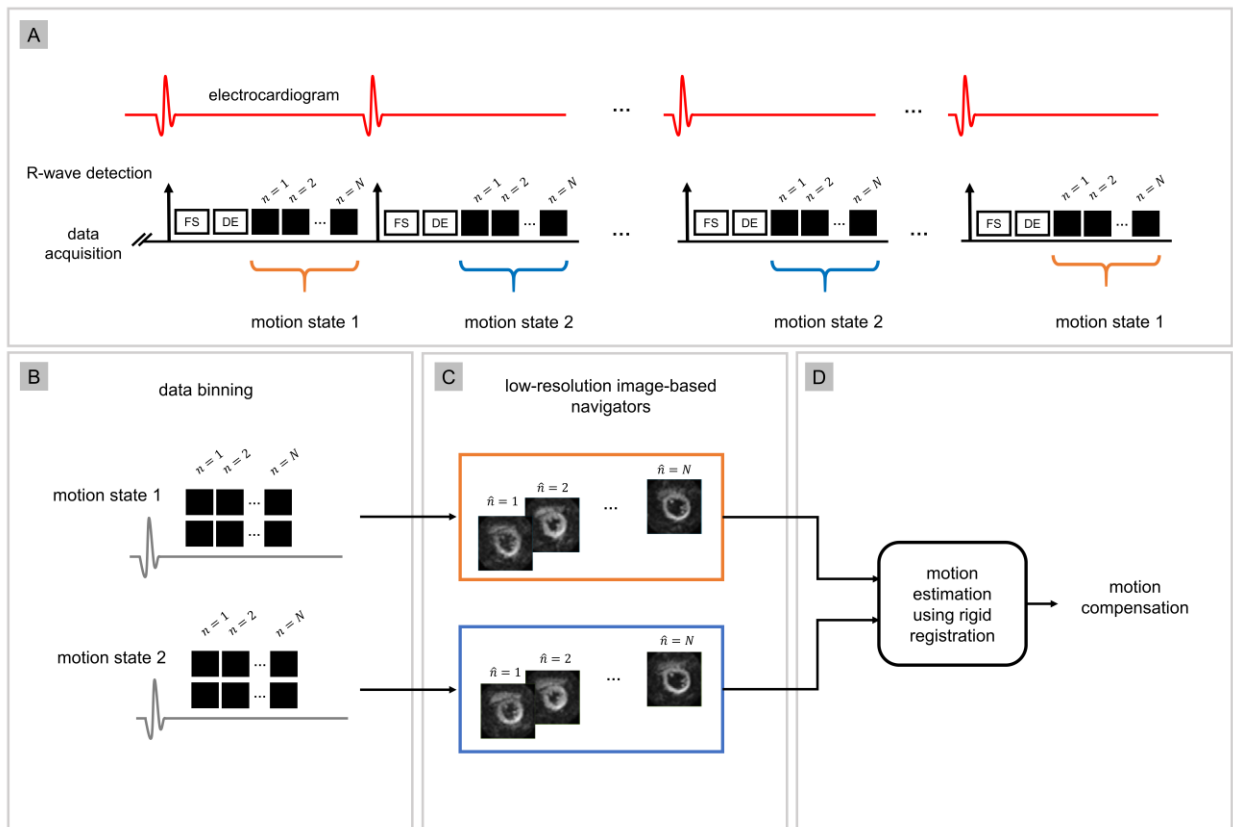


Figure 1.6 – Diagram showing the general approach for motion estimation using self-navigation. Data from different heartbeats are assigned to different motion states. Multiple low-resolution image navigators are reconstructed from data within each motion state. The image navigators are used in rigid registration algorithm to estimate the motion between different states and between different navigators within each state. The estimated motion is used for motion compensation.

Motion compensation using self-navigation accounts for the tissue position shifts in image domain. The position shift (approximately rigid) in image domain corresponds to linear phase errors in k-space. In segmented DENSE acquisitions, each segment is affected by a unique respiratory-motion-induced position shift. The resulting artifact is blurring/ghosting in image domain. This type of artifact is the most common among spin-echo-based and gradient-echo-based MRI methods. Self-navigation is an effective method to correct the blurring/ghosting artifact. However, it does not account for all types of respiratory motion artifacts that arise in stimulated echo imaging. Figure 1.7 illustrates two examples from self-navigated free-breathing DENSE. While the blurring/ghosting artifact is corrected in the first acquisition, self-navigation failed to correct all the artifacts due to respiratory motion in the second acquisition. This example demonstrates that a more accurate motion compensation method is required for reliable free-breathing DENSE.

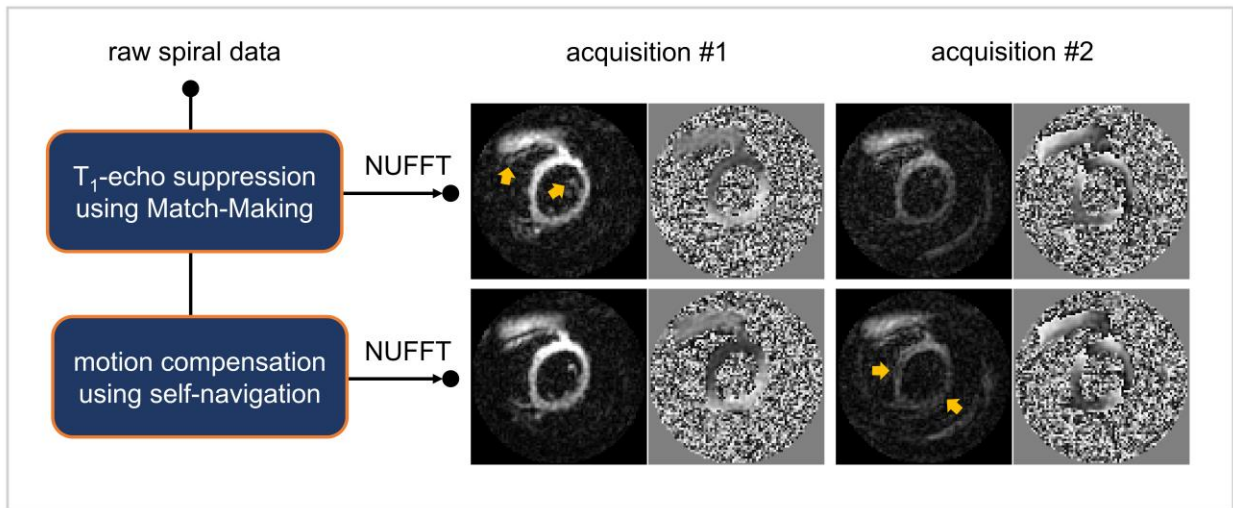


Figure 1.7 – Two examples showing motion compensation using self-navigation in DENSE. The estimated motion from self-navigation is used to correct the linear phase errors in the first and the second acquisitions after suppression of the T_1 -echo. While blurring/ghosting artifacts are corrected in the first acquisitions, the motion compensation failed to correct the all types of artifacts including the signal loss in the second acquisition. This example demonstrates that motion compensations should be extended to account for all types of respiratory motion artifacts in stimulated echo imaging.

1.7 Respiratory motion artifacts in DENSE MRI

Three types of artifacts arise in free-breathing DENSE MRI due to respiration: (1) First respiratory motion shifts the tissue during free-breathing acquisition and because of this shift, different tissue might contribute to the formation of the T_1 -echo in the phase-cycling acquisitions. This leads to imperfect suppression of the T_1 -echo after phase-cycling subtraction. The residual T_1 -echo energy in k-space manifests in the form of stripe artifacts in the image domain. (2) Respiratory motion causes position shifts of the tissue during the free-breathing acquisitions. The approximately rigid position shift leads to linear phase errors in k-space. The linear phase errors lead to blurring/ghosting artifacts in segmented DENSE where each segment is affected by a unique position shift and the corresponding linear phase error. (3) The tissue displacement encoded to the phase of the stimulated echo leads to phase shifts in the image domain. While the phase shifts due to tissue deformation are measured in the post-processing, the respiratory-induced phase shifts generate artifacts in the simulated echo images. The respiratory-induced phase shift corresponds to a constant phase error in k-space and in the segmented DENSE, leading to signal loss and phase corruption in magnitude- and phase-reconstructed stimulated echo images. Figure 1.8 shows the three types of artifacts in DENSE images on a phantom.

Conventional motion compensation methods are developed for spin-echo and gradient-echo imaging account for position shifts and the corresponding linear phase errors. For stimulated-echo imaging, these methods need to be extended to account for respiratory-induced phase shifts and the corresponding constant phase errors.

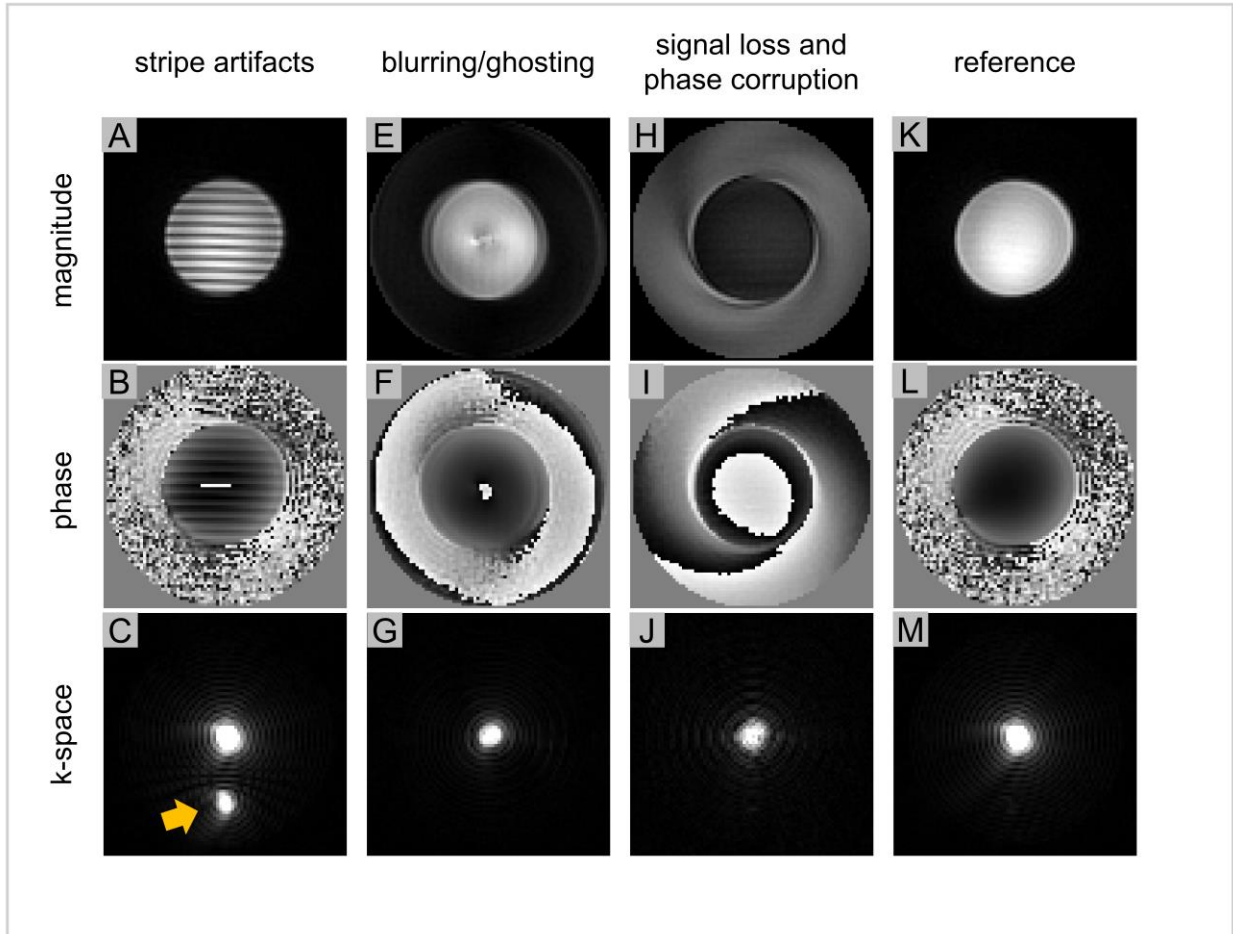


Figure 1.8 - Example magnitude images, phase image, and k-space showing three types of respiratory-motion-induced artifacts in DENSE on a phantom. 1) Stripe artifacts (A-C) are caused by imperfect suppression of the T_1 -echo due to motion. 2) Position shift of tissue leads to approximately linear phase errors in k-space. In segmented DENSE, linear phase errors manifest in the form of blurring/ghosting artifacts (E). 3) The encoding of the tissue motion to the phase of the stimulated echo leads to phase shifts in image domain and constant phase errors in k-space. In segmented DENSE, this manifests in the form of signal loss (H) and phase corruptions (I) in image domain.

1.8 Deep learning

Deep learning is set of machine learning techniques and algorithms that enable computers to automatically extract complex features and patterns in large data sets that are otherwise challenging or impossible to perform manually. Deep learning has gained tremendous attention

and investment for development over the past decade after outperforming other methods in several image analysis benchmarks.

Deep learning methods are neural networks with multiple layers (arrays) of computational units (called neuron) where each unit is connected to all the units in previous layer (fully connected neural network). The input layer of the neural network processes the input data and transform it to a higher-level representation. The output layer transforms the data into the desired output format. The input and output layers are sandwiched by one or more (hence the name, deep) hidden layers that process the high-level representations (features) as the data flows through. The network is trained to produce desired output per input data by determining parameters of each neuron through a process called training. A set or input and desired output is used for training the neural networks. Generally, the training has two major phases: (1) In feedforward, the input data flows through the layers of the network and the corresponding output is generated. The output is compared to the desired output using an objective function. (2) In the learning phase, the values of the objective function are used in a backpropagation algorithm to update the parameters of each neuron to generate a more accurate output. This process usually is performed using multiple batches of the training data depending on the size of the training set, number of learnable parameters, and the limitations enforced by the hardware computational power. The training usually iterates in multiple passes (epochs) until convergence is observed in the values of objective function.

Conventional machine learning models used to employ hand-crafted features extracted from the raw data either by manually design or learning from other simple machine learning models²⁹. By contrast, deep learning models merged the feature extraction and the performing the task into one problem³⁰. The power of deep learning models is the automatic feature learning.

The most common type of deep learning models are convolutional neural networks for image analysis applications³¹. Convolutional neural networks are regularized version of fully connected networks by limiting the activation of each neuron to a small receptive field from the previous layer. This aims to preserve spatial information in the input images and avoid overfitting problems in the fully connected neural networks.

Deep learning has gained much attention in the field of MRI for its potential to learn high level feature automatically. There have been several studies that demonstrated applications of deep learning for elevating user experience by automating the image post-processing^{18,32-35} or generating imaging protocols^{36,37}, for improving and accelerating the image reconstruction^{38,39}, overcoming challenges in data acquisitions^{40,41}, or artifact suppression and noise reductions from various sources⁴²⁻⁴⁴. Specifically, deep learning has been used for correction of artifacts caused by voluntarily motion of subject in brain imaging, respiratory motion for cardiac and abdominal imaging, and motion in pediatric imaging applications⁴⁵⁻⁵⁰.

1.9 Statement of research objectives

My dissertation research is primarily focused on application of deep learning methods for artifact suppressions in cine DENSE MRI.

In Chapter 2, a deep learning method is introduced for suppression of the artifact-generating T_1 -echo to overcome the long acquisitions times of the phase-cycling method. The proposed deep learning method uses the stripe-artifact-free phase-cycled and a non-phase-cycling images as reference and input respectively to train a convolutional neural network. The trained model is able to suppress the T_1 -echo in non-phase-cycling input images without the need for

phase-cycling acquisitions. The feasibility of the trained model was evaluated on non-phase-cycling cine DENSE images from healthy human subjects.

In Chapter 3, a deep learning model is developed for compensation of respiratory-motion-induced signal loss and phase corruption in self-navigated cine DENSE. A new mathematical model is introduced that accounts for the respiratory-motion-induced phase shifts due to the encoding of the respiration motion into the phase of the simulated echo. Phantom experiments and simulation were performed to validate the proposed mathematical model and demonstrate the effect of phase shift in segmented DENSE acquisitions. The mathematical model was used to simulate artifacts due to respiratory-motion-induced phase shifts on breath-hold data to train a convolutional neural network. The trained convolutional neural network was evaluated on self-navigated free-breathing cine DENSE images from healthy human subjects.

In Chapter 4, the developed motion compensation model (from Chapter 3) was evaluated on self-navigated cine DENSE images acquired using adaptive free-breathing from healthy subjects and heart-failure patients. Systolic and diastolic strain parameters in addition to image quality measures were used to evaluate the processed images using the developed deep learning model. The deep learning motion compensation in conjunction with adaptive acquisition was compared to the diaphragm-navigator gated method.

In Chapter 5, an overview of my doctoral research is presented, the developed methods are discussed in addition to their limitations and future research directions.

1.10 References

1. Lauterbur PC. Image formation by induced local interactions: examples employing nuclear magnetic resonance. *Nature*. 1973;242(5394):190-191.

2. Kellman P, Arai AE, McVeigh ER, Aletras AH. Phase-sensitive inversion recovery for detecting myocardial infarction using gadolinium-delayed hyperenhancement. *Magn Reson Med An Off J Int Soc Magn Reson Med*. 2002;47(2):372-383.
3. Mewton N, Liu CY, Croisille P, Bluemke D, Lima JAC. Assessment of myocardial fibrosis with cardiovascular magnetic resonance. *J Am Coll Cardiol*. 2011;57(8):891-903.
4. Aletras AH, Kellman P, Derbyshire JA, Arai AE. ACUT2E TSE-SSFP: a hybrid method for T2-weighted imaging of edema in the heart. *Magn Reson Med An Off J Int Soc Magn Reson Med*. 2008;59(2):229-235.
5. Messroghli DR, Moon JC, Ferreira VM, et al. Clinical recommendations for cardiovascular magnetic resonance mapping of T1, T2, T2* and extracellular volume: a consensus statement by the Society for Cardiovascular Magnetic Resonance (SCMR) endorsed by the European Association for Cardiovascular Imaging (EACVI). *J Cardiovasc Magn Reson*. 2017;19(1):1-24.
6. Luyt C-E, Galanaud D, Perlberg V, et al. Diffusion tensor imaging to predict long-term outcome after cardiac arrest: a bicentric pilot study. *J Am Soc Anesthesiol*. 2012;117(6):1311-1321.
7. Seraphim A, Knott KD, Augusto J, Bhuva AN, Manisty C, Moon JC. Quantitative cardiac MRI. *J Magn Reson Imaging*. 2020;51(3):693-711.
8. Ponikowski P, Voors AA, Anker SD, et al. 2016 ESC Guidelines for the diagnosis and treatment of acute and chronic heart failure. *Kardiol Pol (Polish Hear Journal)*. 2016;74(10):1037-1147.
9. Nagueh SF, Smiseth OA, Appleton CP, et al. Recommendations for the evaluation of left ventricular diastolic function by echocardiography: an update from the American Society

- of Echocardiography and the European Association of Cardiovascular Imaging. *Eur J Echocardiogr.* 2016;17(12):1321-1360.
10. Westenberg JJM. CMR for assessment of diastolic function. *Curr Cardiovasc Imaging Rep.* 2011;4(2):149-158.
 11. Ersbøll M, Andersen MJ, Valeur N, et al. Early diastolic strain rate in relation to systolic and diastolic function and prognosis in acute myocardial infarction: a two-dimensional speckle-tracking study. *Eur Heart J.* 2014;35(10):648-656. doi:10.1093/eurheartj/eh179
 12. Mishra S, Kass DA. Cellular and molecular pathobiology of heart failure with preserved ejection fraction. *Nat Rev Cardiol.* 2021;18(6):400-423.
 13. Chitiboi T, Axel L. Magnetic resonance imaging of myocardial strain: a review of current approaches. *J Magn Reson Imaging.* 2017;46(5):1263-1280.
 14. Aletras AH, Ding S, Balaban RS, Wen H. DENSE: displacement encoding with stimulated echoes in cardiac functional MRI. *J Magn Reson (San Diego, Calif 1997).* 1999;137(1):247.
 15. Kim D, Gilson WD, Kramer CM, Epstein FH. Myocardial tissue tracking with two-dimensional cine displacement-encoded MR imaging: development and initial evaluation. *Radiology.* 2004;230(3):862-871.
 16. Lin K, Meng L, Collins JD, Chowdhary V, Markl M, Carr JC. Reproducibility of cine displacement encoding with stimulated echoes (DENSE) in human subjects. *Magn Reson Imaging.* 2017;35:148-153.
 17. Auger DA, Ghadimi S, Cai X, et al. Reproducibility of global and segmental myocardial strain using cine DENSE at 3 Tesla: A multicenter study in healthy subjects and heart disease patients. *J Card Magn Reson.* 2022.

18. Ghadimi S, Auger DA, Feng X, Sun C, Meyer CH, Bilchick KC, Cao JJ, Scott, AD, Oshinski JN, Ennis DB EF. Fully-automated global and segmental strain analysis of DENSE cardiovascular magnetic resonance using deep learning for segmentation and phase unwrapping. *J Cardiovasc Magn Reson*. 2021.
19. Zhong X, Spottiswoode BS, Meyer CH, Kramer CM, Epstein FH. Imaging three-dimensional myocardial mechanics using navigator-gated volumetric spiral cine DENSE MRI. *Magn Reson Med*. 2010;64(4):1089-1097.
20. Tsao J, Laurent D. N-SPAMM for efficient displacement-encoded acquisition in myocardial tagging. *Proc 13th Annu Meet ISMRM, Miami Beach, Florida, USA*. 2005;42(6):273.
21. Epstein FH, Gilson WD. Displacement-encoded MRI of the heart using Cosine AND Sine modulation to ELiminate (CANSEL) artifact-generating echoes.
22. Zhong X, Spottiswoode BS, Cowart EA, Gilson WD, Epstein FH. Selective suppression of artifact-generating echoes in cine DENSE using through-plane dephasing. *Magn Reson Med An Off J Int Soc Magn Reson Med*. 2006;56(5):1126-1131.
23. Markl M, Frydrychowicz A, Kozerke S, Hope M, Wieben O. 4D flow MRI. *J Magn Reson Imaging*. 2012;36(5):1015-1036.
24. Zhong X, Helm PA, Epstein FH. Balanced Multipoint Displacement Encoding for DENSE. 2009;988:981-988. doi:10.1002/mrm.21851
25. Spottiswoode BS, Zhong X, Lorenz CH, Mayosi BM, Meintjes EM, Epstein FH. Motion-guided segmentation for cine DENSE MRI. *Med Image Anal*. 2009;13(1):105-115.
26. Spottiswoode BS, Zhong X, Hess AT, et al. Tracking myocardial motion from cine DENSE images using spatiotemporal phase unwrapping and temporal fitting. *IEEE Trans*

- Med Imaging*. 2006;26(1):15-30.
27. Cai X, Epstein FH. Free-breathing cine DENSE MRI using phase cycling with matchmaking and stimulated-echo image-based navigators. *Magn Reson Med*. 2018;80(5):1907-1921.
 28. Pang J, Bhat H, Sharif B, et al. Whole-heart coronary MRA with 100% respiratory gating efficiency: self-navigated three-dimensional retrospective image-based motion correction (TRIM). *Magn Reson Med*. 2014;71(1):67-74.
 29. Lundervold AS, Lundervold A. An overview of deep learning in medical imaging focusing on MRI. *Z Med Phys*. 2019;29(2):102-127.
 30. Aggarwal CC. Neural networks and deep learning. *Springer*. 2018;10:973-978.
 31. Litjens G, Kooi T, Bejnordi BE, et al. A survey on deep learning in medical image analysis. *Med Image Anal*. 2017;42:60-88.
 32. De Vos BD, Berendsen FF, Viergever MA, Sokooti H, Staring M, Išgum I. A deep learning framework for unsupervised affine and deformable image registration. *Med Image Anal*. 2019;52:128-143.
 33. Wang K, Li Y, Kemao Q, Di J, Zhao J. One-step robust deep learning phase unwrapping. *Opt Express*. 2019;27(10):15100-15115.
 34. Chen H, Dou Q, Yu L, Qin J, Heng P-A. VoxResNet: Deep voxelwise residual networks for brain segmentation from 3D MR images. *Neuroimage*. 2018;170:446-455.
 35. Akkus Z, Galimzianova A, Hoogi A, Rubin DL, Erickson BJ. Deep learning for brain MRI segmentation: state of the art and future directions. *J Digit Imaging*. 2017;30(4):449-459.
 36. Lee YH. Efficiency improvement in a busy radiology practice: determination of

- musculoskeletal magnetic resonance imaging protocol using deep-learning convolutional neural networks. *J Digit Imaging*. 2018;31(5):604-610.
37. Abdi M, Zhao Y, Farhand S, et al. MRI protocol recommendation using deep metric learning. In: *Joint Annual Meeting ISMRM-ESMRMB & ISMRT 31st Annual Meeting*. London, UK; 2022.
 38. Küstner T, Fuin N, Hammernik K, Bustin A, reports HQ-S, 2020 undefined. CINENet: deep learning-based 3D cardiac CINE MRI reconstruction with multi-coil complex-valued 4D spatio-temporal convolutions. *nature.com*. <https://www.nature.com/articles/s41598-020-70551-8>. Accessed March 31, 2022.
 39. Qin C, Schlemper J, Caballero J, Price AN, Hajnal J V., Rueckert D. Convolutional recurrent neural networks for dynamic MR image reconstruction. *arXiv*. 2017;38(1):280-290.
 40. Gong E, Pauly JM, Wintermark M, Zaharchuk G. Deep learning enables reduced gadolinium dose for contrast-enhanced brain MRI. *J Magn Reson imaging*. 2018;48(2):330-340.
 41. Knoll F, Hammernik K, Kobler E, Pock T, Recht MP, Sodickson DK. Assessment of the generalization of learned image reconstruction and the potential for transfer learning. *Magn Reson Med*. 2019;81(1):116-128.
 42. Zhang Q, Ruan G, Yang W, et al. MRI Gibbs-ringing artifact reduction by means of machine learning using convolutional neural networks. *Magn Reson Med*. 2019;82(6):2133-2145. doi:10.1002/mrm.27894
 43. Hales PW, Pfeuffer J, A. Clark C. Combined Denoising and Suppression of Transient Artifacts in Arterial Spin Labeling MRI Using Deep Learning. *J Magn Reson Imaging*.

- 2020;52(5):1413-1426. doi:10.1002/jmri.27255
44. Jiang D, Dou W, Vosters L, Xu X, Sun Y, Tan T. Denoising of 3D magnetic resonance images with multi-channel residual learning of convolutional neural network. *Jpn J Radiol.* 2018;36(9):566-574. doi:10.1007/s11604-018-0758-8
 45. Duffy BA, Zhang W, Tang H, et al. Retrospective correction of motion artifact affected structural MRI images using deep learning of simulated motion. *Med Imaging with Deep Learn.* 2018;(Midl 2018):1-8.
 46. Qi H, Hajhosseiny R, Cruz G, ... TK-M, 2021 undefined. End-to-end deep learning nonrigid motion-corrected reconstruction for highly accelerated free-breathing coronary MRA. *Wiley Online Libr.* <https://onlinelibrary.wiley.com/doi/abs/10.1002/mrm.28851>. Accessed March 31, 2022.
 47. Tamada D, Kromrey ML, Ichikawa S, Onishi H, Motosugi U. Motion artifact reduction using a convolutional neural network for dynamic contrast enhanced mr imaging of the liver. *Magn Reson Med Sci.* 2020;19(1):64-76. doi:10.2463/mrms.mp.2018-0156
 48. Küstner T, Armanious K, Yang J, Yang B, Schick F, Gatidis S. Retrospective correction of motion-affected MR images using deep learning frameworks. *Magn Reson Med.* 2019;82(4):1527-1540.
 49. Armanious K, Gatidis S, Nikolaou K, Yang B, Thomas K. RETROSPECTIVE CORRECTION OF RIGID AND NON-RIGID MR MOTION ARTIFACTS USING GANS University of Stuttgart , Institute of Signal Processing and System Theory , Stuttgart , Germany University of Tübingen , Department of Radiology , Tübingen ' s College Lond. *IEEE 17th Int Symp Biomed Imaging.* 2020;(Isbi):1550-1554.
 50. Jiang W, Liu Z, Lee K-H, et al. Respiratory Motion Correction in Abdominal MRI using a

Densely Connected U-Net with GAN-guided Training. *arXiv e-prints*. June 2019:arXiv:1906.09745.

Chapter 2 : Suppression of Artifact-Generating Echoes in Cine DENSE Using Deep Learning

2.1 Abstract

Purpose: To employ deep learning for suppression of the artifact-generating T_1 -echo in cine displacement encoding with stimulated echoes (DENSE) for the purpose of reducing the scan time.

Methods: A U-Net was trained to suppress the artifact-generating T_1 -echo using complementary phase-cycled data as the ground truth. A data augmentation method was developed that generates synthetic DENSE images with arbitrary displacement encoding frequencies to suppress the T_1 -echo modulated for a range of frequencies. The resulting U-Net (DAS-Net) was compared to a k-space zero-filling as an alternative method. Non-phase-cycled DENSE images acquired in shorter breath-holds were processed by DAS-Net and compared to DENSE images acquired with phase-cycling for the quantification of myocardial strain.

Results: DAS-Net effectively suppressed the T_1 -echo and its artifacts, and achieved root mean square error (RMSE) = 5.5 ± 0.8 and structural similarity index (SSIM) = 0.85 ± 0.02 for DENSE images acquired with a displacement encoding frequency of 0.10 cycles/mm. DAS-Net outperformed zero-filling (RMSE = 5.8 ± 1.5 vs 13.5 ± 1.5 , DAS-Net vs zero-filling, $p < 0.01$ and SSIM = 0.83 ± 0.04 vs 0.66 ± 0.03 , DAS-Net vs zero-filling, $p < 0.01$). Strain data for non-phase-cycled DENSE images with DAS-Net showed close agreement with strain from phase-cycled DENSE.

Conclusion: DAS-Net provides an effective alternative approach for suppression of the artifact-generating T_1 -echo in DENSE MRI, enabling a 42% reduction in scan time compared to DENSE with phase cycling.

2.2 Introduction

Cine displacement encoding with stimulated echoes (DENSE) is a strain MRI method with applications to the heart¹⁻⁴, brain⁵, blood vessel wall⁶, skeletal muscle⁷, and other areas. In DENSE, tissue displacement is encoded in the phase of the stimulated echo; however, when generating a stimulated echo, other echoes such as the conjugate stimulated echo and an echo due to T_1 relaxation are also generated (T_1 -echo)⁸. As only the stimulated echo has the properties that it is refocused and its phase is directly encoded for tissue displacement, the other echoes are generally considered to cause artifacts. Methods have been developed to isolate the stimulated echo and suppress the other echoes. These methods include using a relatively high displacement-encoding frequency¹, acquiring complementary phase-cycled acquisitions⁹⁻¹¹, applying inversion recovery¹², using through-plane dephasing⁸, and combinations of the aforementioned methods. However, these methods have limitations such as partial loss of the stimulated echo signal due to intravoxel dephasing⁸, imperfect suppression of the artifact-generating echoes due to motion between complementary acquisitions¹³, decreasing the signal amplitude and altering the contrast, and increasing the scan time. An ideal method would suppress the artifact-generating echoes without these limitations.

While artifact suppression in DENSE has previously been addressed using solutions based on MR physics, isolation of the stimulated echo and suppression of the other echoes may also be seen as a single-channel signal separation problem and may be addressed using signal processing or deep learning. Since single-channel signal separation problems are inherently ill-posed, linear

techniques such as independent component analysis require strong priors¹⁴. Recent studies have applied deep convolutional neural networks (CNNs) to address this class of problems in audio and visual domains¹⁵⁻¹⁷ without the need for assumptions about the signals. Also, CNNs have been used for suppression of MRI artifacts from various sources including partial volume effects¹⁸, fat¹⁹, motion²⁰⁻²⁸, and others. In most cases, training is formulated as supervised learning^{18,20,22-24,26-29}, and the U-Net with modifications has been a popular choice for network architecture^{2,5,6,10}. As typical DENSE protocols for cardiac imaging use a displacement-encoding frequency that shifts the conjugate stimulated echo outside the acquisition window, we investigated the use of a U-Net³¹ to suppress the T₁-echo.

2.3 Methods

We trained a U-Net using artifact-free DENSE images obtained from phase-cycled acquisitions to isolate the stimulated echo and suppress the T₁-echo (Figure 2.1). Also, a data augmentation technique was developed to generate synthetic DENSE training data with arbitrary displacement-encoding frequencies to achieve a more generalized model.

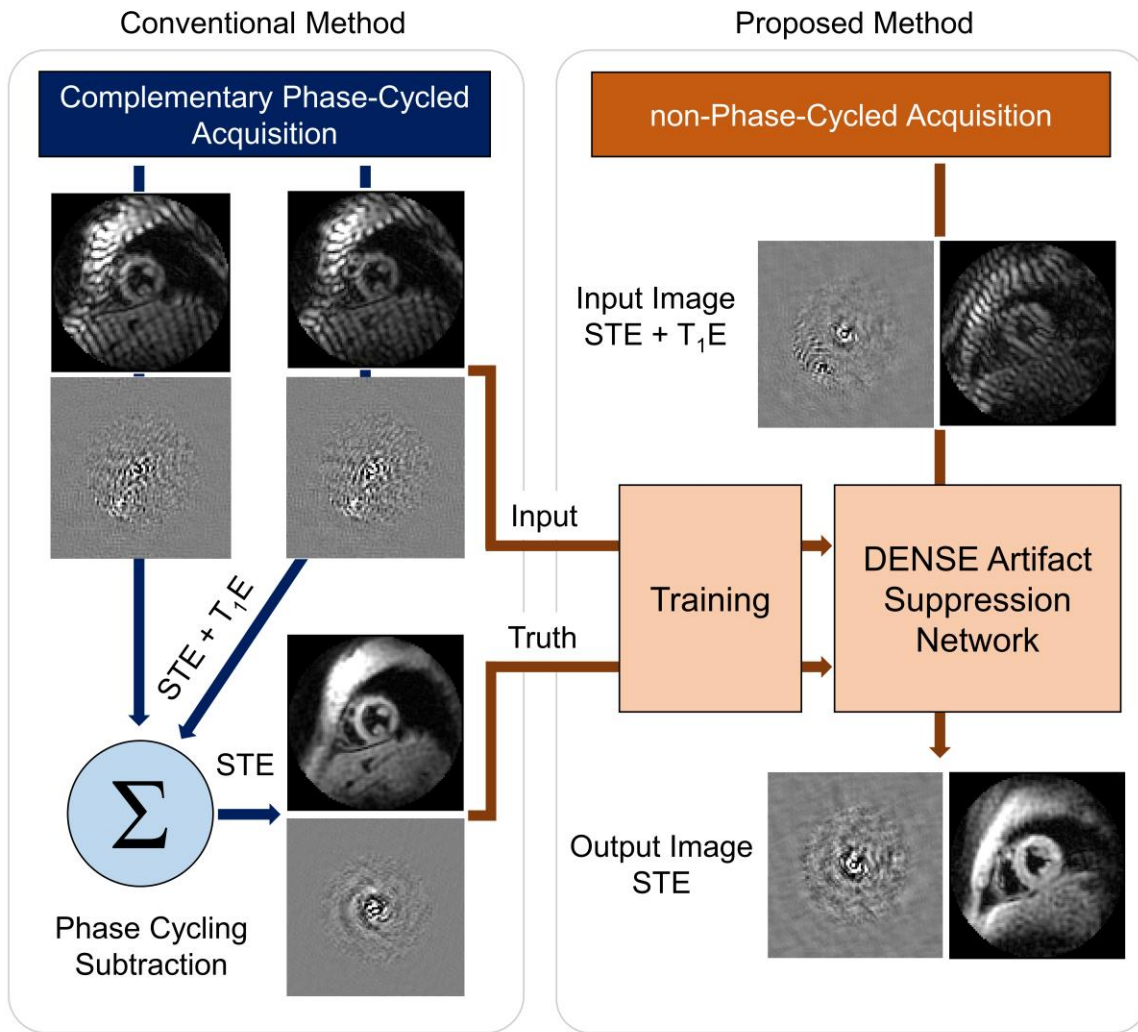


Figure 2.1 - Diagram illustrating the use of deep learning to suppress the artifact-generating T₁-echo (T₁E) in DENSE images. Artifact-free images with suppressed T₁-echoes obtained from complementary phase-cycled DENSE acquisitions were used to train the DAS-Net. Once trained, the DAS-Net takes non-phase-cycled images as input, and its output is a DENSE image where the T₁-echo and associated artifacts have been suppressed. STE: Stimulated echo.

2.3.1 U-Net design

A U-Net consisting of encoding and decoding paths, each with multiple convolutional layers, was used. Each layer consists of 3×3 convolutions followed by the sigmoid function. A 3×3 max pooling operator with stride 2 was used between convolutional layers of the encoding path. Prior to each convolutional layer in the decoding path, a 2×2 upsampling convolution was used and its outputs were concatenated with the output of the corresponding layer in the encoding path. The layers within the encoding path downsampled the input and increased the number of feature channels, and these operations were reversed in the decoding path. The convolutional and max-pooling operators had the same kernel size as those in the generic U-Net architecture. However, different numbers of convolutional layers and feature channels were chosen to avoid overfitting/underfitting.

For training, non-phase-cycled DENSE images were provided as the input and corresponding artifact-free DENSE images after subtraction of phase-cycled data were used as the ground-truth data. Training was posed as minimization of the absolute difference between the ground-truth and the output of the U-Net using the Adam optimizer. The training was implemented using the TensorFlow³² library on an NVIDIA TITAN Xp graphical processing unit.

2.3.2 Training dataset

A 3T scanner (Prisma, Siemens, Erlangen, Germany) with an 18-channel body phased-array RF coil was used to acquire images from 23 healthy volunteers (age= 28.7 ± 4.7 , 52% female). Informed consent was obtained from all subjects. A spiral cine DENSE sequence^{33,34} with prospective cardiac gating was employed for breath-hold scans with the following parameters: slice thickness = 8 mm, variable flip angle with final $\alpha=15^\circ$, field-of-view= 200×200 mm² (with outer volume suppression), spiral readout length=5.6 ms, in-plane spatial resolution= 3.4×3.4 mm², TR=15 ms, and TE=1.26 ms. Balanced 3-point displacement encoding³⁵ was used for in-plane 2D

displacement measurements. Four spiral interleaves per image with 2 interleaves acquired per heartbeat provided a temporal resolution of 30 ms. Phase-cycling was used to suppress the T_1 -echo. With two heartbeats to acquire field maps, the total scan time per slice was 14 heartbeats (14-HB protocol). The spiral multi-coil cine DENSE data were gridded using the non-uniform fast Fourier transform³⁶ and were adaptively combined³⁷.

Short-axis images from 17 subjects were used for training. For each subject, 6 slices were acquired, each with 20-27 cardiac phases. For each slice, displacement encoding in three directions (three-point displacement encoding) was used to measure two-dimensional in-plane displacements and perform correction for non-zero background phase. Also, for each slice, images were acquired using three different displacement-encoding frequencies: $k_e=0.06$, $k_e=0.08$, and $k_e=0.10$ cyc/mm. With these parameters, we define a dataset as the multiphase images corresponding to each slice, displacement-encoding frequency, and displacement-encoding direction. This yields a total of $N=918$ datasets (17 subjects \times 6 slices/subject \times 3 encoding frequencies/slice \times 3 encoding directions/slice). Each dataset is of size $(94 \times 94 \times 20)$, as each image is a 94×94 matrix, and we used 20 cardiac phases (the minimum number of phases from the 17 subjects studied).

2.3.3 Determination of the optimal training domain

As 2D planes are the input to the U-Net, we investigated whether any particular 2D data representation would be advantageous. We hypothesized that the k - t domain, which shows the different temporal dynamics of the T_1 -echo vs. the stimulated echo, would lead to better signal separation than other domains. To test this hypothesis, $N=108$ datasets from six subjects acquired with $k_e=0.06$ cyc/mm were divided into training ($N_{TR}=66$), validation ($N_{VL}=12$), and test ($N_{TS}=30$) subsets. To accommodate for unseen geometries, spatial translations and rotations were used to augment the training subset. Each DENSE dataset with size of $(94 \times 94 \times 20)$ was formatted into the

spatial domain, the k-space domain, and the k-space-time domain (k-t) as 2D planes with sizes 94×94 , 94×94 and 94×20 respectively, and these data were used to train three U-Nets: UN_{xy} , UN_{kk} and UN_{kt} , respectively. This approach provided $N=10560$ training planes for the spatial and k-space domains and $N=49,632$ training planes for the k-t domain. The complex data were converted to real-valued data by separating the real and imaginary parts. The number of convolutional layers (n_L) and initial feature channels (n_F) were chosen empirically as $(n_L=2, n_F=24)$, $(n_L=2, n_F=16)$ and $(n_L=3, n_F=32)$ for UN_{xy} , UN_{kk} and UN_{kt} , respectively. After training, each U-Net was evaluated using the testing subset. The root mean squared error³⁸ (RMSE) and structural similarity index³⁹ (SSIM) applied to concatenated real and imaginary parts of the images were used to quantify the performance of each network relative to the ground-truth images. End-systolic RMSE and SSIM were compared by one-way ANOVA and a post-hoc Tukey's test.

2.3.4 Data augmentation with remodulation of the displacement-encoding frequency

As the displacement-encoding frequency, k_e , is a user-selectable parameter, the DAS-Net should be trained to suppress the T_1 -echo for any typical value of k_e . While we acquired DENSE images with three different encoding frequencies, it is not practical to acquire images with all possible encoding frequencies. Instead, we developed a data augmentation method to synthesize any encoding frequency from authentic images. For DENSE images, this method isolates each echo (the stimulated echo and T_1 -echo) using a linear combination of phase-cycled data as previously described³⁵. Then, the phases of the images corresponding to the isolated stimulated echo and T_1 -echo are multiplied by a constant c_r . A new dataset is formed by summing the manipulated stimulated echo and T_1 -echo, where the new dataset has an encoding frequency of $k_e c_r$. As this process mimics the use of a different displacement-encoding frequency, we refer to c_r

as the remodulation constant. To describe the effect of frequency remodulation, we employ the DENSE signal model¹¹ that relates the DENSE signals in the image and k-space domains as:

$$c_1 m_{STE}(r) e^{-i2\pi k_e \Delta r} + c_2 m_{T_1E}(r) e^{-i2\pi k_e (r + \Delta r)} \stackrel{F}{\Leftrightarrow} c_1 M_{STE}(k) * \delta(k) + c_2 M_{T_1E}(k) * \delta(k - k_e) \quad (2.1)$$

where r is the tissue position, Δr is the tissue displacement, m_{STE} and m_{T_1E} are the magnitudes of the stimulated echo and T₁-echo, respectively, c_1 and c_2 are constants associated with the acquisition parameters, F denotes the Fourier transform, M_{STE} and M_{T_1E} are the Fourier transforms of m_{STE} and m_{T_1E} , respectively, and δ is the Dirac delta function. The augmented version of the DENSE signal after remodulation can be described in the image and k-space domains as:

$$c_1 m_{STE}(r) e^{-i2\pi c_r k_e \Delta r} + c_2 m_{T_1E}(r) e^{-i2\pi c_r k_e (r + \Delta r)} \stackrel{F}{\Leftrightarrow} c_1 M_{STE}^r(k) * \delta(k) + c_2 M_{T_1E}^r(k) * \delta(k - c_r k_e) \quad (2.2)$$

In the augmented DENSE signal, the phase of the stimulated echo is proportional to $c_r k_e \Delta r$ instead of $k_e \Delta r$ and the k-space location of the T₁-echo is shifted by $k_e(c_r - 1)$.

Because frequency remodulation is a new data augmentation method, we investigated whether the method improves U-Net training. Three U-Nets with three different datasets were trained: UN₃₀ was trained using 30 authentic datasets with $k_e=0.06$ cyc/mm, UN₆₀ was trained using 30 authentic datasets with $k_e=0.06$ cyc/mm and 30 authentic datasets with $k_e=0.1$ cyc/mm, and UN_{30A} was trained using 30 authentic datasets with $k_e=0.06$ cyc/mm and 30 synthetic datasets with $k_e=0.1$ cyc/mm, where the synthetic datasets were computed using the frequency remodulation method. The three U-Nets were evaluated on a test subset containing authentic datasets with $k_e=0.06$ cyc/mm (N=6) and 0.10 cyc/mm (N=6). The RMSE and SSIM of end-systolic images were used to compare the networks using one-way ANOVA and a post-hoc Tukey's test.

2.3.5 DENSE artifact suppression network

After determining the optimal training domain and developing a data augmentation method, we trained the U-Net using larger and more diverse datasets. A total of 918 authentic datasets with $k_e=0.06$ (N=306), 0.08 (N=306) and 0.10 (N=306) cyc/mm and 612 synthetic datasets with $k_e=0.07$ and 0.09 cyc/mm were used for training in the k-t domain. After data augmentation, 575,280 k-t planes were provided for training. The final U-Net is referred to as the DENSE artifact suppression network (DAS-Net).

2.3.6 Comparison to k-space zero-filling

Since harmonic phase (HARP)^{40,41} MRI has previously employed k-space zero-filling to suppress unwanted signals, as a comparison to the DAS-Net method, we employed zero-filling as an alternative method. For zero-filling, a circular region with a diameter of 20 pixels around the T₁-echo center was replaced with zeros in k-space. The performance of DAS-Net and zero-filling were evaluated on test datasets with $k_e=0.06$ cyc/mm (N=30 datasets) and $k_e=0.10$ cyc/mm (N=30 datasets). A two-sided t-test was employed to compare the end-systolic RMSE and SSIM.

2.3.7 Evaluation of the method using DENSE data without phase-cycling

Non-phase-cycled and phase-cycled DENSE images were acquired from six healthy human subjects using $k_e=0.06$ and 0.09 cyc/mm. Elimination of phase-cycling while keeping all other acquisition parameters unchanged led to a new 8-heartbeat protocol (8-HB protocol), rather than 14 heartbeats.

The non-phase-cycled images were passed through the DAS-Net to suppress the T₁-echo. The 8-HB protocol DAS-Net images and the reference standard images underwent segmental strain analysis using well-established methods⁴²⁻⁴⁴, and were compared using Bland-Altman analysis of end-systolic strain. Also, the Intra-class Correlation Coefficient (ICC) and Coefficient

of Variation (CoV)^{45,46} were calculated for circumferential and radial strain. For ICC, agreement was considered as excellent (ICC \geq 0.75), good (ICC 0.6–0.74), fair (ICC 0.4–0.59), or poor (ICC $<$ 0.40)^{45–47}.

The signal-to-noise ratio (SNR) of DAS-Net processed images was assessed and compared to that of phase-cycled images. As DENSE measures displacement using the myocardial phase, we measured the phase SNR⁴⁸ that was computed as described in equation (2.3)⁴⁹.

$$phase\ SNR = \left\| \frac{mean(unwrapped\ phase\ of\ end - systolic\ ROI)}{stdev(phase\ of\ end - diastolic\ myocardium)} \right\| \quad (2.3)$$

where the mean unwrapped phase of an end-systolic region of interest (ROI) measures the DENSE phase in the region with greatest displacement (representing the signal of interest), and the standard deviation of the phase of the end-diastolic myocardium provides a measure of the standard deviation of phase at a cardiac frame where the mean phase is essentially zero.

The image quality of DAS-Net processed and phase-cycled magnitude DENSE images was assessed by two experts, F.H.E and K.C.B, with 30 and 20 years of experience, respectively. Cine movies were presented in a random order and were rated using a 5-point scale with 5 indicating highest quality and 1 indicating poor quality. A Wilcoxon Rank-Sum test was performed on paired scores with the null hypothesis that the means of the scores were different.

2.4 Results

2.4.1 *k-t is the optimal training domain*

Figure 2.2 illustrates examples of artifact suppression using UN_{kt}, UN_{xy} and UN_{kk} and summarizes the RMSE and SSIM results. The images from UN_{kt} had the lowest RMSE (RMSE=7.0 \pm 1.4, 8.7 \pm 1.8, and 9.3 \pm 2.1 for UN_{kt}, UN_{xy}, and UN_{kk}, respectively, p $<$ 0.05) and the

highest SSIM (SSIM=0.79±0.03, 0.76±0.03, and 0.74±0.05 for UN_{kt}, UN_{xy}, and UN_{kk}, respectively, p<0.05).

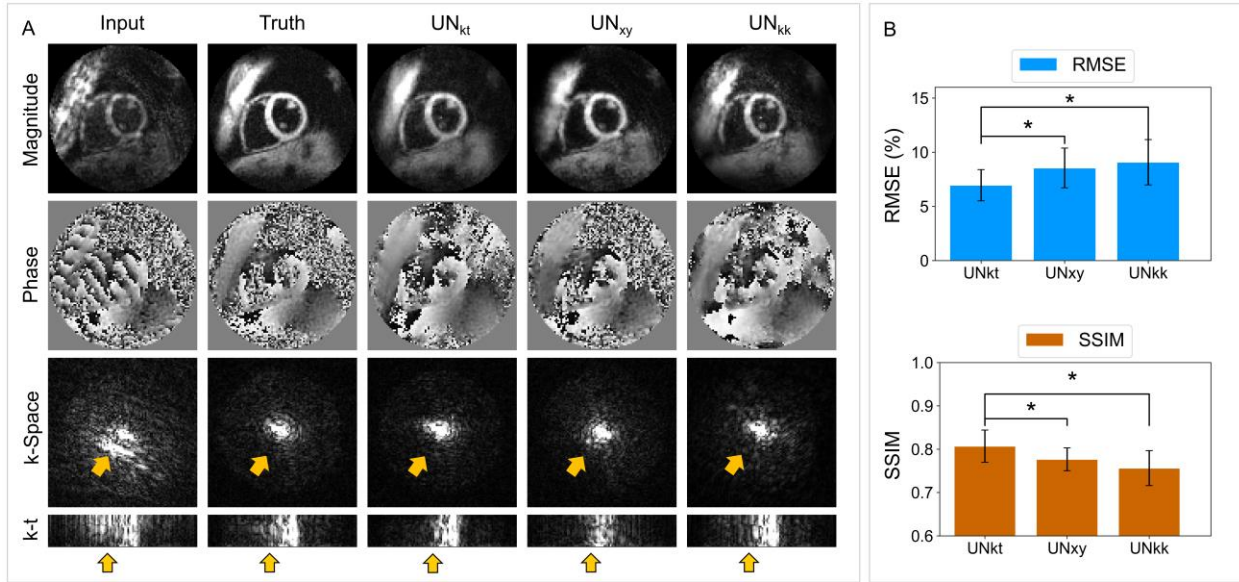


Figure 2.2 - U-Nets were trained using DENSE data formatted in *k-t* planes (UN_{kt}), spatial planes (UN_{xy}), and *k-space* planes (UN_{kk}). A) An example showing DENSE magnitude and phase images, the *k-space* magnitude data, and *k-t* planes after application of the UN_{kt}, UN_{xy} and UN_{kk} U-Nets. B) Bar-plots and error bars (representing the standard deviation) of RMSE and SSIM computed from the output of each U-Net and the ground-truth data for end-systolic images of *N*=30 test datasets show that the UN_{kt} network provides the best performance.

2.4.2 Data augmentation with remodulation of the displacement-encoding frequency enhances

*T*₁-echo suppression

Figure 2.3.A shows an example of synthetic DENSE images generated using remodulation of the displacement-encoding frequency. The original version of the image is also shown, as is an authentic image using the higher encoding frequency. Figure 2.3.B summarizes the evaluation of the UN₃₀, UN_{30A} and UN₆₀ on the test images. RMSE and SSIM show three findings: first, the UN_{30A} and UN₆₀ outperform UN₃₀ based on RMSE (RMSE=8.07±0.74, 7.13±0.53, and 7.07±0.52 for UN₃₀, UN_{30A} and UN₆₀, respectively, p<0.05) and SSIM (SSIM=0.78±0.02, 0.81±0.02, and 0.82±0.02 for UN₆₀, UN_{60A} and UN₁₂₀, respectively, p<0.05). Second, the performance of UN₆₀ is

almost identical to that of UN_{30A}. Third, the three networks performed better with $k_e = 0.10$ cyc/mm compared to 0.06 cyc/mm.

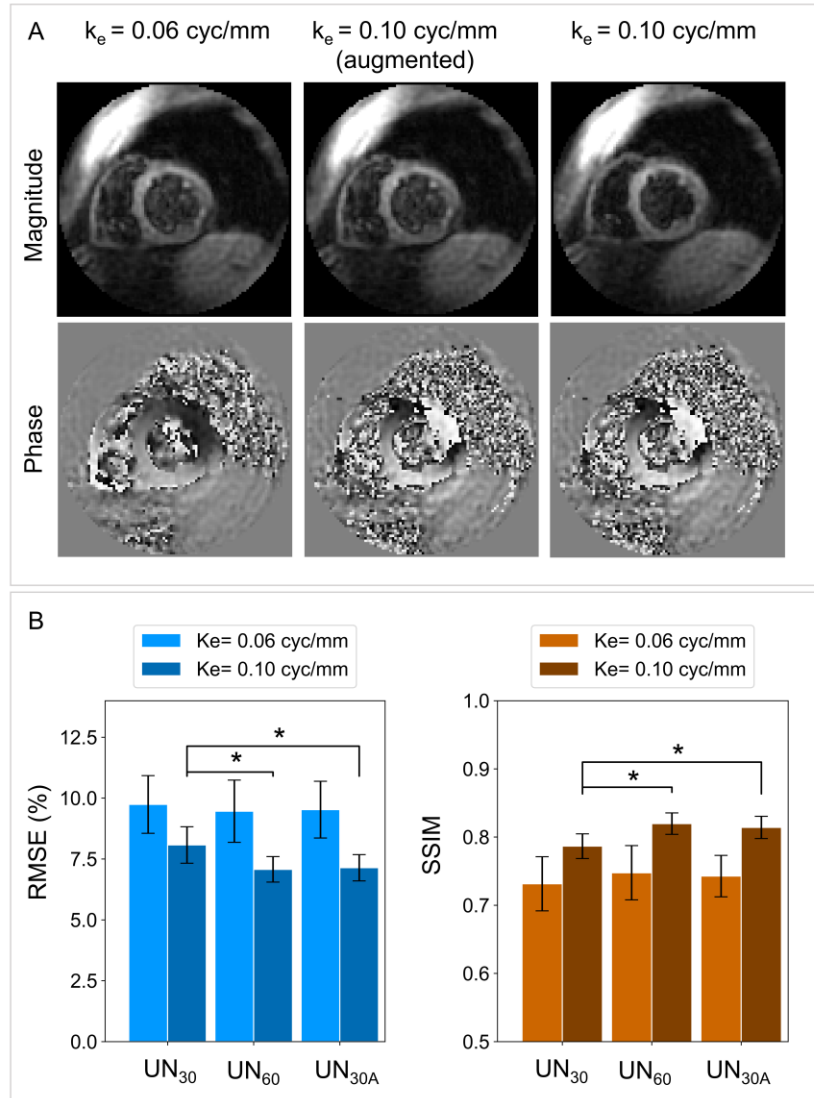


Figure 2.3 - Demonstration of data augmentation using remodulation of the displacement-encoding frequency. A) Authentic data are shown in left column of (A), acquired with an encoding frequency of 0.06 cycles/mm. Using the frequency remodulation method, the authentic data in the left column was phase remodulated to generate the synthetic image shown in the middle column, with encoding frequency of 0.10 cycles/mm. Compared to the authentic image, the synthetic image are reasonably realistic. B) Training a U-Net with 30 authentic and 30 augmented datasets (UN_{30A}) results in lower RMSE and higher SSIM than training with only 30 authentic datasets (UN₃₀), and provides similar RMSE and SSIM as training with 60 authentic datasets (UN₆₀). The error bars represent standard deviation.

2.4.3 DAS-Net outperforms *k*-space zero-filling

Relative to the ground-truth, for $k_e=0.10$ cyc/mm the DAS-Net achieved $RMSE=5.5\pm0.8$ and $SSIM=0.85\pm0.02$, and for $k_e=0.06$ cyc/mm the DAS-Net achieved $RMSE=6.0\pm1.8$ and $SSIM=0.82\pm0.04$. Figure 2.4 summarizes the comparison of the DAS-Net and k-space zero-filling. The example images from DAS-Net are more similar to the ground-truth images compared to those of k-space zero-filling. DAS-Net showed significantly better performance than zero-filling with regard to RMSE (5.8 ± 1.5 vs 13.5 ± 1.5 , DAS-Net vs zero-filling, $p<0.01$) and SSIM (0.83 ± 0.04 vs 0.66 ± 0.03 , DAS-Net vs zero-filling, $p<0.01$).

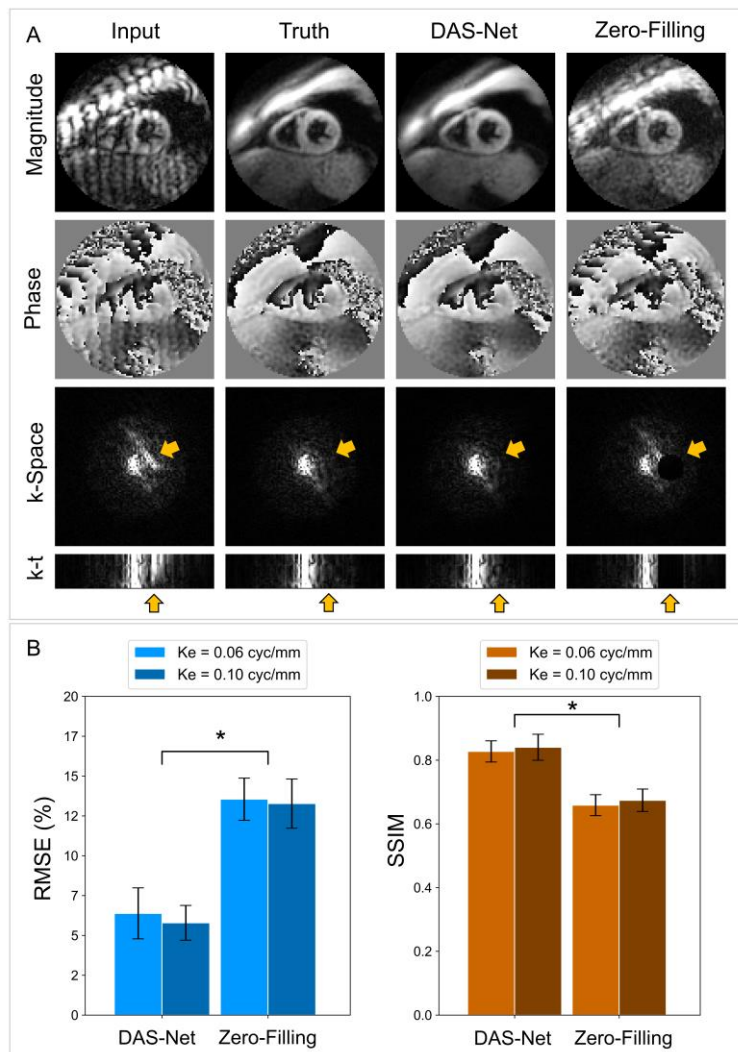


Figure 2.4 - The DAS-Net is effective for suppression of the T_1 -echo. In (A), example magnitude images, phase images, k-space data, and k-t planes are shown for input images, ground truth using phase-cycling, DAS-Net, and images after

k-space zero-filling. As observed in (A) and quantified for all datasets in (B), the DAS-Net provided lower RMSE and higher SSIM values than zero-filling.

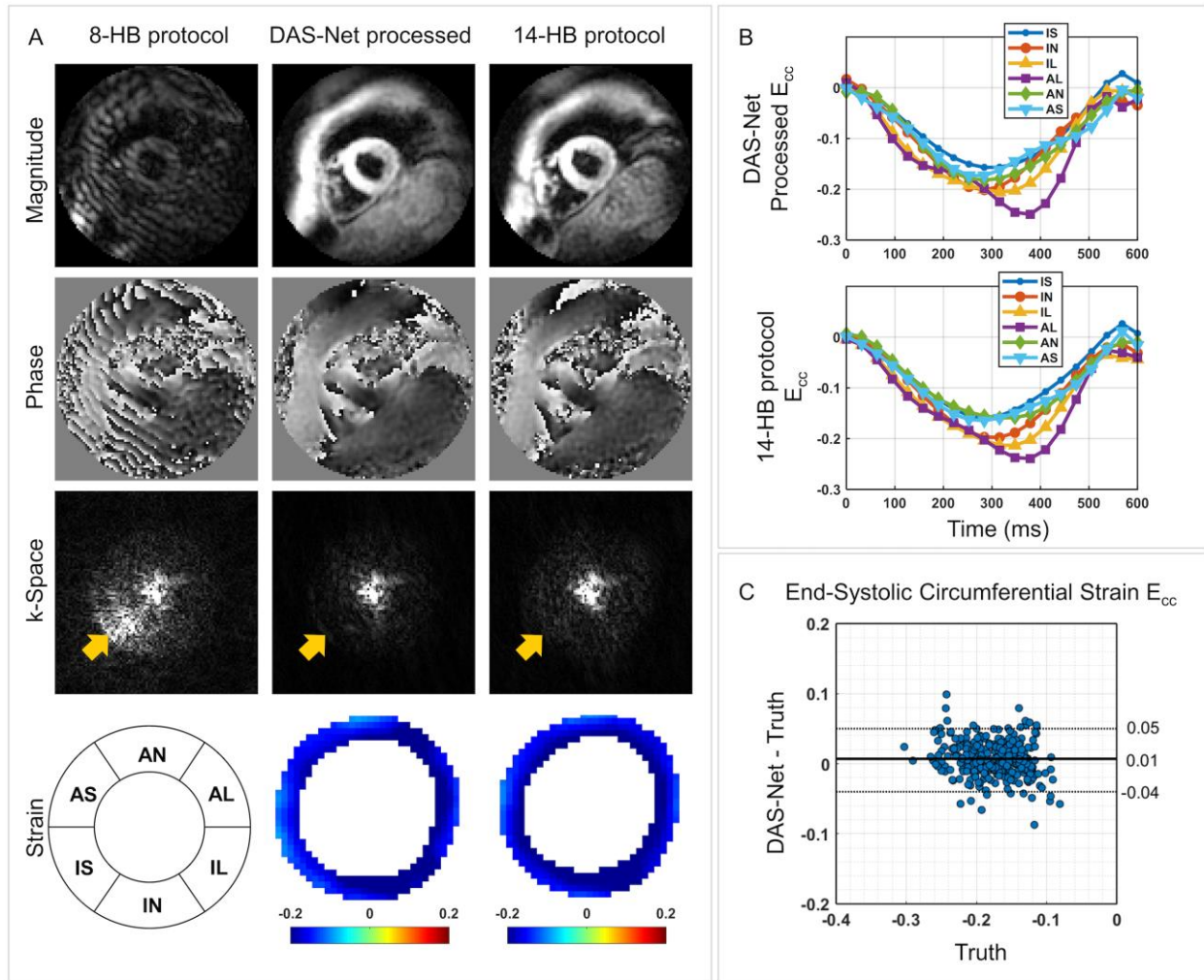


Figure 2.5 - Circumferential strain measurements are similar for non-phase-cycled DENSE images using DAS-Net for T_1 -echo suppression (8-heartbeat protocol) and phase-cycled DENSE images (14-heartbeat protocol). (A) Example magnitude images, phase images, and *k*-space data are shown for the 8-heartbeat protocol without DAS-Net processing (8-HB protocol), the 8-heartbeat protocol with DAS-Net processing (8HB DAS-Net processed), and the 14-heartbeat protocol with phase-cycling (14-HB protocol). The end-systolic circumferential strain maps of the DAS-Net processed and the 14-heartbeat protocol data are shown in the bottom row. (B) Multiphasic segmental circumferential strain-time curves of the DAS-Net processed 8-HB protocol and the 14-HB protocol images are shown. (C) Bland-Altman analysis shows good agreement between the 8HB DAS-Net processed and 14-HB protocols for end-systolic segmental circumferential strain (E_{cc}) from the six test subjects.

2.4.4 Strain data from non-phase-cycled images processed by DAS-Net are in close agreement with ground-truth

Figure 2.5.A illustrates example images acquired with (a) the 8-HB protocol (without DAS-Net processing), (b) the 8-HB protocol and application of the DAS-Net, and (c) the 14-HB standard protocol. The corresponding multiphasic circumferential strain (E_{cc})-time curves and end-systolic E_{cc} maps are presented in Figure 2.5.B. Figure 2.5.C shows a Bland-Altman analysis comparing the DAS-Net processed 8-HB protocol and the 14-HB protocol for the assessment of segmental end-systolic E_{cc} from six subjects, demonstrating close agreement. The radial strain comparisons are included in Figure 2.6. The ICC and CoV were 0.76 and -0.13 for circumferential strain, respectively, and 0.72 and 0.28 for radial strain, respectively.

The phase SNR of the DAS-Net processed and phase-cycled images were 32.32 ± 12.84 and 33.39 ± 12.89 , respectively for images with $k_e=0.06$ cyc/mm, and 35.20 ± 16.03 and 39.54 ± 17.60 , respectively, for $k_e=0.09$ cyc/mm; showing 3% and 10% reductions, respectively, in SNR of DAS-net processed images.

The image quality scores for DAS-Net processed and phase-cycled images were 3.59 ± 0.91 and 3.44 ± 0.75 , respectively, with $p=0.22$, indicating similar image quality of the two methods.

2.5 Discussion

The major finding of this study is that deep learning can effectively perform signal separation for cine DENSE, isolating the displacement-encoded stimulated echo and suppressing the artifact-generating T_1 -echo without employing methods based on MRI physics. After training the DAS-Net and achieving good performance for test data, we demonstrated its use by acquiring accurate cine DENSE strain data without phase-cycling, shortening the scan time from 14 to 8 heartbeats.

We compared network training in various domains and achieved the best performance using the k-t domain. The temporal dynamics captured in the k-t domain may contribute to better

performance compared to the spatial and k-space domains. Alternatively, 3-dimensional^{50,51} and 2+1-dimensional⁵¹ networks may be used to incorporate the both spatial and time dimensions.

The quality of T_1 -echo suppression depends on the k-space location of the T_1 -echo. The DAS-Net showed better performance for higher displacement encoding frequencies, likely due to greater spacing between echo centers in k-space, making the signal separation task easier.

We employed a novel data augmentation strategy using remodulation of the displacement-encoding frequency. While our authentic training data were acquired with three different displacement-encoding frequencies, a design feature of the DAS-Net is that it should be able to suppress the T_1 -echo for any displacement-encoding frequency. We developed the frequency remodulation method to provide training data with arbitrary displacement-encoding frequency. Our results showed that with the augmented data, lower RMSE and higher SSIM were achieved. We compared the DAS-Net to k-space zero-filling, for this signal separation task. Zero-filling showed worse performance as assessed by RMSE and SSIM, demonstrating the difficulty of the problem for conventional methods and the capabilities of deep learning to solve this challenging problem.

While this study applied deep learning to DENSE, similar methods could be applied to HARP imaging⁴⁰, where k-space filters are used to suppress various signals; however, they degrade spatial resolution. Our results suggest that deep learning could improve HARP by suppressing signals and preserving spatial resolution.

We had anticipated that the 8-HB protocol with DAS-Net processing would lead to a 40% decrease in SNR compared to the phase-cycled 14-HB protocol, as phase-cycling provides signal averaging of the stimulated echo in addition to suppression of the T_1 -echo. However, we measured

just a 3-10% SNR reduction. We attribute this finding to DAS-Net denoising, as previously shown for CNNs⁵².

Limitations of this study were that DENSE images were acquired using only 3T scanners from a single vendor and included only healthy volunteers. DAS-Net may not perform as well using different field strengths such as 1.5T because SNR is generally lower at 1.5T, T_1 values are different, and off-resonance effects are different. Also, training data from just 17 subjects were employed. Better and more generalized DAS-Net performance would likely be achieved by retraining using data from 1.5T and more subjects. In addition, the U-Net trained in the k-t domain requires a consistent number of cardiac phases and we used the minimum number of 20 phases from all datasets. This limitation can be obviated by incorporating time using CNNs with 3D convolutions.

In conclusion, the DAS-Net provides an effective alternative to phase-cycling for suppression of the T_1 -echo in DENSE MRI. Artifact suppression with DAS-Net enabled the elimination of phase-cycling and provides a 42% reduction in the acquisition time. The approach may be extended in the future to suppress the T_1 -echo and conjugate stimulated echo, potentially leading to faster 3D DENSE³³.

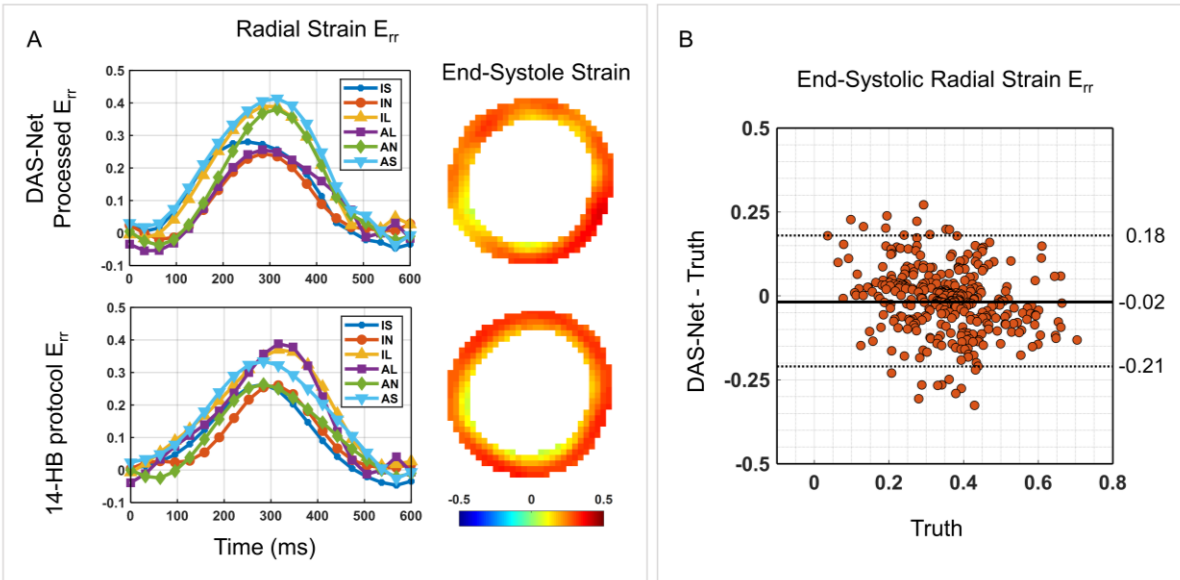


Figure 2.6 - (A) Example multiphasic segmental radial strain (E_{rr})-time curves from the DAS-Net processed 8-HB protocol and the 14-HB protocol are shown, as are example end-systolic radial strain maps. (B) The Bland-Altman analysis for segmental end-systolic E_{rr} for the six test subjects is shown

2.6 References

1. Kim D, Gilson WD, Kramer CM, Epstein FH. Myocardial tissue tracking with two-dimensional cine displacement-encoded MR imaging: development and initial evaluation. *Radiology*. 2004;230(3):862-871.
2. Auger DA, Bilchick KC, Gonzalez JA, et al. Imaging left-ventricular mechanical activation in heart failure patients using cine DENSE MRI: Validation and implications for cardiac resynchronization therapy. *J Magn Reson Imaging*. 2017;46(3):887-896.
3. Feng L, Donnino R, Babb J, Axel L, Kim D. Numerical and in vivo validation of fast cine displacement-encoded with stimulated echoes (DENSE) MRI for quantification of regional cardiac function. *Magn Reson Med An Off J Int Soc Magn Reson Med*. 2009;62(3):682-690.
4. Bilchick KC, Auger DA, Abdishektaei M, et al. CMR DENSE and the Seattle Heart Failure

- Model Inform Survival and Arrhythmia Risk After CRT. *JACC Cardiovasc Imaging*. 2020;13(4):924-936. doi:10.1016/j.jcmg.2019.10.017
5. Zhong X, Meyer CH, Schlesinger DJ, et al. Tracking brain motion during the cardiac cycle using spiral cine-DENSE MRI. *Med Phys*. 2009;36(8):3413-3419.
 6. Lin AP, Bennett E, Wisk LE, Gharib M, Fraser SE, Wen H. Circumferential strain in the wall of the common carotid artery: Comparing displacement-encoded and cine MRI in volunteers. *Magn Reson Med An Off J Int Soc Magn Reson Med*. 2008;60(1):8-13.
 7. Zhong X, Epstein FH, Spottiswoode BS, Helm PA, Blemker SS. Imaging two-dimensional displacements and strains in skeletal muscle during joint motion by cine DENSE MR. *J Biomech*. 2008;41(3):532-540.
 8. Zhong X, Spottiswoode BS, Cowart EA, Gilson WD, Epstein FH. Selective suppression of artifact-generating echoes in cine DENSE using through-plane dephasing. *Magn Reson Med An Off J Int Soc Magn Reson Med*. 2006;56(5):1126-1131.
 9. Tsao J, Laurent D. N-SPAMM for efficient displacement-encoded acquisition in myocardial tagging. *Proc 13th Annu Meet ISMRM, Miami Beach, Florida, USA*. 2005;42(6):273.
 10. Callot V, Bennett E, Decking UKM, Balaban RS, Wen H. In vivo study of microcirculation in canine myocardium using the IVIM method. *Magn Reson Med An Off J Int Soc Magn Reson Med*. 2003;50(3):531-540.
 11. Epstein FH, Gilson WD. Displacement-encoded cardiac MRI using cosine and sine modulation to eliminate (CANSEL) artifact-generating echoes. *Magn Reson Med*. 2004;52(4):774-781. doi:10.1002/mrm.20232
 12. Aletras AH, Wen H. Mixed echo train acquisition displacement encoding with stimulated echoes: an optimized DENSE method for in vivo functional imaging of the human heart.

- Magn Reson Med An Off J Int Soc Magn Reson Med.* 2001;46(3):523-534.
13. Cai X, Epstein FH. Free-breathing cine DENSE MRI using phase cycling with matchmaking and stimulated-echo image-based navigators. *Magn Reson Med.* 2018;80(5):1907-1921.
 14. Hoshen Y. Towards unsupervised single-channel blind source separation using adversarial pair unmix-and-remix. In: *ICASSP 2019-2019 IEEE International Conference on Acoustics, Speech and Signal Processing (ICASSP)*. IEEE; 2019:3272-3276.
 15. Chandna P, Miron M, Janer J, Gómez E. Monoaural audio source separation using deep convolutional neural networks. In: *International Conference on Latent Variable Analysis and Signal Separation*. Springer; 2017:258-266.
 16. Zhang X, Ng R, Chen Q. Single image reflection separation with perceptual losses. In: *Proceedings of the IEEE Conference on Computer Vision and Pattern Recognition.* ; 2018:4786-4794.
 17. Wang D, Chen J. Supervised speech separation based on deep learning: An overview. *IEEE/ACM Trans Audio, Speech, Lang Process.* 2018;26(10):1702-1726.
 18. Ryu K, Nam Y, Gho SM, et al. Data-driven synthetic MRI FLAIR artifact correction via deep neural network. *J Magn Reson Imaging.* 2019;50(5):1413-1423. doi:10.1002/jmri.26712
 19. Gurbani SS, Schreiber E, Maudsley AA, et al. A convolutional neural network to filter artifacts in spectroscopic MRI. *Magn Reson Med.* 2018;80(5):1765-1775. doi:10.1002/mrm.27166
 20. Hales PW, Pfeuffer J, A. Clark C. Combined Denoising and Suppression of Transient Artifacts in Arterial Spin Labeling MRI Using Deep Learning. *J Magn Reson Imaging.*

- 2020;52(5):1413-1426. doi:10.1002/jmri.27255
21. Oh G, Lee JE, Ye JC. Unsupervised MR Motion Artifact Deep Learning using Outlier-Rejecting Bootstrap Aggregation. 2020:1-10. <http://arxiv.org/abs/2011.06337>.
 22. Qing L, Hongming S, Xie Y, Debiao L, Wang G. Cine Cardiac MRI Motion Artifact Reduction Using a Recurrent Neural Network. *arXiv*. 2020:1-10.
 23. Zhao Y, Ossowski J, Wang X, et al. Localized Motion Artifact Reduction on Brain MRI Using Deep Learning with Effective Data Augmentation Techniques. *arXiv*. 2020.
 24. Armanious K, Gatidis S, Nikolaou K, Yang B, Thomas K. RETROSPECTIVE CORRECTION OF RIGID AND NON-RIGID MR MOTION ARTIFACTS USING GANS University of Stuttgart , Institute of Signal Processing and System Theory , Stuttgart , Germany University of Tübingen , Department of Radiology , Tübingen 's College Lond. *IEEE 17th Int Symp Biomed Imaging*. 2020;(Isbi):1550-1554.
 25. Küstner T, Armanious K, Yang J, Yang B, Schick F, Gatidis S. Retrospective correction of motion-affected MR images using deep learning frameworks. *Magn Reson Med*. 2019;82(4):1527-1540.
 26. Jiang W, Liu Z, Lee K-H, et al. Respiratory Motion Correction in Abdominal MRI using a Densely Connected U-Net with GAN-guided Training. *arXiv e-prints*. June 2019:arXiv:1906.09745.
 27. Tamada D, Kromrey M-L, Ichikawa S, Onishi H, Motosugi U. Motion Artifact Reduction Using a Convolutional Neural Network for Dynamic Contrast Enhanced MR Imaging of the Liver. *Magn Reson Med Sci*. 2020;19(1):64-76. doi:10.2463/mrms.mp.2018-0156
 28. Duffy BA, Zhang W, Tang H, et al. Retrospective correction of motion artifact affected structural MRI images using deep learning of simulated motion. *Med Imaging with Deep*

- Learn.* 2018;(Midl 2018):1-8.
29. Qin C, Schlemper J, Caballero J, Price AN, Hajnal J V., Rueckert D. Convolutional recurrent neural networks for dynamic MR image reconstruction. *arXiv.* 2017;38(1):280-290.
 30. Kwon K, Kim D, Kim B, Park HW. Unsupervised learning of a deep neural network for metal artifact correction using dual-polarity readout gradients. *Magn Reson Med.* 2020;83(1):124-138. doi:10.1002/mrm.27917
 31. Ronneberger O, Fischer P, Brox T. U-net: Convolutional networks for biomedical image segmentation. In: *International Conference on Medical Image Computing and Computer-Assisted Intervention.* ; 2015:234-241.
 32. Abadi M, Barham P, Chen J, et al. Tensorflow: A system for large-scale machine learning. In: *12th {USENIX} Symposium on Operating Systems Design and Implementation ({OSDI} 16).* ; 2016:265-283.
 33. Zhong X, Spottiswoode BS, Meyer CH, Kramer CM, Epstein FH. Imaging three-dimensional myocardial mechanics using navigator-gated volumetric spiral cine DENSE MRI. *Magn Reson Med.* 2010;64(4):1089-1097.
 34. Tayal U, Wage R, Ferreira PF, et al. The feasibility of a novel limited field of view spiral cine DENSE sequence to assess myocardial strain in dilated cardiomyopathy. *Magn Reson Mater Physics, Biol Med.* 2019;32(3):317-329. doi:10.1007/s10334-019-00735-5
 35. Zhong X, Helm PA, Epstein FH. Balanced Multipoint Displacement Encoding for DENSE. 2009;988:981-988. doi:10.1002/mrm.21851
 36. Fessler JA. On NUFFT-based gridding for non-Cartesian MRI. *J Magn Reson.* 2007;188(2):191-195.

37. Walsh DO, Gmitro AF, Marcellin MW. Adaptive reconstruction of phased array MR imagery. *Magn Reson Med An Off J Int Soc Magn Reson Med*. 2000;43(5):682-690.
38. Otazo R, Kim D, Axel L, Sodickson DK. Combination of compressed sensing and parallel imaging for highly accelerated first-pass cardiac perfusion MRI. *Magn Reson Med*. 2010;64(3):767-776.
39. Wang Z, Bovik AC, Sheikh HR, Simoncelli EP. Image quality assessment: from error visibility to structural similarity. *Image Process IEEE Trans*. 2004;13(4):600-612.
40. Osman NF, Kerwin WS, McVeigh ER, Prince JL. Cardiac motion tracking using CINE harmonic phase (HARP) magnetic resonance imaging. *Magn Reson Med An Off J Int Soc Magn Reson Med*. 1999;42(6):1048-1060.
41. Sampath S, Derbyshire JA, Atalar E, Osman NF, Prince JL. Real-time imaging of two-dimensional cardiac strain using a harmonic phase magnetic resonance imaging (HARP-MRI) pulse sequence. *Magn Reson Med*. 2003;50(1):154-163. doi:10.1002/mrm.10509
42. Spottiswoode BS, Zhong X, Hess AT, et al. Tracking myocardial motion from cine DENSE images using spatiotemporal phase unwrapping and temporal fitting. *IEEE Trans Med Imaging*. 2006;26(1):15-30.
43. Spottiswoode BS, Zhong X, Lorenz CH, Mayosi BM, Meintjes EM, Epstein FH. Motion-guided segmentation for cine DENSE MRI. *Med Image Anal*. 2009;13(1):105-115.
44. Gilliam A, Suever J. 2D Cine DENSE Post-Processing Software. <https://github.com/denseanalysis/denseanalysis>. Published 2016.
45. Schmidt B, Dick A, Treutlein M, et al. Intra- and inter-observer reproducibility of global and regional magnetic resonance feature tracking derived strain parameters of the left and right ventricle. *Eur J Radiol*. 2017;89:97-105. doi:10.1016/j.ejrad.2017.01.025

46. Swoboda PP, Larghat A, Zaman A, et al. Reproducibility of myocardial strain and left ventricular twist measured using complementary spatial modulation of magnetization. *J Magn Reson Imaging*. 2014;39(4):887-894. doi:10.1002/jmri.24223
47. Khan JN, Singh A, Nazir SA, Kanagala P, Gershlick AH, McCann GP. Comparison of cardiovascular magnetic resonance feature tracking and tagging for the assessment of left ventricular systolic strain in acute myocardial infarction. *Eur J Radiol*. 2015;84(5):840-848. doi:10.1016/j.ejrad.2015.02.002
48. Lee AT, Bruce Pike G, Pelc NJ. Three-point phase-contrast velocity measurements with increased velocity-to-noise ratio. *Magn Reson Med*. 1995;33(1):122-126.
49. Ghadimi S, Auger DA, Feng X, Sun C, Meyer CH, Bilchick KC, Cao JJ, Scott, AD, Oshinski JN, Ennis DB EF. Fully-automated global and segmental strain analysis of DENSE cardiac MRI using deep learning for segmentation and phase unwrapping (Accepted). *J Cardiovasc Magn Reson*. 2020.
50. Milletari F, Navab N, Ahmadi S-A. V-net: Fully convolutional neural networks for volumetric medical image segmentation. In: *2016 Fourth International Conference on 3D Vision (3DV)*. ; 2016:565-571.
51. Tran D, Wang H, Torresani L, Ray J, LeCun Y, Paluri M. A closer look at spatiotemporal convolutions for action recognition. In: *Proceedings of the IEEE Conference on Computer Vision and Pattern Recognition*. ; 2018:6450-6459.
52. Jain V, Seung HS. Natural image denoising with convolutional networks. *Adv Neural Inf Process Syst 21 - Proc 2008 Conf*. 2009:769-776.

Chapter 3 : Compensation for Respiratory-Motion-Induced Signal Loss and Phase Corruption in Free-breathing Self-navigated Cine DENSE using Deep Learning

3.1 Abstract

Purpose: To introduce a mathematical model that describes artifacts due to encoding of respiratory motion into the phase of the stimulated echo and to use the model to develop a deep convolutional neural network for correcting the artifacts in self-navigated free-breathing cine DENSE.

Methods: The mathematical model describes the phase shifts of stimulated echoes due to breathing that corresponds to constant phase error in k-space. Phantom experiments and Bloch-equation simulations were performed to validate the model. The model was used along with the simulation of respiratory motion to generate synthetic images with phase shift artifacts to train a U-Net, DENSE-RESP-NET. Self-navigated free-breathing cine DENSE from healthy volunteers was used and processed by DENSE-RESP-NET to evaluate its performance using phase signal-to-noise ratio and strain analysis.

Results: Phantom experiments and Bloch-equation simulations showed that constant phase errors in segmented DENSE leads to signal loss in magnitude images and phase corruption in the phase images of the stimulated echo. However, these artifacts can be restored using known respiratory motion and the developed model. For self-navigated free-breathing DENSE where respiratory motion could not be accurately estimated, the DENSE-RESP-NET significantly

corrected the signal loss and phase corruption and provided reliable strain measurement for systolic and diastolic parameters.

Conclusion: DENSE-RESP-NET is an effective method to correct for breathing-associated constant phase errors. DENSE-RESP-NET in concert with self-navigated free-breathing DENSE images can provide reliable myocardial strain measurements.

3.2 Introduction

Cine displacement encoding with stimulated echoes (DENSE) is an accurate and reproducible method of myocardial strain imaging and provides automatic displacement and strain analysis¹⁻⁴. These properties have led to increasing clinical applications. For example, Bilchick et al. showed an important role of DENSE for prognostication in heart failure patients undergoing cardiac resynchronization therapy⁵, Mangion et al. showed the prognostic value of DENSE in acute myocardial infarction⁶, and Jing et al showed that DENSE detects systolic dysfunction in childhood obesity⁷. While these studies used breath-hold or navigator-based DENSE protocols, breath-holding is taxing for patients and diaphragm navigator methods are burdensome for technologists, prompting the need for self-navigated free-breathing DENSE⁸.

For DENSE imaging, three echoes are generated from the application of three RF pulses and the corresponding displacement-encoding gradient pulses⁹, namely (1) the displacement-encoded stimulated echo, (2) an echo due to T_1 relaxation (T_1 echo), and (3) the complex conjugate of the stimulated echo. While the stimulated echo is the desired signal as its phase is proportional to tissue displacement¹⁰, the other two echoes are generally considered to cause artifacts and should be suppressed^{9,11}. The T_1 echo is typically suppressed by combining two phase-cycled acquisitions^{12,13} and the complex conjugate echo is typically shifted outside of the acquisition window by using an appropriately large displacement-encoding frequency⁹.

Considering these echoes and suppression methods, in free-breathing DENSE respiratory motion can lead to three types of artifacts. The first type is striping artifacts due to imperfect suppression of the T_1 echo, as different tissue contributes to the T_1 echo during the different phase-cycled acquisitions¹⁴. The second type is blurring related to respiratory motion induced position shifts of the tissue and its magnetization, which correspond to (approximately) linear phase errors in k-space of the stimulated-echo signal. The third artifact type comes from a phase shift of the stimulated echo due to breathing (i.e., the breathing induced tissue displacement that is encoded into the phase of the stimulated echo). This image domain phase shift due to breathing corresponds to a constant phase error in k-space of the stimulated-echo signal and manifests as signal loss (as demonstrated later in this paper). The first and third artifact types are specific to stimulated-echo imaging. The second type of artifact is common among most MRI methods and is predicted and accounted for using conventional models that describe the effects of breathing in MRI¹⁴.

Prior work developing self-navigated DENSE introduced the match-making method⁸ which effectively deals with suppression of the T_1 echo in free-breathing phase-cycled DENSE and also employs stimulated-echo-based image navigators (ste-iNAVs) to estimate and correct for in-plane position shifts due to breathing (i.e., the first and second types of artifacts discussed above). However, the third type of artifact (encoding of respiratory motion into the phase of the stimulated echo) has yet to be well described and corrected.

In this paper we (1) present a new model that fully describes the effect of breathing in cine DENSE, and (2) develop a method for the correction of respiratory-induced constant phase shifts that can be combined with match-making and ste-iNAVs to enable accurate free-breathing self-navigated cine DENSE.

3.3 Theory

In DENSE, the acquired signal can be described by equation (3.1).

$$s(r) = \frac{1}{2}M(r) \sin(\alpha) e^{-\frac{t}{T_1}} e^{-i2\pi(k_e, \Delta r)} + M_0(r) \sin(\alpha) \left(1 - e^{-\frac{t}{T_1}}\right) e^{-i2\pi(k_e, r + \Delta r)} \quad (3.1)$$

where the first and the second terms describe the stimulated echo and the T_1 echo, respectively, M is the displacement-encoded longitudinal magnetization, M_0 is the longitudinal magnetization at thermal equilibrium, T_1 is the longitudinal relaxation time, k_e denotes the displacement encoding frequency vector, α is the flip angle of the RF excitation pulse, $\langle ., . \rangle$ denotes the dot product, r denotes the position of the tissue at the time of signal readout, and Δr is the displacement of the tissue during the time between application of the displacement-encoding pulses and the readout.

Diagrams of a short-axis view of the heart and motion and deformation of a small element of myocardium, as well as DENSE sequence diagrams, are illustrated in Figure 3.1.A and Figure 3.1.B, respectively, and show that, without respiratory motion, the stimulated-echo phase is proportional to $\Delta r = \Delta r^C$, where Δr^C represents displacement due to cardiac motion. For the case with both cardiac and respiratory motion (Figure 3.1.C), we define two displacements related to respiratory motion. First, Δr^{R_1} is defined as the in-plane translation of the myocardium due to breathing immediately prior to the application of the displacement-encoding pulses. Next, Δr^{R_2} is defined as the in-plane displacement due to breathing during the time between application of the displacement-encoding pulses and the readout. With these definitions, equation (3.2) can be written as follows by adding the effects of respiratory motion into equation (3.1):

$$\hat{s}(r) = \frac{1}{2} M(r - \Delta r^{R_1} - \Delta r^{R_2}) \sin(\alpha) e^{-\frac{t}{T_1}} e^{-i2\pi(k_e \Delta r^{R_2} + \Delta r^C)} + M_0(r - \Delta r^{R_1} - \Delta r^{R_2}) \sin(\alpha) \left(1 - e^{-\frac{t}{T_1}}\right) e^{-i2\pi(k_e r + \Delta r^{R_2} + \Delta r^C)} \quad (3.2)$$

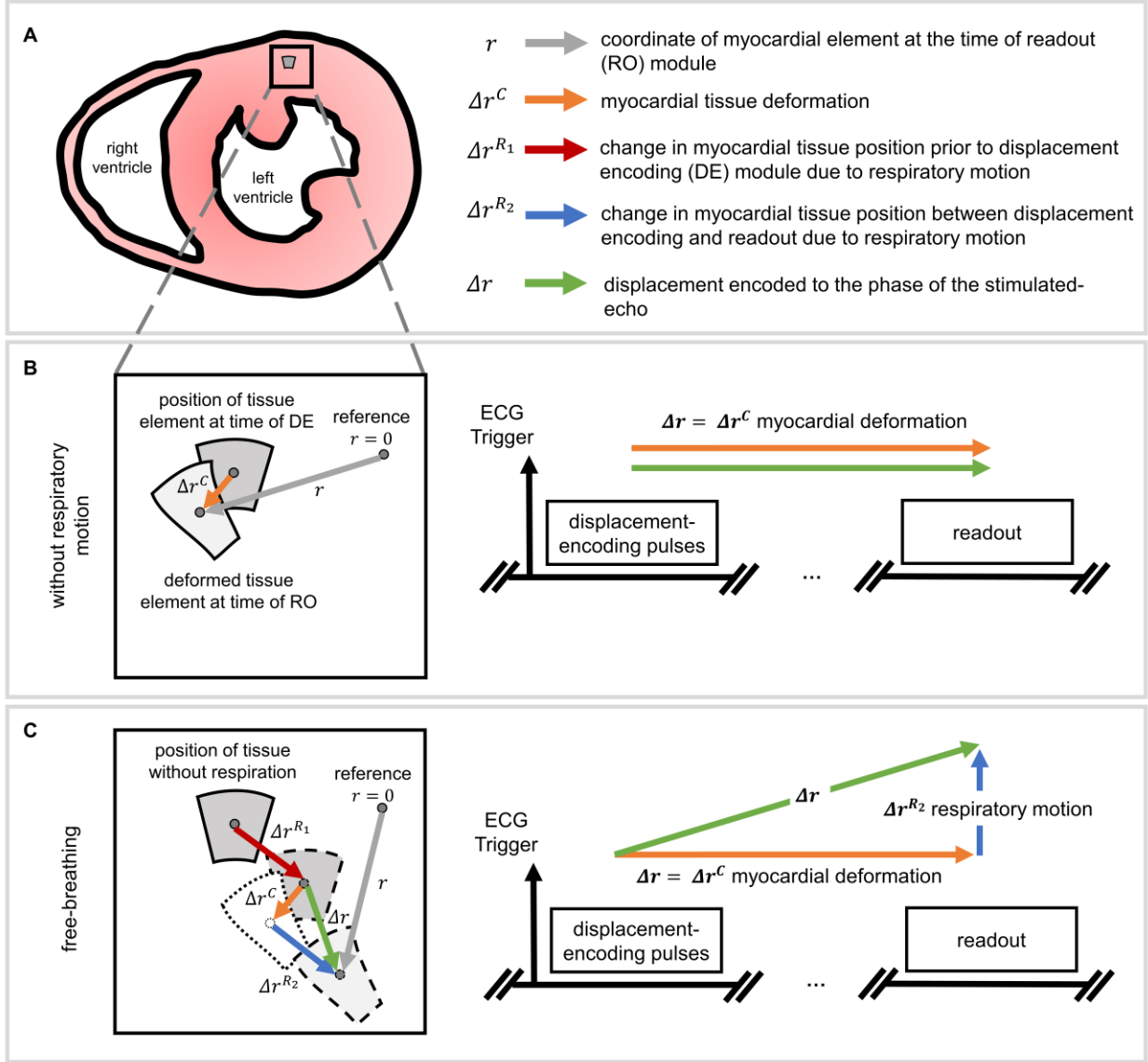


Figure 3.1 - Effect of respiratory motion on the DENSE signal. (A) Schematic diagram showing the left and right ventricles in a short-axis view. (B) In the absence of respiratory motion, cardiac contraction causes displacement of myocardial tissue and this displacement, $\Delta r = \Delta r^C$, is encoded into the phase of the DENSE stimulated-echo. During a free-breathing acquisition (C), the displacement of myocardial tissue is due to both heart deformation and respiratory motion. There are two types of respiratory motion: (1) that which changes the heart's position prior to displacement encoding, Δr^{R_1} , and that which occurs between displacement encoding and readout, Δr^{R_2} . Δr^{R_1} leads

to a position shift of the magnetization amplitude, while Δr^{R_2} gets encoded into the phase of the stimulated echo in addition to leading to a position shift of the magnetization amplitude.

While respiratory motion affects both the stimulated echo and the T_1 echo, the matching method⁸ has previously been shown to effectively perform phase-cycling suppression of the T_1 echo during free breathing, such that here we focus our attention on the effects of respiratory motion on the displacement-encoded stimulated-echo, \hat{s}_{STE} , as shown in equation (3.3).

$$\hat{s}_{STE}(r) = \frac{1}{2}M(r - \Delta r^{R_1} - \Delta r^{R_2}) \sin(\alpha) e^{-\frac{t}{T_1}} e^{-i2\pi(k_e \Delta r^{R_2} + \Delta r^C)} \quad (3.3)$$

Equation (3.3) is expressed in the image domain. Assuming that $m(k)$ represents the Fourier transform of $\hat{s}_{STE}(r)$ when $\Delta r^{R_1} = \Delta r^{R_2} = 0$, then by invoking Fourier Transform properties, equation (3.4) shows that respiratory motion leads to linear and constant phase errors in the k-space domain given by:

$$\hat{m}(k) = m(k) e^{-i2\pi k (\Delta r^{R_1} + \Delta r^{R_2})} e^{-i2\pi (k_e \Delta r^{R_2})} \quad (3.4)$$

where $\hat{m}(k)$ is the k-space representations of the stimulated-echo in the presence of respiratory motion. The previously developed ste-iNAV method has been shown to be effective for correcting the linear phase errors by estimating the in-plane position shifts and applying the corresponding phase correction terms in k-space. However, the remaining constant phase errors due to the respiratory-induced shifts of the stimulated echo phase can still lead to large degrees of signal loss and phase corruption, as shown in Figure 3.2, and need to be corrected. Specifically, as shown in Figure 3.2, when the respiratory-induced shifts of the stimulated echo phase are different for different k-space segments (e.g., when there are different phase shifts of the different spiral interleaves in ECG-gated spiral cine DENSE¹⁵), then signal loss and phase corruption artifacts as shown in Figure 3.2 occur. Mathematically, the stimulated echo affected by per-segment respiratory-induced constant phase shifts is expressed as equation (3.5):

$$\hat{s}_{STE}^c = \sum_{i=1}^N \mathcal{F}^{-1} \left(U_i (E_i^c \mathcal{F}(s_{STE})) \right) \quad (3.5)$$

where s_{STE} is the displacement-encoded stimulated-echo image in the absence of respiratory motion, \mathcal{F} is the 2D Fourier transform, U_i is the sampling operator corresponding to the acquisition of the i^{th} k-space segment, and E_i^c is a complex constant representing the unique respiratory motion-induced constant phase error for the i^{th} k-space segment.

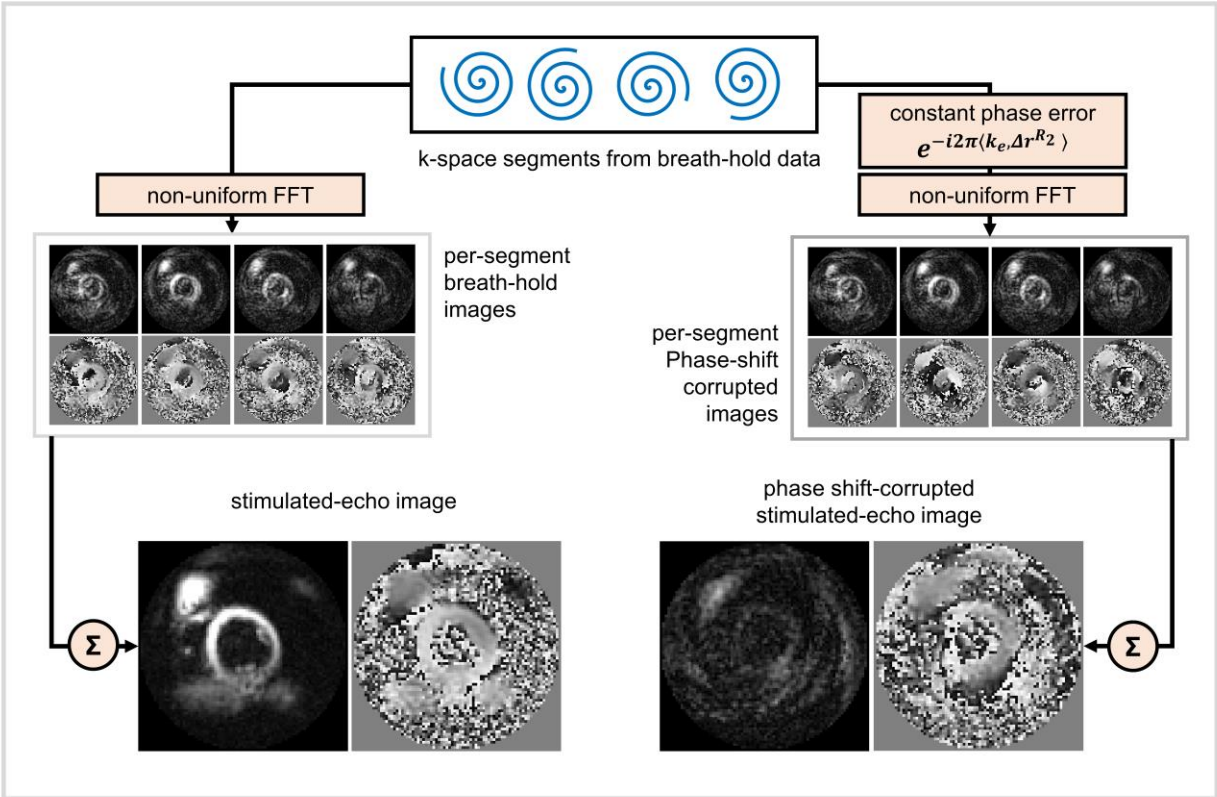


Figure 3.2 - Respiratory motion encoded into the phase of the stimulated-echo in segmented DENSE leads to signal loss and phase corruption artifacts. The respiratory-motion-induced phase shifts were calculated from simulated respiratory motion and applied on breath-hold data on a per-segment basis. The simulated phase shifts lead to signal loss and phase corruptions in segmented DENSE acquisitions.

Because the constant phase errors originate from both in-plane and through-plane motion in DENSE, where it is common to use through-plane gradients to help suppress the T_1 echo⁹, 2D ste-iNAVs are ineffective for estimating these errors. In addition, ste-iNAVs do not provide

sufficient temporal resolution to accurately estimate the phase errors through time. For these reasons, we investigated a deep learning solution to correct for these artifacts.

3.4 Methods

3.4.1 Phantom Experiments

We performed phantom experiments to validate the DENSE motion model provided by equations (3.3), (3.4), and (3.5). The diagram in Figure 3.3.A shows the experimental setup used for the phantom experiment. An agar-gel-filled spherical phantom was used and positioned on a wagon that was moveable inside the bore of the magnet using a slider-crank device. Since motion prior to the application of the displacement-encoding pulses, Δr^{R_1} , causes linear phase errors that can be corrected using ste-iNAVs, we have validated the model for motion that occurs during the time between the application of the initial displacement-encoding pulses and the readout module, Δr^{R_2} . Imaging was performed on a 3T MRI system (Magnetom Prisma, Siemens Healthineers) with an 18-channel phased-array body coil using a spiral cine DENSE sequence¹⁵. DENSE images were acquired from a coronal cross-section of the phantom with diameter $R = 16.4$ mm using the following imaging parameters: field of view (FOV) = 350×350 mm², 4 spiral interleaves per image with 2 interleaves acquired per simulated heartbeat, spiral readout length of 5.6 ms, in-plane spatial resolution of 3.4×3.4 mm², TR = 15 ms, TE = 1.26 ms, slice thickness = 8 mm, and variable flip angle with final $\alpha = 15^\circ$. The displacement encoding frequency was 0.10 cycles/mm, the through-plane dephasing frequency was 0.06 cycles/mm, and the simple encoding method was employed¹⁶. A simulated RR interval of 3000 ms was used. The use of longer than typical RR interval provided sufficient time to move the phantom to the exact designated positions between applications of the displacement-encoding and readout pulses.

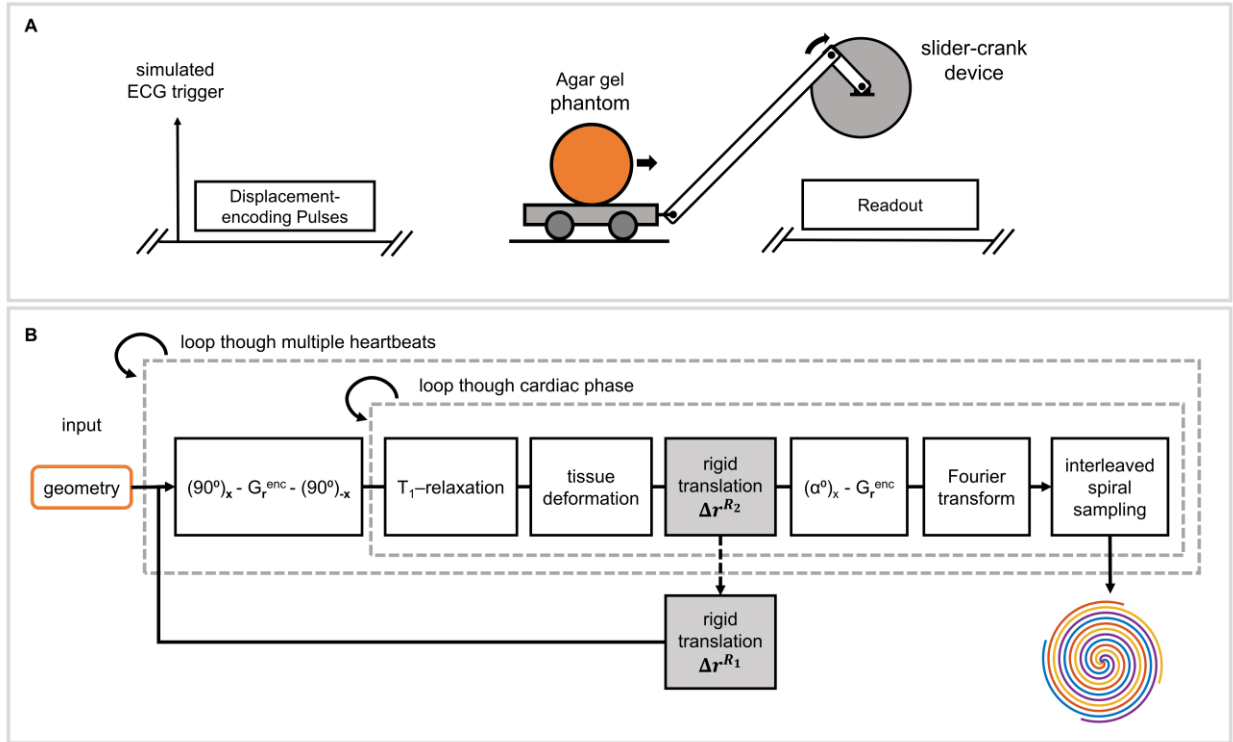


Figure 3.3 - Phantom experiment and Bloch equation simulations used to validate the DENSE motion model that accounts for breathing. Diagrams illustrating A) the phantom experiment used to validate the DENSE motion model where the phantom can be moved in the scanner between the displacement-encoding pulses and the readout, and B) the modules embedded in a Bloch-equation-based DENSE simulator, including the simulation of cardiac motion and the two types of respiratory motion.

Two sets of data were acquired. The first dataset was for reference, where the phantom was kept still during the acquisition. For the second dataset, the phantom was moved using the slider-crank device by $\Delta r^{R_2} = 35$ mm or by $\Delta r^{R_2} = 0$ mm during the time between application of the displacement-encoding pulses and the corresponding readout, as illustrated in Figure 3.4.A. To demonstrate the relationships between the direction of phantom motion and the displacement-encoding direction, a 3-point displacement encoding¹⁶ method was used to acquire three displacement measurements for each set of data. In the first and second measurements, the phantom motion was parallel to or orthogonal to the displacement encoding direction, respectively. The third acquisition, without displacement-encoding gradients, was used to correct for the

nonzero background phase. Phase-cycled datasets at matched phantom locations were also acquired to suppress the T_1 echo.

For image reconstruction, phase-cycling subtraction was performed to suppress the T_1 echo. Next, to simulate stimulated-echo imaging during breathing, stimulated-echo images were reconstructed by selecting two k-space segments from the phantom position with $\Delta r^{R_2} = 0$ and combining them with two segments from the dataset with $\Delta r^{R_2} = 35$ mm. Using the displacement encoding frequency, $k_e = 0.10$ cycle/mm, these parameters induce a π phase shift (0.1 cycle/mm \times 35 mm = 3.5 cycles) corresponding a constant phase error of $e^{i\pi}$ for the second set of k-space segments. The motion-corrupted k-space data were corrected for linear phase errors and constant phase errors using equation (3.4). After motion correction was performed in k-space, images were reconstructed using the nonuniform fast Fourier transform¹⁷.

3.4.2 Bloch-equation DENSE simulations incorporating cardiac and respiratory motion

We also performed simulations to computationally investigate the effects of respiratory motion on DENSE images, where the effects of respiratory motion could be investigated in combination with simulated cardiac deformation (which was not feasible in our non-deforming phantom). Figure 3.3.B shows a diagram of the DENSE Bloch equation simulations incorporating cardiac and respiratory motion¹⁵. The simulator received the geometry of a computational phantom and its corresponding temporal deformation function¹⁸ as input. For each voxel in the phantom, the Bloch equations were solved to compute the magnetization with respect to time, accounting for the application of RF and gradient pulses in the displacement-encoding and readout modules, as well as for the effects of motion and T_1 relaxation. As motion prior to application of the displacement-encoding pulses can be corrected using the ste-iNAV method, we only investigated the effect of motion during the time between application of the displacement-encoding and the

readout pulses. The 2D Fourier transform was applied to the transverse magnetization during the readout to compute its k-space representation. The simulated k-space signal was sampled using interleaved spiral trajectories computed according to the parameters used to acquire data in the phantom experiment.

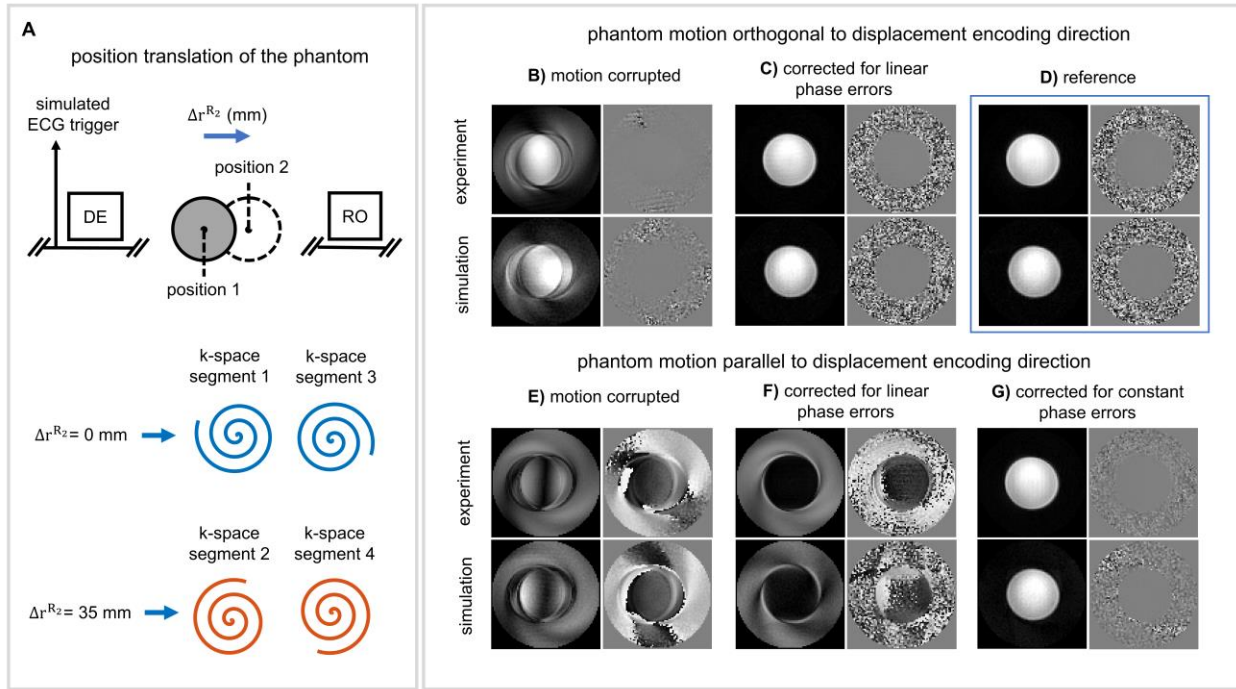


Figure 3.4 - Experimental and simulation results demonstrating that motion in the displacement-encoding direction is encoded into the phase of the stimulated echo and, when the motion is different for different segments, causes signal loss and phase corruption. Phase correction using the signal model of equation (3.4) and the known motion can correct the artifacts. (A) A diagram showing the acquisition of four k-space segments where $\Delta r^{R_2} = 0$ mm for segments one and three and $\Delta r^{R_2} = 35$ mm for segments two and four. (B) DENSE images corresponding to the conditions shown in panel (A) where the object motion is orthogonal and parallel, respectively, to the displacement-encoding direction. Different types of artifacts are observed when motion is orthogonal or parallel to the displacement-encoding direction, and per-segment linear and constant phase corrections applied in k-space can recover artifact-free stimulated-echo images from the motion-corrupted versions.

We used the simulations in two different scenarios. First, we performed simulations of the previously described phantom experiments using a computational non-deforming phantom. The geometry of the phantom was obtained from the data collected during phantom experiment. The T_1 of the phantom was measured as 1.1 seconds. Other simulation parameters included: FOV =

$350 \times 350 \text{ mm}^2$, spiral readout length = 5.6 ms, in-plane spatial resolution = $3.4 \times 3.4 \text{ mm}^2$, and variable flip angle with final $\alpha = 15^\circ$. Simple 3-point displacement encoding¹⁶ and four spiral interleaves per image were used. The actual background phase of the experimental phantom, reflecting the true B0 inhomogeneity, was also used.

Second, we performed simulations that included synthetic cardiac and respiratory motion. For this purpose, we used a computational phantom consisting of two components as shown in Figure 3.5.A: a deforming annulus¹⁹ representing a short-axis image of the heart, and a static component representing other tissue. The concentric circles of the annulus represent the end-diastolic epicardial and endocardial borders. Respiratory motion was simulated by rigid translation of the tissue using a sinusoidal function defined as.

$$r_k^R(n) = a_k \sin\left(\frac{2\pi}{p_k} T_R n + \psi_k\right) \quad (3.6)$$

where a_k , p_k , and ψ_k denote the magnitude, period, and initial phase of the sine wave for the k^{th} heartbeat at the readout time corresponding to sampling of the n^{th} cardiac phase, and T_R denotes the repetition time of the readout module. The rigid translations representing respiratory motion were applied to the phantom between applications of displacement encoding pulses to simulate Δr^{R_1} , and between application of the displacement encoding and readout modules to simulate Δr^{R_2} . We used the following parameters: in-plane translation $a_k = [3, 3]^T \text{ mm}$, $p_k = 14$ times/minutes, and ψ_k was randomly selected from a uniform distribution $u(-\pi, +\pi)$. In addition, simulated reference data were generated using the null respiratory function.

The T_1 of the deforming annulus and the static component were set to 1.1 and 0.7 seconds, respectively, to simulate myocardium and other tissue at 3T. The parameters of the simulation were selected to mimic the following imaging parameters: FOV = $200 \times 200 \text{ mm}^2$, spiral readout length = 5.6 ms, in-plane spatial resolution = $3.4 \times 3.4 \text{ mm}^2$, and variable flip angle with final $\alpha =$

15°. Balanced 3-point displacement encoding¹⁶ was used for 2D in-plane displacement measurements, and four spiral interleaves per image with two interleaves acquired per cardiac cycle were used. The simulated cardiac cycle had a duration of 0.8 seconds, and these parameters provided a temporal resolution of 30 ms per cardiac phase. Phase-cycled acquisitions were also simulated, and matchmaking suppression of the T_1 echo was simulated by using matched respiratory positions for the phase-cycling pairs. The displacement-encoding frequency was set to 0.06 cycles/mm.

The simulated motion-corrupted data were corrected for linear and constant phase errors (following equations (3.4) and (3.5)) using the known motion and the resulting k-space data were reconstructed using the nonuniform fast Fourier transform¹⁷. The motion-corrupted and motion-compensated images were compared to reference images without motion.

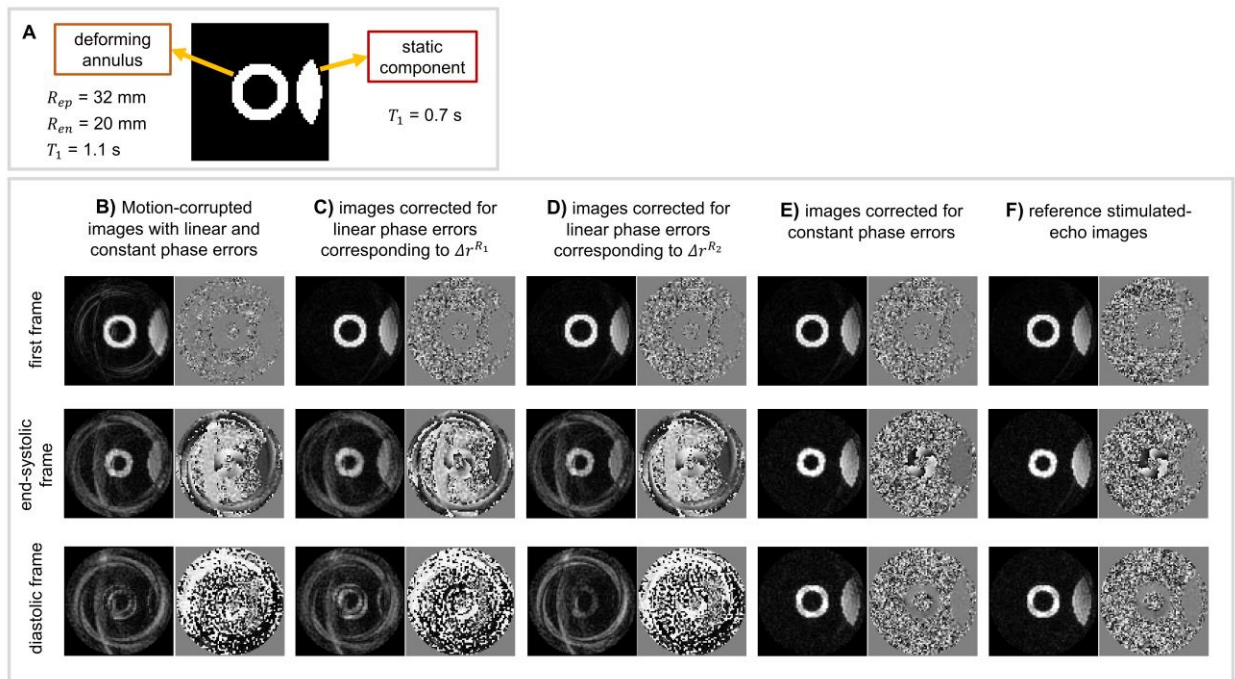


Figure 3.5 - Bloch equation simulations using a deforming heart motion phantom demonstrate respiratory-motion induced DENSE artifacts and their correction using the DENSE motion model of Equations (3.3), (3.4), and (3.5). (A) The computational deforming phantom consists of a deforming annulus where the concentric circles define the

epicardial and endocardial borders in the heart short-axis view and a static component. (B-F) The motion corrupted DENSE images were simulated using the Bloch equations with typical DENSE sequence parameters and the incorporation of motion. Motion correction based on the known motion and the linear (corresponding to Δr^{R_1} and Δr^{R_2}) and constant corrections (corresponding to Δr^{R_2}) of Equations (3.4) and (3.5) recover images that are nearly identical to the reference images and preserve the phase-based measurement of heart contraction.

3.4.3 Acquisition of training data for the convolutional neural network

To provide training data to develop a deep learning model, we acquired breath-hold DENSE images from twenty-three healthy volunteers (age = 28.7 ± 4.7 , 52% female) using a 3T MRI system. All CMR was performed in accordance with a protocol approved by the Institutional Review Board for Human Subjects Research at our institution and informed consent was obtained from all subjects prior to imaging. A spiral cine DENSE sequence¹⁵ with prospective cardiac gating was used for breath-hold scans with the following parameters: FOV = 200×200 mm² (with outer volume suppression), spiral readout length = 5.6 ms, in-plane spatial resolution = 3.4×3.4 mm², TR = 15 ms, TE = 1.26 ms, slice thickness = 8 mm, and variable flip angle with final $\alpha = 15^\circ$. Four spiral interleaves per image with two interleaves acquired per heartbeat provided a temporal resolution of 30 ms. Phase-cycling was used to suppress the T₁-echo. The displacement encoding frequency and the through-plane dephasing frequency were set to 0.06 cycles/mm and 0.08 cycles/mm, respectively. Short-axis images at basal, mid-ventricular, and apical levels were acquired for each subject. For each slice, balanced three-point displacement encoding was used to measure 2D in-plane displacements and perform correction for background phase. The spiral multicoil cine DENSE data were reconstructed using the nonuniform fast Fourier transform¹⁷ and adaptive coil combination²⁰.

3.4.4 Architecture of the deep learning model

We used an instance of a U-Net²¹ with recurrent convolutional modules as the deep learning model. The convolutional modules in the generic U-Net were replaced with convolutional long short-term memory (LSTM)^{22,23} cells to exploit the time correlations of the cine DENSE data. The output of each LSTM was normalized using instance normalization²⁴ and activated using leaky rectified linear units. The network receives a time-series of images and processes one frame at a time while incorporating the accumulated features from the previous frame. Specifically, the hidden and the cell states of each LSTM are computed by processing the current input frame which is used as input for the processing of the next frame. In addition, the skip connections pass the current hidden states of the convolutional LSTM cells.

3.4.5 Training of the constant-phase correction deep learning model (DENSE-RESP-NET)

We postulated that the artifacts due to the respiratory-motion-induced constant phase error could be corrected using a deep learning model. Referring to Figure 3.6, to train the model, phase error-corrupted DENSE images, \hat{S}_{STE}^c , were generated using equation (3.5) and the following steps: (a) respiratory motions were simulated using the sine wave defined in equation (3.6), (b) the corresponding phase errors were computed using the simulated motion, $E_i^c = e^{i2\pi k_e \Delta r_i^{R2}}$ where i denotes the i^{th} k-space segment, and (c) the phase error terms were applied to the breath-hold DENSE data according to equation (3.5). The respiratory-induced translations, Δr_i^{R2} , were calculated using $\Delta r_i^{R2} = r_i^R(n) - r_i^R(1)$, where $r_i^R(n)$ denotes the position of the heart when the n^{th} frame is acquired and $r_i^R(1)$ denotes the position of the heart at the beginning of the corresponding heartbeat.

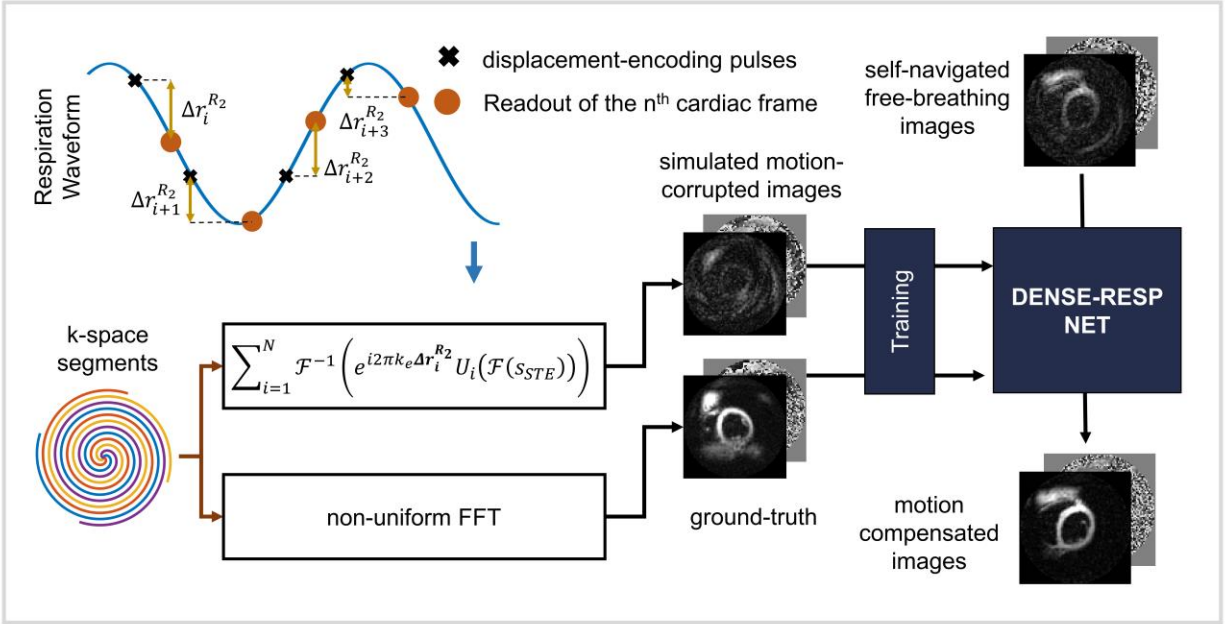


Figure 3.6 - Diagram illustrating the generation of phase-shift-corrupted DENSE images for training a convolutional neural network, DENSE-RESP-NET, to correct the signal loss and phase corruption artifacts in self-navigated free-breathing cine DENSE. Respiratory motion was simulated using sine waves with magnitude and frequency similar to physiological values. The constant phase errors were calculated and applied on per-segment breath-hold DENSE images. The motion-corrupted images were generated by summing the manipulated per-segment images according to equation (3.6). The motion-corrupted and the corresponding breath-hold images were used to train an instance of U-Net with recurrent connections and long-short term memory cells.

The resulting motion-corrupted and the corresponding uncorrupted breath-hold images were used to train the model serving as input and ground-truth, respectively. A diagram of the training is shown in Figure 3.6. The breath-hold data from twenty-three healthy volunteers with three slices per subject and three displacement measurements (x-, y-, and background) per slice provided 207 multiphase DENSE slices (time-series) for training. To accommodate for unseen geometries, spatial translations and rotations in addition to image flipping were used to augment the training set which provided 828 time-series after data augmentation. For each time-series, the amplitude and the period of the sine wave were randomly selected from uniform distributions $u(0, 25)$ mm and $u(10, 20)$ times/minute, respectively. Thirty and six combinations of sine wave

amplitude and frequency, respectively, were simulated per time-series resulting in 24840 and 4968 pairs of time-series for training and validating the model, respectively. The real and imaginary parts of images were separated and formatted as two-channel data. Training was performed on a Nvidia Tesla V100 GPU core for 72 hours. The trained model is referred to as DENSE-RESP-NET.

3.4.6 Testing of the methods using prospectively acquired free-breathing DENSE

To test the trained model, we acquired free-breathing cine DENSE from nine healthy volunteers (age = 25.9 ± 3.7 , 44% female). These healthy subjects were different than those recruited for acquisition of the training data. Free-breathing data were acquired using a modified spiral DENSE sequence⁸ with uniform rotation of the spiral interleaves through time to enable construction of the ste-iNAV^{8,25}. To facilitate T₁-echo suppression using match-making, the acquisition of each interleaf was repeated 4 times using an average loop, resulting in a 50-heartbeat imaging protocol while keeping all other parameters the same as those used for breath-hold data. Short-axis free-breathing images at basal, mid-ventricular, and apical levels were acquired per subject. Breath-hold images at matched slice positions were acquired to serve as reference for comparisons. For each slice, 18-30 frames were acquired depending on the subject's heart rate.

For each time frame, phase-cycled spiral interleaves at matched respiratory position were identified using the match-making algorithm⁸ and subtracted to suppress the T₁-echo. To correct for inter-segment in-plane position shifts and corresponding linear phase errors, ste-iNAV⁸ were generated using consecutively acquired interleaves. In the current design, each ste-iNAV consisted of 4 consecutively acquired interleaves with uniform rotation of spiral interleaves through time. For each heartbeat, multiple ste-iNAV⁸ were reconstructed. The inter-heartbeat in-plane translations were automatically estimated using 2D cross-correlation²⁶ and linear phase corrections

were applied using the estimated translations on a per-segment basis in k-space. The resulting spiral multicoil cine DENSE data were reconstructed as described previously. These images are referred to as self-navigated free-breathing images.

3.4.7 Evaluation of the deep learning model

The trained motion compensation model, DENSE-RESP-NET, was evaluated on volunteer data by comparing self-navigated free-breathing images processed by DENSE-RESP-NET to unprocessed self-navigated free-breathing images, free-breathing data with multiple averages without any type of self-navigation or phase correction, and to breath-hold data which served as the reference standard.

Because DENSE measures tissue displacement using the signal phase, we used phase SNR as one metric of image quality. Since the phase error due to breathing accumulates over time and the diastolic frames are more affected by the corresponding artifacts, the phase SNR was computed on three mid-diastolic frames. The calculation of phase SNR is described as follows^{4,11}:

$$phase\ SNR = \left\| \frac{mean(\text{phase of mid} - \text{diastolic ROI})}{stdev(\text{phase of end} - \text{diastolic ROI})} \right\| \quad (3.7)$$

where the standard deviation of the phase of the end-diastolic myocardial ROI provides a measure of the standard deviation of phase at a cardiac frame where the mean phase is essentially zero. The measured phase SNR values were used to compare the images using one-way analysis of variance and a post hoc Tukey's test.

In addition, the DENSE-RESP-NET processed, self-navigated free-breathing, and breath-hold images were analyzed for strain using established methods²⁷⁻²⁹. The averaged free-breathing images did not undergo strain analysis because the image quality was so poor that the semi-automated myocardial segmentation procedure generally failed for these datasets. Since end-

systolic circumferential strain is the most commonly reported metric for cardiac strain MRI, we performed Bland-Altman analysis for this parameter. In addition, we analyzed the early diastolic circumferential strain rate since the constant phase error has a greater impact on diastolic frames.

3.5 Results

3.5.1 Validation of the DENSE signal model that accounts for the effects of respiratory motion using a moving, non-deformable phantom

Motion-corrupted DENSE magnitude and phase images from experimental and simulation studies are shown in Figure 3.4.B-G for the cases where the moving, non-deforming phantom motion was parallel (panels E-G) to or orthogonal (panels B and C) to the displacement-encoding direction. When motion is orthogonal to the displacement-encoding direction, only linear phase errors and blurring/ghosting artifacts occur, and the artifacts are eliminated by correcting the per-segment linear phase errors. When the motion is parallel to the displacement-encoding direction, the motion is encoded into the phase of the stimulated-echo and causes constant phase errors in k-space in addition to the linear phase errors. Motion-corrupted images corrected for just the known linear phase errors are shown in Figure 3.4.F, and the remaining artifacts in the images are due to the constant phase errors. The images corrected for the remaining constant phase errors, using equation (3.4), are shown in Figure 3.4.G.

3.5.2 Simulated respiratory motion-induced artifacts in DENSE images of a deforming digital phantom and their correction using the proposed model

Figure 3.5.B-F shows DENSE magnitude and phase images from the deforming computational digital phantom generated using Bloch equation simulations. Simulated motion-corrupted images are shown at the initial, end-systolic, and mid-diastolic phases of the cardiac

cycle. Using Eqs. 4-5, linear phase corrections corresponding to Δr^{R_1} and Δr^{R_2} and constant phase corrections were applied to the simulated motion-corrupted data and the resulting images are shown in panels C, D, and E of the figure. The reference images are shown in panel F. The simulated respiratory motion led to signal loss in the magnitude images and phase corruption in the phase images. However, using the known respiratory motion and the per-segment linear and constant phase corrections according to equations (3.4) and (3.5), the displacement-encoded stimulated-echo images are recovered from their respiratory motion-corrupted versions, and the effects of cardiac motion on the image phase are preserved.

3.5.3 The deep learning model can correct the respiratory motion-induced artifacts in self-navigated free-breathing DENSE

Example magnitude and phase images from self-navigated free-breathing DENSE processed with DENSE-RESP-NET are shown in Figure 3.7 for an end-systolic (I, J) and a diastolic frame (K, L), and for comparison the same images are shown for averaged free-breathing (A-D), self-navigated free-breathing without DENSE-RESP-NET (E-H), and breath-hold DENSE (M-P). Signal loss in the magnitude images (G) and phase corruption in the phase images (H) of the self-navigated free-breathing data due to respiratory motion are readily apparent in the diastolic images where breathing has a larger effect. The deep learning model restored the signal loss and corrected the phase values in the DENSE-RESP-NET processed magnitude (K) and phase (L) images, respectively.

The bar plot in Figure 3.8 summarizes the comparisons of the phase SNR. The phase SNR assessed for DENSE-RESP-NET processed images was significantly higher compared to the self-navigated and averaged free-breathing images and was comparable to those of breath-hold images.

In addition, the self-navigated free-breathing images had significantly higher phase SNR than the averaged free-breathing data.

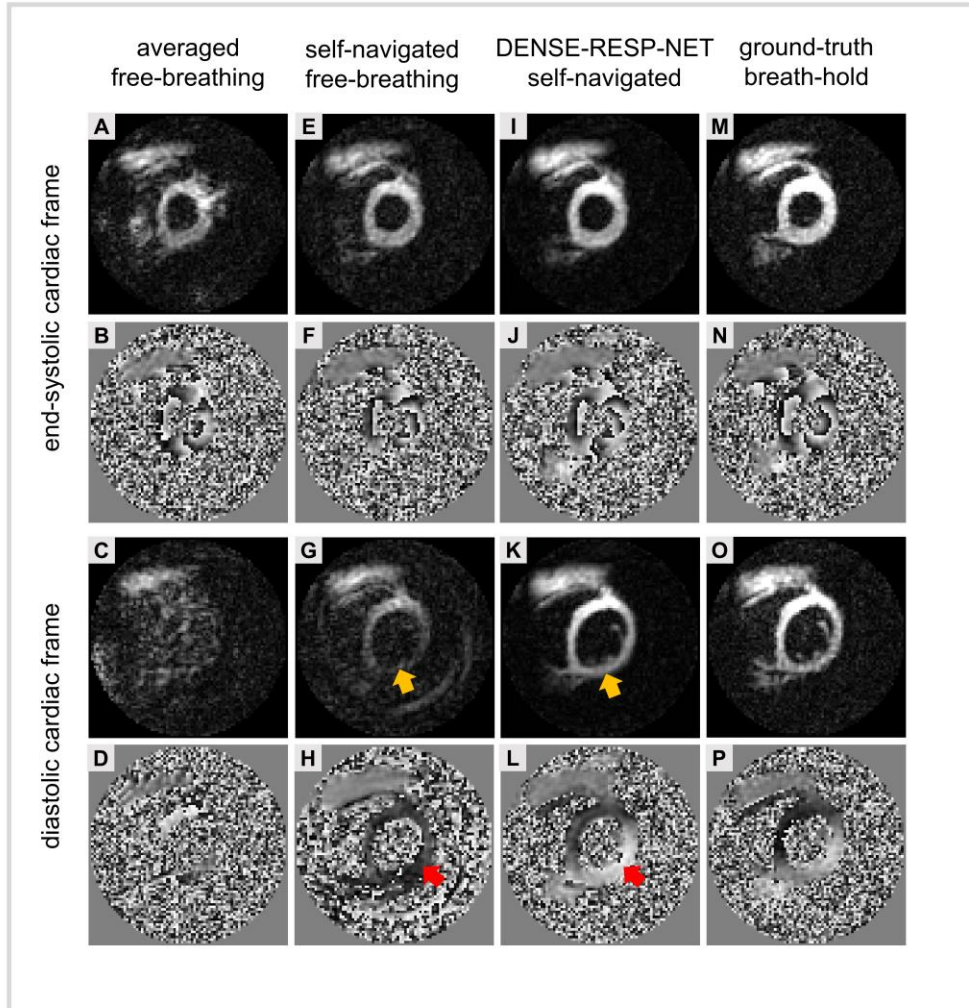


Figure 3.7 - *DENSE-RESP-NET* compensates for the signal loss and phase corruption in self-navigated free-breathing cine DENSE. Example magnitude and phase images of averaged free-breathing, self-navigated free-breathing, *DENSE-RESP-NET* processed and ground-truth breath-hold cine DENSE images are shown for an end-systolic frame and a diastolic frame. *DENSE-RESP-NET* effectively corrects the signal loss and phase corruption, and the results are more pronounced in the diastolic frame where Δr^{R_2} is greater.

Figure 3.9 shows segmental circumferential strain-time curves and global circumferential strain rate-time curves for the breath-hold, the *DENSE-RESP-NET* processed, the self-navigated free-breathing, and the averaged free-breathing images computed from the example images shown

in Figure 3.7. Overall, the DENSE-RESP-NET processed curves are in close agreement with breath-hold curves for both segmental strain and the global strain rate. The segmental strain and the global strain rate curves from the self-navigated free-breathing images are in close agreement with those of the reference and the DENSE-RESP-NET processed images early in the cardiac cycle. However, the agreement worsens in diastole. The segmental strain and the global strain rate curves from the averaged free-breathing images were unreliable compared to those of reference images.

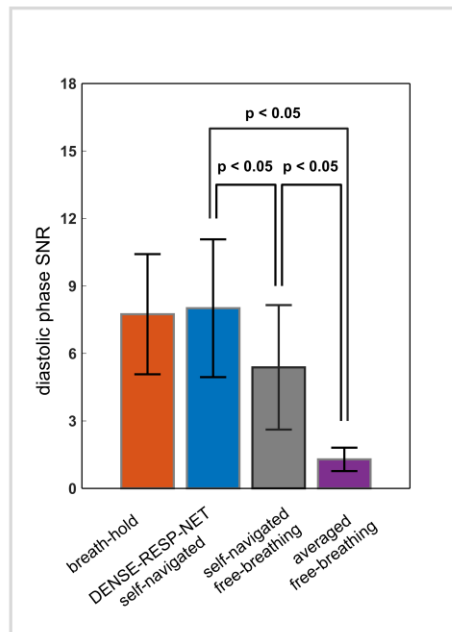


Figure 3.8 - Diastolic phase SNR demonstrates improved image quality in DENSE-RESP-NET corrected self-navigated images compare to uncorrected self-navigated and averaged free-breathing images. Breath-hold DENSE images represent the reference standard. Bar plots and error bars show the mean and standard deviation of the phase SNR calculated according to equation (3.7). The phase SNR values were 8.75 ± 2.67 , 9.07 ± 3.06 , 6.38 ± 2.77 , and 1.29 ± 0.52 (p -value < 0.001) for the breath-hold, the DENSE-RESP-NET self-navigated, the self-navigated free-breathing (without DENSE-RESP-NET), and the averaged free-breathing images respectively.

Figure 3.10 summarizes the Bland-Altman analysis for the segmental end-systolic circumferential strain and the global early diastolic circumferential strain rate for the twenty-seven DENSE slices acquired from the nine healthy volunteers. The end-systolic segmental strain shows

modestly better agreement for DENSE-RESP-NET compared to unprocessed self-navigated free-breathing images with respect to the breath-hold images. For early diastolic strain rate, agreement and accuracy are substantially improved in favor of the DENSE-RESP-NET processed images compared to the self-navigated free-breathing images.

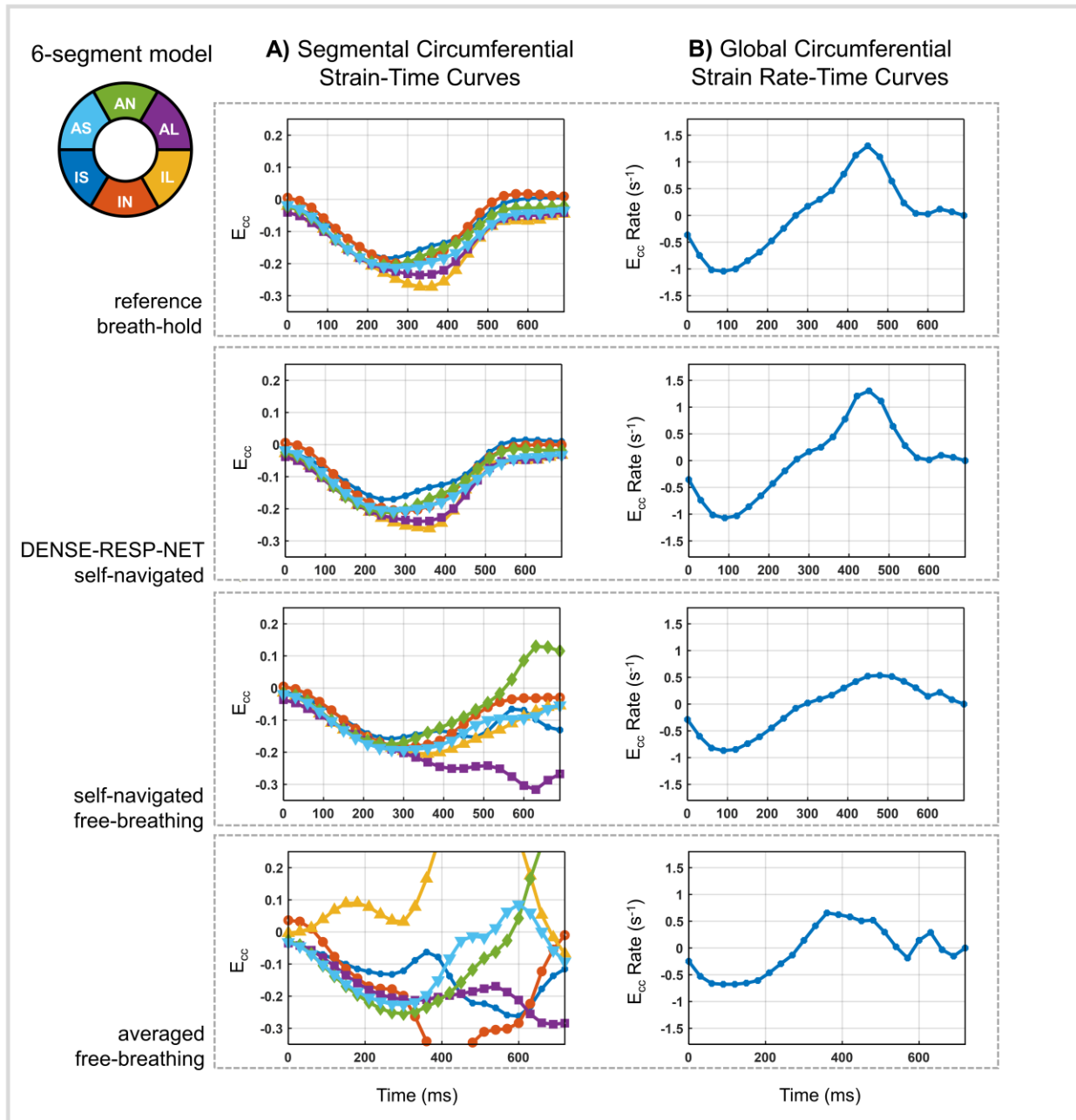


Figure 3.9 - Strain measurement in a healthy subject shows good agreement between the DENSE-RESP-NET corrected data compared to the breath-hold data, whereas the self-navigated and averaged free-breathing data are

unreliable in diastole. A) Segmental circumferential strain (E_{cc})-time curves, and B) global circumferential strain rate-time curves of the example in Figure 3.7 are shown for averaged free-breathing, self-navigated free-breathing, DENSE-RESP-NET processed and ground-truth breath-hold images.

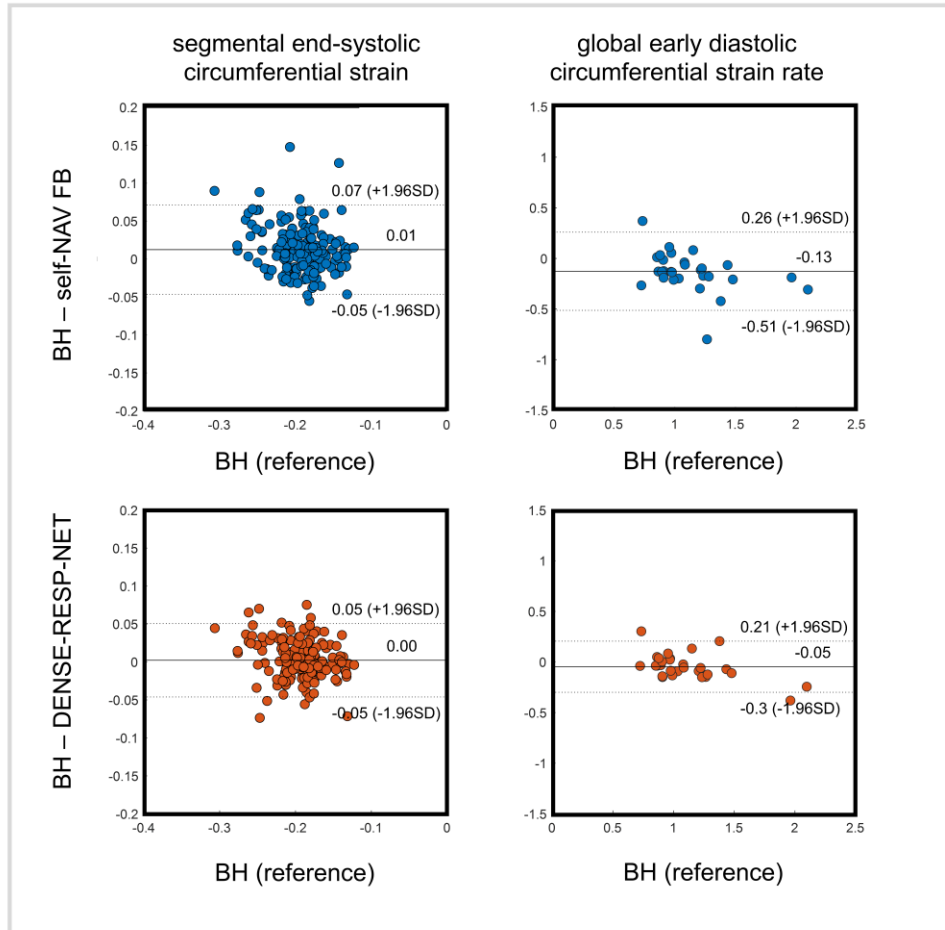


Figure 3.10 - Bland-Altman analysis of segmental circumferential strain and global circumferential strain rate of the DENSE-RESP-NET corrected data shows improved accuracy and a better agreement with the breath-hold (BH) DENSE data compared to uncorrected self-navigated free-breathing data (self-NAV FB).

3.6 Discussion

The main contributions of this study are that (a) a new model was introduced and validated that describes the effects of breathing on the magnitude and phase of the DENSE signal, and (b) the new motion model was used to train a deep convolutional neural network, DENSE-RESP-NET, to correct the constant phase artifacts in free-breathing cine DENSE attributed to the

encoding of respiratory motion into the phase of the stimulated echo. When used in concert with the match-making method for suppression of the T_1 echo and ste-iNAV's for correction of linear phase errors in k-space related to object motion, DENSE-RESP-NET-corrected self-navigated free-breathing DENSE images show good agreement with breath-hold DENSE images and the corresponding strain data show good agreement with breath-hold strain data for the evaluation of both systolic and diastolic parameters.

Our phantom experiments and Bloch equation simulations using non-deforming and deforming computational phantoms were used to validate the DENSE motion model of equations (3.3), (3.4), and (3.5). For the phantom experiments, DENSE images were formed by combining spiral interleaves acquired when the phantom was in different positions at the time of data readout. For the simulations, the Bloch equations were solved to generate the raw data. In both cases, the object motion was known, and our results in Figure 3.4 and Figure 3.5 showed that correcting the phase of the k-space data according to equations (3.3), (3.4), and (3.5) successfully removed the signal loss and phase corruption artifacts from the images. Together, these results demonstrate the validity of equations (3.3), (3.4), and (3.5) for describing the effects of motion on segmented stimulated-echo images.

The present study used the new DENSE motion model, represented by equations (3.3), (3.4), and (3.5), in combination with breath-hold DENSE k-space data to generate synthetic data that was used to train DENSE-RESP-NET. An alternative approach could be to use breath-hold DENSE images and free-breathing DENSE images acquired at matched locations; however, that approach is very challenging and unlikely to be successful because matching locations between breath-hold and free-breathing acquisitions is imperfect. Unsupervised and semi-supervised learning approaches could be used when the training pairs are at different locations or when only

a few pairs at matched locations are available, respectively. However, hundreds or thousands of datasets would be needed to represent sufficient variability in respiration. To our knowledge, other than using synthetic data as presented in this study, there is no other time- and cost-efficient way to obtain training data for this task. Therefore, for this task it was essential to understand the physics underlying the artifacts, as a description of the underlying physics was needed to generate training data and facilitate a deep learning solution.

The recurrent neural connections in DENSE-RESP-NET using the LSTM cells provided two main advantages. First, it exploits the time correlations of the cine DENSE data by accumulating the spatial features through time. This is important for correction of the artifacts caused by constant phase error as they temporally grow in magnitude. Second, DENSE-RESP-NET is able to process the cine DENSE images independent of the number of acquired cardiac frames, which facilitates its application in in vivo imaging where heart rates vary.

A limitation of the current approach was that the in vivo images used for training and evaluation of the model did not include data from heart disease patients. Although the developed deep learning model was effective, in the future a more generalized model may require data from heart disease patients. Another limitation was that long-axis images were not included in the training and testing data. Finally, the in vivo data used in this study were acquired with a specific set of acquisition parameters. While we showed good performance of free-breathing cine DENSE with match-making, ste-iNAVs and DENSE-RESP-NET using a specific protocol, a generalized deployment of the deep learning model on self-navigated free-breathing images with different acquisition parameters and various types of heart disease may require re-training of the model. Future studies may evaluate the current model in heart disease patients and evaluate its generalizability.

3.7 Conclusion

A new model was introduced to describe the effects of breathing on the magnitude and phase of the DENSE signal, and it was used to train DENSE-RESP-NET to correct for breathing-associated constant phase errors. When used in combination with the match-making method for suppression of the T_1 echo and ste-iNAVs for correction of linear phase errors, DENSE-RESP-NET-corrected self-navigated free-breathing DENSE images and myocardial strain data show good agreement with breath-hold DENSE.

3.8 References

1. Kim D, Gilson WD, Kramer CM, Epstein FH. Myocardial tissue tracking with two-dimensional cine displacement-encoded MR imaging: development and initial evaluation. *Radiology*. 2004;230(3):862-871.
2. Lin K, Meng L, Collins JD, Chowdhary V, Markl M, Carr JC. Reproducibility of cine displacement encoding with stimulated echoes (DENSE) in human subjects. *Magn Reson Imaging*. 2017;35:148-153. doi:10.1016/j.mri.2016.08.009
3. Auger DA, Ghadimi S, Cai X, et al. Reproducibility of global and segmental myocardial strain using cine DENSE at 3 Tesla: A multicenter study in healthy subjects and heart disease patients. *J Card Magn Reson*. 2022.
4. Ghadimi S, Auger DA, Feng X, Sun C, Meyer CH, Bilchick KC, Cao JJ, Scott, AD, Oshinski JN, Ennis DB EF. Fully-automated global and segmental strain analysis of DENSE cardiovascular magnetic resonance using deep learning for segmentation and phase unwrapping. *J Cardiovasc Magn Reson*. 2021.
5. Bilchick KC, Auger DA, Abdishektaei M, et al. CMR DENSE and the Seattle Heart Failure

- Model Inform Survival and Arrhythmia Risk After CRT. *JACC Cardiovasc Imaging*. 2020;13(4):924-936. doi:10.1016/j.jcmg.2019.10.017
6. Mangion K, Carrick D, Carberry J, et al. Circumferential Strain Predicts Major Adverse Cardiovascular Events Following an Acute ST-Segment–Elevation Myocardial Infarction. *Radiology*. 2019;290(2):329-337. doi:10.1148/radiol.2018181253
 7. Jing L, Binkley CM, Suever JD, et al. Cardiac remodeling and dysfunction in childhood obesity: a cardiovascular magnetic resonance study. *J Cardiovasc Magn Reson*. 2016;18(1):28.
 8. Cai X, Epstein FH. Free-breathing cine DENSE MRI using phase cycling with matchmaking and stimulated-echo image-based navigators. *Magn Reson Med*. 2018;80(5):1907-1921.
 9. Zhong X, Spottiswoode BS, Cowart EA, Gilson WD, Epstein FH. Selective suppression of artifact-generating echoes in cine DENSE using through-plane dephasing. *Magn Reson Med An Off J Int Soc Magn Reson Med*. 2006;56(5):1126-1131.
 10. Aletras AH, Ding S, Balaban RS, Wen H. DENSE: displacement encoding with stimulated echoes in cardiac functional MRI. *J Magn Reson (San Diego, Calif 1997)*. 1999;137(1):247.
 11. Abdi M, Feng X, Sun C, Bilchick KC, Meyer CH, Epstein FH. Suppression of artifact-generating echoes in cine DENSE using deep learning. *Magn Reson Med*. 2021;86(4):2095-2104. doi:10.1002/MRM.28832
 12. Epstein FH, Gilson WD. Displacement-encoded cardiac MRI using cosine and sine modulation to eliminate (CANSEL) artifact-generating echoes. *Magn Reson Med*. 2004;52(4):774-781. doi:10.1002/mrm.20232
 13. Tsao J, Laurent D. N-SPAMM for efficient displacement-encoded acquisition in myocardial

- tagging. *Proc 13th Annu Meet ISMRM, Miami Beach, Florida, USA*. 2005;42(6):273.
14. Batchelor PG, Atkinson D, Irarrazaval P, Hill DLG, Hajnal J, Larkman D. Matrix description of general motion correction applied to multishot images. *Magn Reson Med An Off J Int Soc Magn Reson Med*. 2005;54(5):1273-1280.
 15. Zhong X, Spottiswoode BS, Meyer CH, Kramer CM, Epstein FH. Imaging three-dimensional myocardial mechanics using navigator-gated volumetric spiral cine DENSE MRI. *Magn Reson Med*. 2010;64(4):1089-1097.
 16. Zhong X, Helm PA, Epstein FH. Balanced Multipoint Displacement Encoding for DENSE. 2009;988:981-988. doi:10.1002/mrm.21851
 17. Fessler JA. On NUFFT-based gridding for non-Cartesian MRI. *J Magn Reson*. 2007;188(2):191-195.
 18. Gilliam AD, Zhong X, Epstein FH. Automated cardiac motion estimation from 3D Cine DENSE MRI. *J Cardiovasc Magn Reson*. 2012;14(S1). doi:10.1186/1532-429X-14-S1-W16
 19. Gilliam AD, Epstein FH. Automated Motion Estimation for 2-D Cine DENSE MRI. *IEEE Trans Med Imaging*. 2012;31(9):1669-1681. doi:10.1109/TMI.2012.2195194
 20. Walsh DO, Gmitro AF, Marcellin MW. Adaptive reconstruction of phased array MR imagery. *Magn Reson Med An Off J Int Soc Magn Reson Med*. 2000;43(5):682-690.
 21. Ronneberger O, Fischer P, Brox T. U-net: Convolutional networks for biomedical image segmentation. In: *International Conference on Medical Image Computing and Computer-Assisted Intervention*. ; 2015:234-241.
 22. Hochreiter S, computation JS-N, 1997 undefined. Long short-term memory. *ieeexplore.ieee.org*. <https://ieeexplore.ieee.org/abstract/document/6795963/>. Accessed

March 31, 2022.

23. Xingjian SHI, Chen Z, Wang H, Yeung D-Y, Wong W-K, Woo W. Convolutional LSTM network: A machine learning approach for precipitation nowcasting. In: *Advances in Neural Information Processing Systems*. ; 2015:802-810.
24. Ulyanov D, Vedaldi A, Lempitsky V. Instance Normalization: The Missing Ingredient for Fast Stylization. July 2016. <http://arxiv.org/abs/1607.08022>. Accessed March 31, 2022.
25. Cai X, Epstein FH. Free-breathing cine DENSE imaging. 2018. <https://patents.google.com/patent/US10830855B2/en>.
26. Cai X, Epstein F, X Zhong - US Patent 10 310,047, 2019 undefined. Systems and methods for free-breathing cine DENSE MRI using self-navigation. *Google Patents*. 2017;568(62). <https://patents.google.com/patent/US10310047B2/en>. Accessed March 31, 2022.
27. Spottiswoode BS, Zhong X, Lorenz CH, Mayosi BM, Meintjes EM, Epstein FH. Motion-guided segmentation for cine DENSE MRI. *Med Image Anal*. 2009;13(1):105-115.
28. Spottiswoode BS, Zhong X, Hess AT, et al. Tracking myocardial motion from cine DENSE images using spatiotemporal phase unwrapping and temporal fitting. *IEEE Trans Med Imaging*. 2006;26(1):15-30.
29. Gilliam A, Suever J. 2D Cine DENSE Post-Processing Software. <https://github.com/denseanalysis/denseanalysis>. Published 2016.

Chapter 4 : Compensation for respiratory-induced stimulated-echo artifacts in free-breathing adaptive-matchmaker DENSE applied in healthy subjects and heart failure patients

4.1 Abstract

Motion compensated DENSE imaging requires methods to correct all three types of artifacts in free-breathing DENSE MRI. The adaptive match-making method and in-plane motion estimation and correction using the ste-iNAVs were previously developed and shown to be effective to suppress the first two types of artifacts. The developed deep learning model (DENSE-RESP-NET) for compensation of signal loss and phase corruption due to respiratory-motion-induced phase errors has shown to be an effective on free-breathing self-navigated DENSE. While DENSE-RESP-NET was evaluated on free-breathing images acquired with multiple acquisitions, the previously developed adaptive free-breathing method provides a more efficient way of suppressing the T_1 -echo. The DENSE-RESP-NET method in conjunction with the adaptive free-breathing and the ste-iNAV methods will potentially compensate for all types of respiratory motion artifacts in free-breathing DENSE MRI. In this study, DENSE-RESP-NET is evaluated on adaptive free-breathing cine DENSE image from healthy human subjects and heart failure patients.

4.2 Introduction

Displacement-encoding with stimulated-echo (DENSE) is an accurate and reproducible method of myocardial strain imaging and with automatic post-processing¹⁻³.

Cine DENSE data is typically collected using breath-hold protocols which leads to patient discomfort and limitations with pediatric subjects and those under anesthesia⁴. Conventional methods such as diaphragm navigator-gated acquisitions enables free-breathing cine DENSE imaging by continuously collecting cine DENSE data while allowing the subject to breath during acquisitions⁵. A navigator-echo is acquired at the end of each cardiac cycle to track the position of the diaphragm. After data acquisition, only data falls into the end-expiration phase of the respiratory cycle is used for image reconstruction. The limitations of diaphragm navigator-gated method are low acquisition efficiency, complexities with the navigator setup, requirements for additional scout imaging, and variably in image quality^{4,6}.

Motion compensation in free-breathing DENSE requires effective suppression of the three types of artifacts that arise in free-breathing DENSE. In Chapter 3, we evaluated the offline reconstruction match-making algorithm for suppression of the T_1 -echo in self-navigated free-breathing acquisitions. To increase the likelihood of finding phase-cycling pairs at the matched respiratory positions, acquisition of each k-space segment was repeated multiple time using an averaging loop. DENSE-RESP-NET has shown to be effective for compensation of signal loss and phase corruption using this approach.

Repeated acquisition of each k-space segment reduces the imaging efficiency and may not guarantee effective suppression of the T_1 -echo as the number of required repetitions may vary from subject to subject. Previously, an adaptive match-making acquisition method was developed that addresses these limitations by prospectively identifying the matched phase-cycling pairs using online feedback during free-breathing acquisitions⁷. I hypothesized that the adaptive free-breathing acquisitions used in concert with self-navigation and the developed DENSE-RESP-NET can

ensure suppression of the free-breathing artifacts in DENSE in healthy human subjects and heart disease patients.

The purpose of this study is to evaluate the DENSE-RESP-NET in self-navigated adaptive free-breathing DENSE imaging applied on healthy human subjects and heart-failure patients.

4.3 Methods

4.3.1 *Prospective in vivo cine DENSE imaging*

To evaluate the DENSE-RESP-NET on adaptive free-breathing images, cine DENSE acquisitions were performed on nine healthy volunteers (age = 25.9 ± 3.7 , 44% female) and four heart-failure patients (age = 60.5 ± 10.8 , 100% male, 50% ischemic and 50% non-ischemic heart disease) using 3T MRI systems (Siemens Healthineers, Erlangen, Germany). All CMR was performed in accordance with a protocol approved by the Institutional Review Board for Human Subjects Research at our institution and informed consent was obtained from all subjects prior to imaging. The adaptive free-breathing method previously implemented on a spiral cine DENSE sequence⁵ with prospective cardiac gating was used with the following parameters: FOV = 200×200 mm² (with outer volume suppression), spiral readout length = 5.6 ms, in-plane spatial resolution = 3.4×3.4 mm², TR = 15 ms, TE = 1.26 ms, slice thickness = 8 mm, and variable flip angle with final $\alpha = 15^\circ$. Four spiral interleaves per image with two interleaves acquired per heartbeat provided a temporal resolution of 30 ms. The displacement encoding frequency and the through-plane dephasing frequency⁸ were set to 0.06 cycles/mm and 0.08 cycles/mm, respectively. 18-30 cardiac frames were acquired depending on the subject's heart rate. Short-axis images at basal, mid-ventricular, and apical levels were acquired for each subject. For each slice, balanced

three-point displacement encoding was used to measure 2D in-plane displacements and perform correction for nonzero background phase⁹.

In addition, the diaphragm navigator-gated sequence⁵ was used to acquire free-breathing images to evaluate how the proposed method performs in comparison to the conventional free-breathing method. Short-axis cine DENSE were acquired at the same slice locations using the same imaging parameters. Breath-hold images were also acquired to serve as reference for comparisons.

4.3.2 Evaluation of deep learning model on adaptive free-breathing cine DENSE

The performance of the DENSE-RESP-NET on adaptive free-breathing images was evaluated on in vivo data using the phase SNR and strain analysis.

The adaptive free-breathing images were reconstructed on an offline MATLAB workstation (MathWorks inc.). The adaptive match-making algorithm was used to subtract the T₁-echo using the matched phase-cycled data⁴. Multiple ste-iNAVs (10-14 depending on the heartrate of the subject) were reconstructed and used to estimate the inter-segment position shifts and to correct the corresponding linear phase errors in k-space. The linear-phase-corrected data were adaptively combined and reconstructed using non-uniform fast Fourier transform^{10,11}. The resulting cine DENSE images, referred to as self-navigated adaptive free-breathing images, were processed by the DENSE-RESP-NET for correction of the signal loss and phase corruption due to constant phase errors.

The phase SNR was measured on diastolic frames of self-navigated adaptive free-breathing images processed using DENSE-RESP-NET, self-navigated adaptive free-breathing images (without DENSE-RESP-NET processing), and diaphragm navigator-gated images according to equation (4.1). The phase SNR value were compared to that of reference breath-hold images using one-way analysis of variance (ANOVA) and a post-hoc Tuckey's test.

$$phase\ SNR = \left\| \frac{mean(\text{phase of mid} - \text{diastolic ROI})}{stdev(\text{phase of end} - \text{diastolic ROI})} \right\| \quad (4.1)$$

In addition to the image-based quality measures, strain analysis was performed to evaluate the proposed method. The DENSE-RESP-NET processed, self-navigated adaptive free-breathing, diaphragm navigator-gated, and breath-hold images were analyzed for strain using the established methods^{12,13}. Segmental circumferential strain from entire cardiac cycle was used in Pearson's correlation analysis and Bland-Altman analysis to measure the agreements between different methods. Analyses were performed separately on healthy and heart-failure cohorts. Since end-systolic circumferential strain is the most commonly reported metric for cardiac strain MRI, we performed Bland-Altman analysis for this parameter. In addition, we used Bland-Altman analysis of early diastolic circumferential strain rate due to importance of this parameter in prognostication of cardiac diseases¹⁴ and since diastolic DENSE images are more affected by the constant phase errors. The Pearson's correlation analysis was not performed on strain values corresponding to a single time point due to challenges with the range restriction in correlation analysis¹⁵.

4.4 Results

Example magnitude and phase images from DENSE-RESP-NET processed self-navigated adaptive free-breathing method in addition to self-navigated adaptive free-breathing images (without DENSE-RESP-NET processing), diaphragm navigator-gated, and the reference breath-hold methods are shown in Figure 4.1 for a healthy subject in panel A and for a heart-failure patient in panel B.

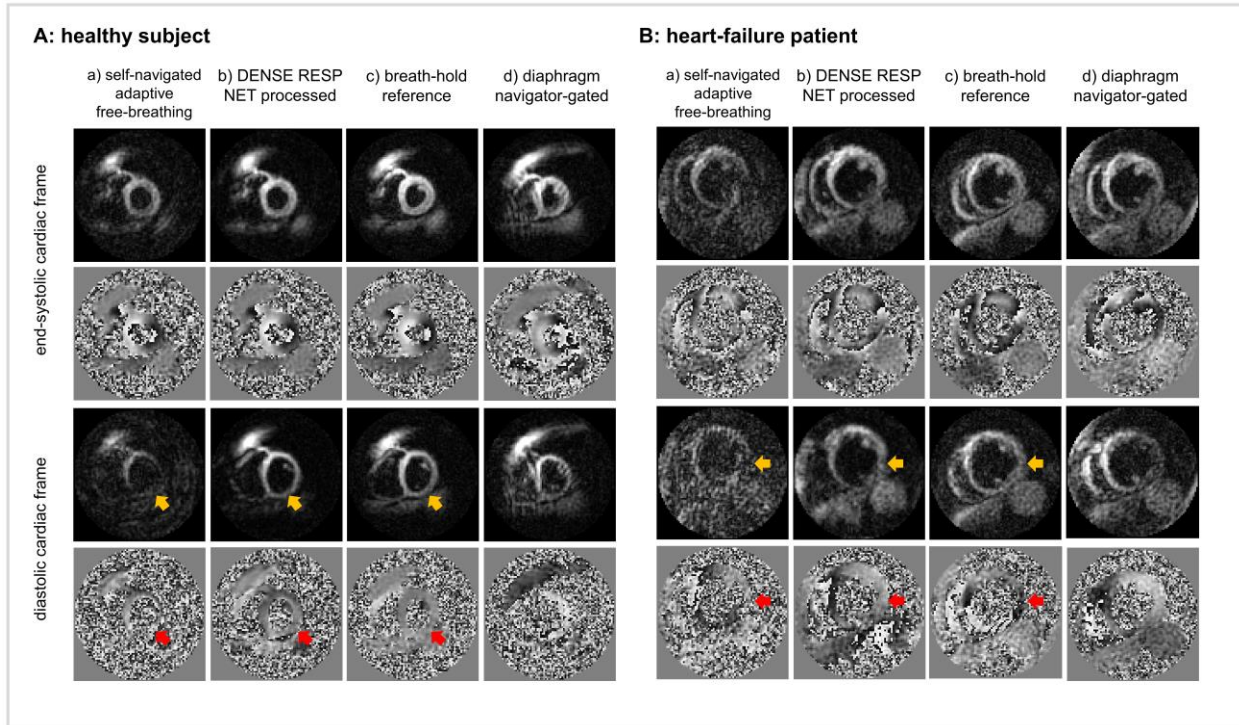


Figure 4.1 - Example magnitude and phase images from self-navigated adaptive free-breathing (without DENSE-RESP-NET processing), DENSE-RESP-NET processed, diaphragm navigator-gating, reference breath-hold images are shown from a healthy human subject (A) and heart-failure patient (B). While end-systolic images show small improvement in DENSE-RESP-NET processed images compared to self-navigated adaptive data, improvement are significant for the diastolic images.

For both healthy subject and the heart-failure patient, the DENSE-RESP-NET processed images show improved image quality compared to self-navigated adaptive free-breathing images without DENSE-RESP-NET processing. The self-navigated adaptive free-breathing images (without DENSE-RESP-NET processing) show signal loss and phase corruption in diastolic magnitude and phase images. DENSE-RESP-NET significantly restored the signal loss and corrected the phase images. The DENSE-RESP-NET produced similar magnitude and phase images to the reference breath-hold images and both methods show significantly better image quality than those of the diaphragm navigator-gated method.

The bar plots in Figure 4.2 summarize the comparisons of the methods using diastolic phase SNR values where separate comparisons were performed healthy (panel A) and patient

(panel B) cohorts. The diastolic phase SNR computed on DENSE-RESP-NET processed images were significantly higher than those from self-navigated adaptive free-breathing images and comparable to those of reference breath-hold data. These results also suggest that both the reference breath-hold and DENSE-RESP-NET processed images have significantly higher diastolic phase SNR compared to diaphragm navigator-gated images.

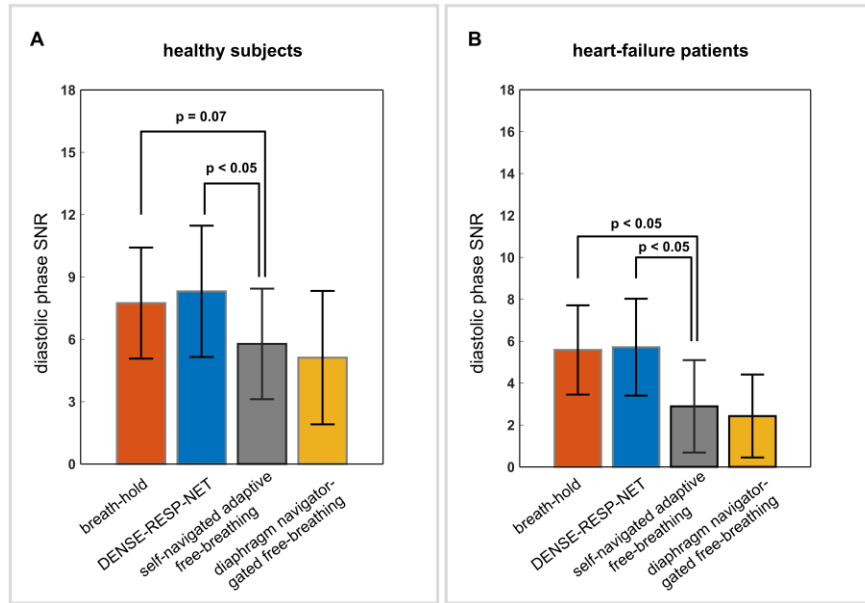


Figure 4.2 – Bar plots of diastolic phase SNR measured according to Equation (4.1) on patients and healthy-subject images. The DENSE-RESP-NET shows significantly better phase SNR compared to the self-navigated adaptive and diaphragm navigator-gated images and comparable values compared to reference breath-hold images. The error bars indicate the standard deviations.

Figure 4.3 and Figure 4.4 shows the Bland-Altman and correlation analysis for circumferential strain computed from DENSE-RESP-NET processed, self-navigated adaptive free-breathing (without DENSE-RESP-NET processing), and diaphragm navigator-gated images compared to the reference breath-hold data for healthy subjects and heart-failure patients respectively.

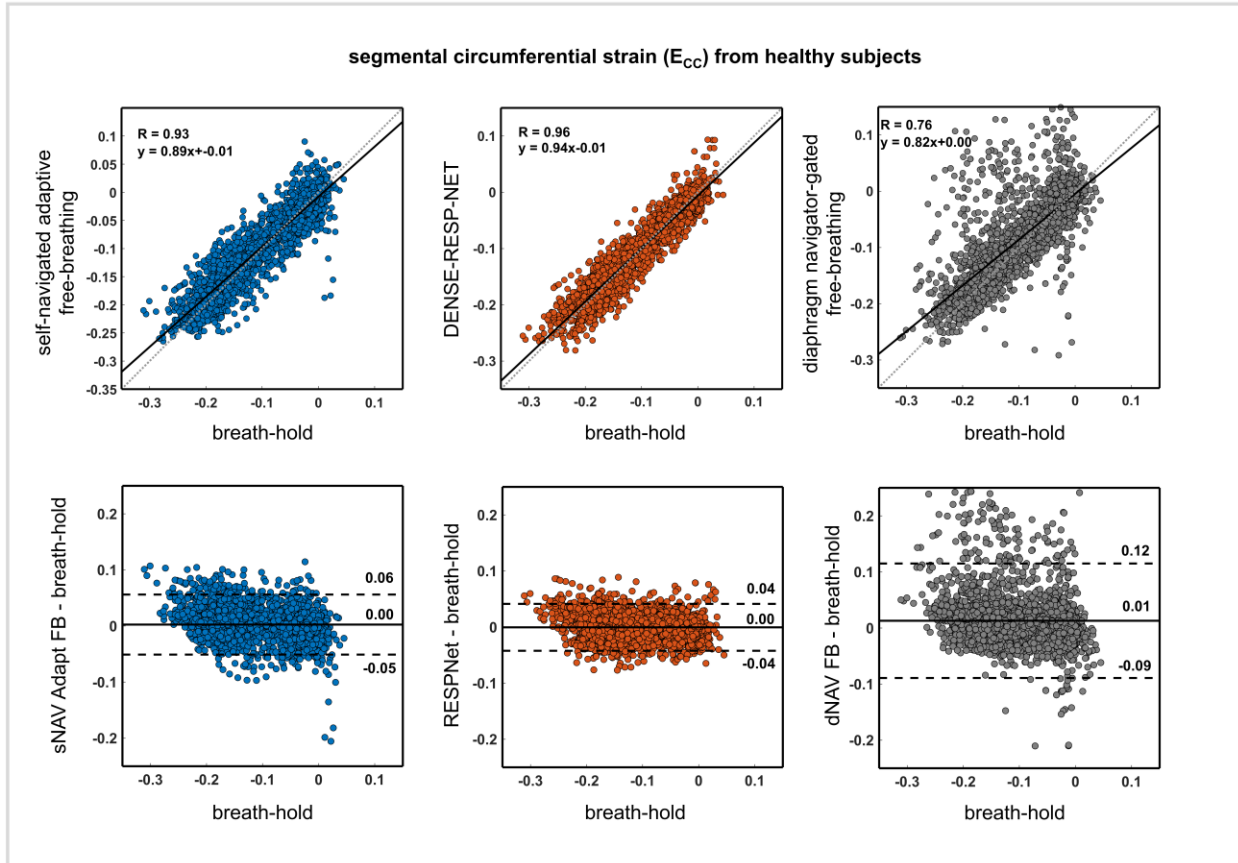


Figure 4.3 – Pearson’s correlation and Bland-Altman analysis show better agreements for segmental circumferential strain (E_{cc}) measured on DENSE-RESP-NET processed images compared to the self-navigated adaptive and diaphragm navigator-gated data in healthy subjects.

In both test groups, strain from DESEP-RESP-NET processed images was more correlated with the reference data ($y = 0.94x - 0.01$; Pearson’s $R = 0.96$ for healthy subjects and $y = 0.81x + 0.0$; Pearson’s $R = 0.85$ for patients) compared to that of self-navigated adaptive free-breathing ($y = 0.89x - 0.01$; Pearson’s $R = 0.93$ for healthy subjects and $y = 0.73x + 0.0$; Pearson’s $R = 0.76$ for patients) and diaphragm navigator-gated methods ($y = 0.82x + 0.0$; Pearson’s $R = 0.76$ for healthy subjects and $y = 0.80x + 0.0$; Pearson’s $R = 0.71$ for patients). The Bland-Altman analysis also shows improved agreement when DENSE-RESP-NET processed strain is compared to the reference data than the other two methods.

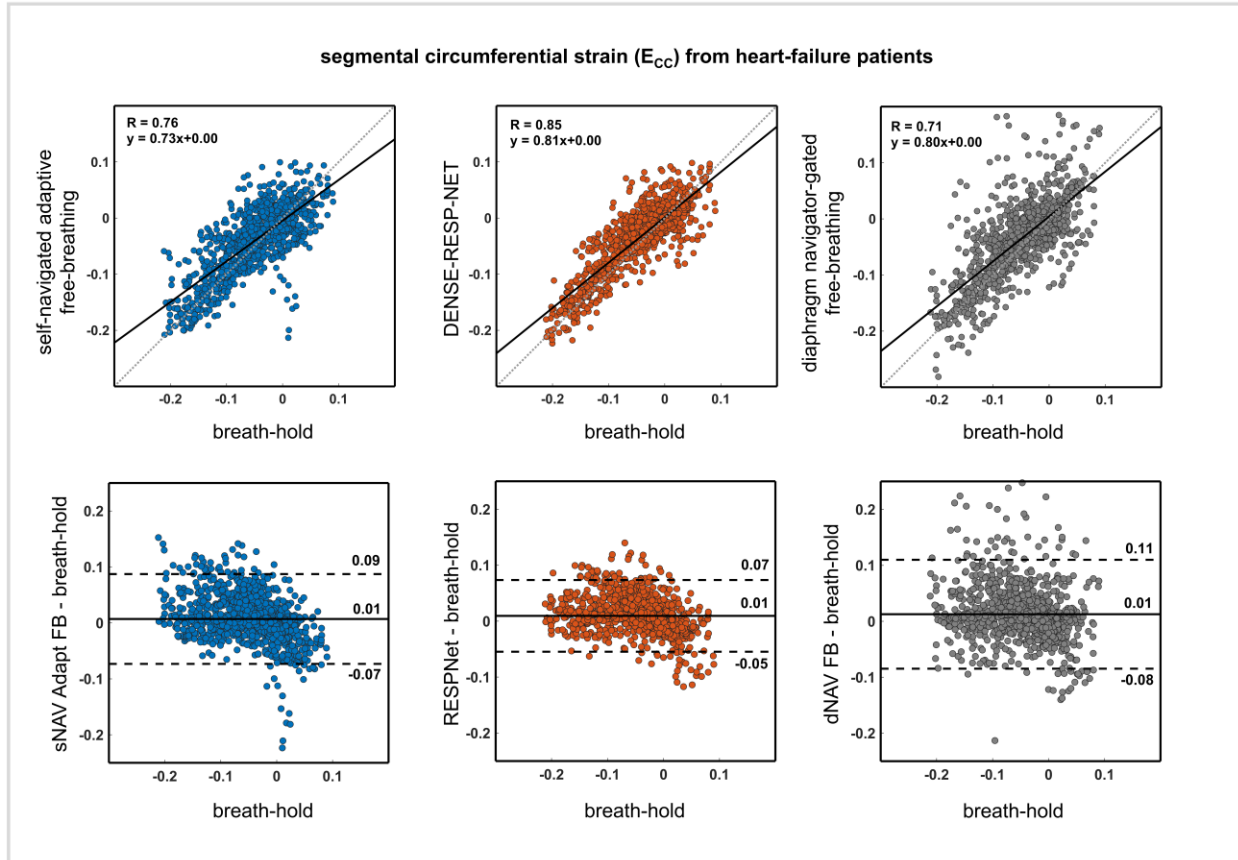


Figure 4.4 – Segmental circumferential strain (E_{cc}) measurements on heart-failure patients show better agreements between DENSE-RESP-NET processed images and reference data compared to those of self-navigated adaptive and diaphragm navigator-gated data using both Pearson’s correlation and Bland-Altman analysis.

Figure 4.5 is the Bland-Altman analysis of end-systolic segmental circumferential strain (panel A) and early diastolic global circumferential strain rate (panel B) from healthy subjects. Figure 4.6 shows the Bland-Altman analysis of the early diastolic global circumferential strain rate from heart-failure patients.

Overall, the strain from DENSE-RESP-NET processed and self-navigated adaptive free-breathing data show better agreement with the reference data compared to strain from diaphragm navigator-gated method. The early diastolic circumferential strain rate from DENSE-RESP-NET for both healthy and heart-failure cohorts shows significantly improved accuracy and agreement compared to the self-navigated adaptive and diaphragm navigator-gated free-breathing data.

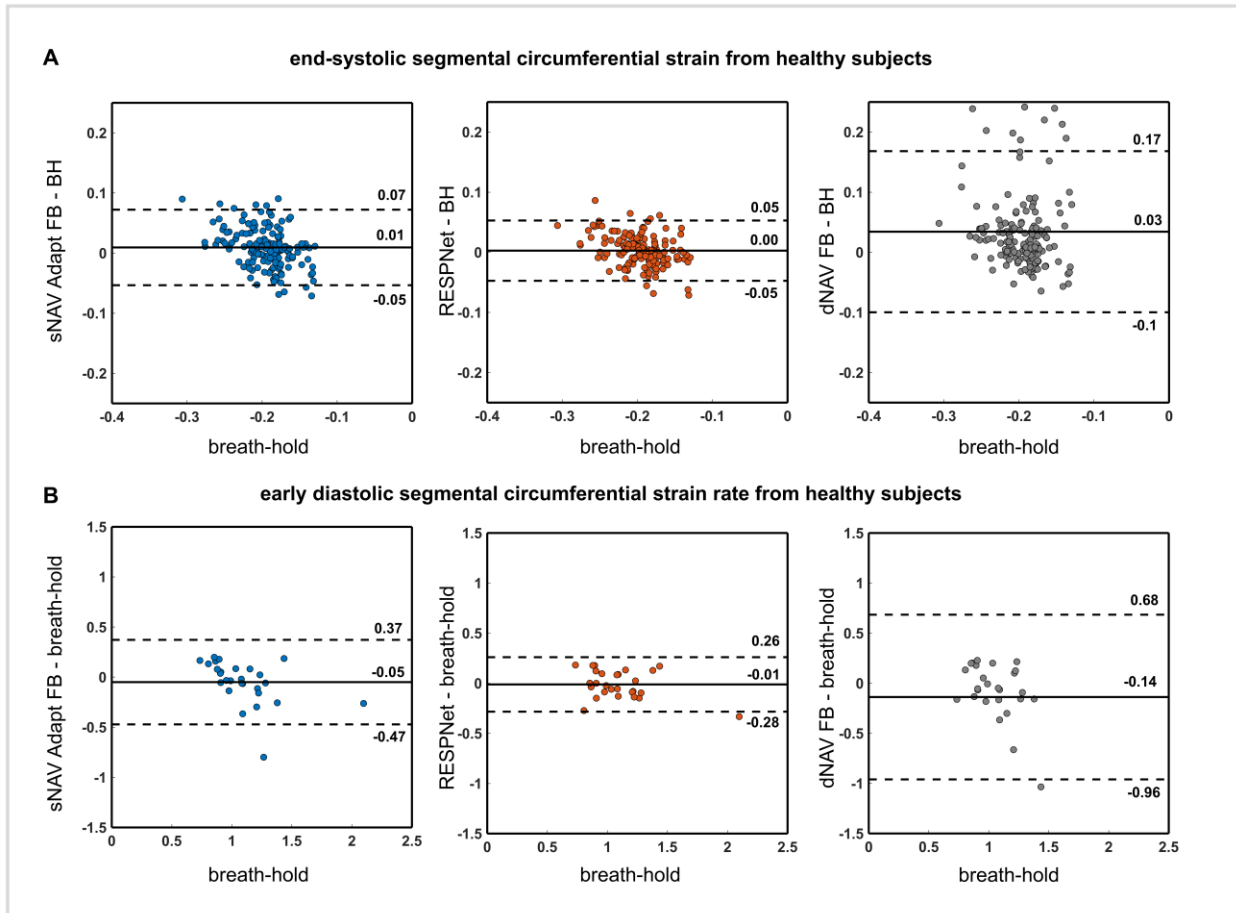


Figure 4.5 – DENSE-RESP-NET significantly improved diastolic measurements. Global early diastolic circumferential strain rate from DENSE-RESP-NET processed data show significantly better agreement compared to those of self-navigated adaptive and diaphragm navigator-gated images on healthy subjects. Self-navigated adaptive images (with or without DENSE-RESP-NET processing) provided more accurate segmental systolic circumferential strain measurements compared to diaphragm navigator-gated images.

4.5 Discussion

We evaluated the trained deep learning model (DENSE-RESP-NET) for correction of signal loss and phase corruption due to respiratory-induced constant phase errors in self-navigated adaptive free-breathing acquisitions. Our evaluations using in vivo data from healthy subjects and heart-failure patients demonstrates that the motion compensated images generated using adaptive free-breathing acquisition for suppression of the T_1 -echo, the self-navigation method for correction of linear phase errors in k-space, and the DENSE-RESP-NET method for correction of constant

phase artifacts show good agreement with the reference breath-hold images for image quality measures and systolic and diastolic parameters.

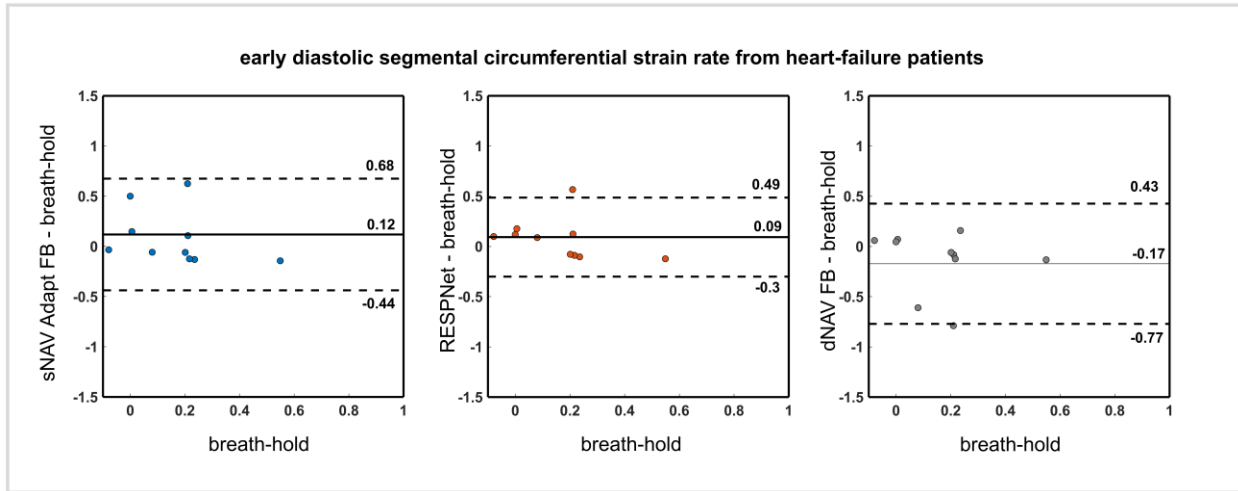


Figure 4.6 – Evaluation of global early diastolic circumferential strain rate on heart-failure patient demonstrates the improved accuracy and agreement in favor of DENSE-RESP-NET compared to other methods.

DENSE-RESP-NET was effective for correction of phase corruption due to the encoding of the respiratory motion into the phase of the stimulate-echo. Diastolic phase SNR and strain measurements shows a very good agreement between the motion compensated free-breathing and breath-hold images and a superior performance compared to free-breathing images without DENSE-RESP-NET processing and the diaphragm navigator-gated methods.

Strain measurements using the self-navigated adaptive free-breathing data with or without DENSE-RESP-NET processing were in a good agreement with the reference measurements for end-systolic parameters on healthy subjects. The DENSE-RESP-NET provide more accurate and better agreement with reference measurements for diastolic parameters compared to data without DENSE-RESP-NET processing. The respiratory-induced constant phase errors are greater in magnitude in diastole compared to earlier cardiac phases and because of this effect, the diastolic self-navigated free-breathing images are more affected by the constant phase artifacts. Our results

demonstrate that DENSE-RESP-NET was effective for compensation of content phase errors in diastole and can provide an effective solution for measurement of diastolic parameters when used in concert with adaptive free-breathing DENSE and self-navigation.

The constant phase artifacts can occur in the diaphragm navigator-gated method as well. Ideally, the acceptance window in diaphragm navigator-gated acquisitions are set to the position of the diaphragm at end-expiration phase of respiration where the respiratory motion in a corresponding cardiac cycle is minimal. However, variations in respiratory pattern during the acquisition can shift the end-expiration baseline to a position where the accepted data are affected by respiratory motion with larger magnitude. This can lead to significant constant phase artifacts and inaccurate strain measurements.

The limitation of this study is the lack of training data from heart-failure patients. Although DENSE-RESP-NET was effective in compensation of constant phase artifacts in healthy subjects and patients, a better and more generalized performance might be achieved by inclusion of data from various cardiac diseases for training. The cine DENSE images used in this study (whether for training or evaluation) were acquired using a one set of acquisitions parameters and only 3T scanners manufactured by a single vendor. A more comprehensive analysis requires cine DENSE images from various magnetic fields, vendors, and acquisitions parameters.

4.6 Conclusion

Motion compensation with DENSE-RESP-NET provides reliable free-breathing cine DENSE for measurement of systolic and diastolic parameters when used in concert with the adaptive match-making acquisitions and self-navigation.

4.7 Reference

1. Kim D, Gilson WD, Kramer CM, Epstein FH. Myocardial tissue tracking with two-dimensional cine displacement-encoded MR imaging: development and initial evaluation. *Radiology*. 2004;230(3):862-871.
2. Ghadimi S, Auger DA, Feng X, Sun C, Meyer CH, Bilchick KC, Cao JJ, Scott, AD, Oshinski JN, Ennis DB EF. Fully-automated global and segmental strain analysis of DENSE cardiovascular magnetic resonance using deep learning for segmentation and phase unwrapping. *J Cardiovasc Magn Reson*. 2021.
3. Auger DA, Ghadimi S, Cai X, et al. Reproducibility of global and segmental myocardial strain using cine DENSE at 3 Tesla: A multicenter study in healthy subjects and heart disease patients. *J Card Magn Reson*. 2022.
4. Cai X, Epstein FH. Free-breathing cine DENSE MRI using phase cycling with matchmaking and stimulated-echo image-based navigators. *Magn Reson Med*. 2018;80(5):1907-1921.
5. Zhong X, Spottiswoode BS, Meyer CH, Kramer CM, Epstein FH. Imaging three-dimensional myocardial mechanics using navigator-gated volumetric spiral cine DENSE MRI. *Magn Reson Med*. 2010;64(4):1089-1097.
6. Pang J, Bhat H, Sharif B, et al. Whole-heart coronary MRA with 100% respiratory gating efficiency: self-navigated three-dimensional retrospective image-based motion correction (TRIM). *Magn Reson Med*. 2014;71(1):67-74.
7. Cai X, Epstein FH. Free-breathing cine DENSE imaging. 2018. <https://patents.google.com/patent/US10830855B2/en>.
8. Zhong X, Spottiswoode BS, Cowart EA, Gilson WD, Epstein FH. Selective suppression of

- artifact-generating echoes in cine DENSE using through-plane dephasing. *Magn Reson Med An Off J Int Soc Magn Reson Med*. 2006;56(5):1126-1131.
9. Zhong X, Helm PA, Epstein FH. Balanced Multipoint Displacement Encoding for DENSE. 2009;988:981-988. doi:10.1002/mrm.21851
 10. Walsh DO, Gmitro AF, Marcellin MW. Adaptive reconstruction of phased array MR imagery. *Magn Reson Med An Off J Int Soc Magn Reson Med*. 2000;43(5):682-690.
 11. Fessler JA. On NUFFT-based gridding for non-Cartesian MRI. *J Magn Reson*. 2007;188(2):191-195.
 12. Spottiswoode BS, Zhong X, Lorenz CH, Mayosi BM, Meintjes EM, Epstein FH. Motion-guided segmentation for cine DENSE MRI. *Med Image Anal*. 2009;13(1):105-115.
 13. Spottiswoode BS, Zhong X, Hess AT, et al. Tracking myocardial motion from cine DENSE images using spatiotemporal phase unwrapping and temporal fitting. *IEEE Trans Med Imaging*. 2006;26(1):15-30.
 14. Ersbøll M, Andersen MJ, Valeur N, et al. Early diastolic strain rate in relation to systolic and diastolic function and prognosis in acute myocardial infarction: a two-dimensional speckle-tracking study. *Eur Heart J*. 2014;35(10):648-656. doi:10.1093/eurheartj/eh179
 15. Goodwin LD, Leech NL. Understanding Correlation: Factors That Affect the Size of r . *J Exp Educ*. 2006;74(3):249-266. doi:10.3200/JEXE.74.3.249-266

Chapter 5 : Summary, Discussion, Limitations, Conclusion

5.1 Summary of the work

This work has presented deep learning methods for suppression of artifacts due to undesired echoes and the respiratory motion in cine displacement encoding with stimulated echoes (DENSE) for myocardial strain imaging.

A deep learning method based on a convolutional neural network was developed and evaluated in the first phase of the project for suppression of the artifact-generating T_1 -echo. The developed model (DAS-Net) was shown to be an effective method for suppression of the strip artifacts due to T_1 -echo in breath-hold data. While conventionally, MR physics-based phase-cycling method¹ is used to suppress the T_1 -echo which requires additional acquisitions, the developed framework eliminated this requirement and shortened the breath-hold scan time by 42% in myocardial strain imaging. To achieve a more generalized performance of DAS-Net for suppression of the T_1 -echo modulated in a range of displacement encoding frequencies, a data augmentation method was developed to generate synthetic DENSE images with arbitrary displacement encoding frequency for training. The feasibility of the data augmentation method was evaluated for situations where availability of training data the desired displacement encoding frequencies is limited. In addition, DAS-Net was shown to significantly outperform the zero-filling method which is routinely used in harmonic phase MRI² for suppression of undesired echoes. Myocardial strain measurements from healthy subjects using non-phase-cycled images processed with DAS-Net showed excellent agreement with the phase-cycling.

In the second phase of this work, a deep learning method was developed for compensation of respiratory-motion-induced signal loss and phase corruption in self-navigated free-breathing cine DENSE³ for myocardial strain measurements. While myocardial motion is measured as phase shift in stimulated echo images, the phase shift due to encoding of the respiratory motion into stimulated echo phase creates error and inaccurate myocardial displacement measurements in self-navigated free-breathing cine DENSE and manifest as signal loss and phase corruption. The artifact due to respiratory-motion-induced phase shifts are unique to stimulated echo imaging and is not accounted for in conventional motion compensation models. We introduced a model using stimulated echo signal that accurately describes this artifact. Phantom experiments and simulation were performed to validate the new model. The accurate description of respiratory-induced phase shifts using the proposed model created a framework for simulation of associated artifacts on breath-hold images. The simulated data were used to develop a convolutional neural network (DENSE-RESP-NET) that can compensate for the signal loss and phase corruptions in self-navigated free-breathing DENSE. The DENSE-RESP-NET was evaluated on self-navigated free-breathing DENSE images from healthy human subjects. Strain measurements from motion compensated images showed significant improvement in measurement of diastolic parameters.

In the last phase of this work, a free-breathing cine DENSE method using adaptive match-making acquisitions⁴, self-navigation³, and the DENSE-RESP-NET processing for compensation of three intrinsic artifacts that arise in free-breathing DENSE was evaluated. Free-breathing images using the proposed methods were acquired from healthy human subjects and heart disease patients in addition to diaphragm navigator-gated images. Image-based quality measures in addition to the strain analysis demonstrated that the proposed method outperform the diaphragm navigator gated method using both image-based quality measures and the strain. The proposed free-breathing

method showed a very good agreement to the breath-hold method for measurement of diastolic and systolic strain parameters. These results suggest that the DENSE-RESP-NET processing used in concert with the adaptive free-breathing acquisitions and the self-navigation is a reliable free-breathing method for myocardial strain imaging

5.2 Discussions

5.2.1 *Artifact-generating T_1 -echo*

In breath-hold cine DENSE, the major source of artifact is the T_1 -echo⁵. Suppression of the T_1 -echo is required for high-quality and accurate strain measurements using cine DENSE. Since the T_1 -echo is not centered in k-space, it creates stripe artifacts in the image domain and leads to inaccurate displacement measurements. The source of T_1 -echo is the relaxation of the longitudinal magnetization after application of the displacement-encoding pulses and because of this, the magnitude of T_1 -echo grows over time during each cardiac cycle⁶. Although the magnitude of the T_1 -echo is negligible for systolic images, it grows to a large magnitude (compared to the stimulated-echo) in diastolic images and adversely affect the diastolic strain measurements especially in those subjects with lower heart-rates. Figure 5.1 shows example DENSE magnitude and phase images before and after T_1 -echo suppression using phase-cycling subtractions. The strain measurement from non-phase-cycling images are unreliable compared to those from artifact free images obtained after phase-cycling subtractions.

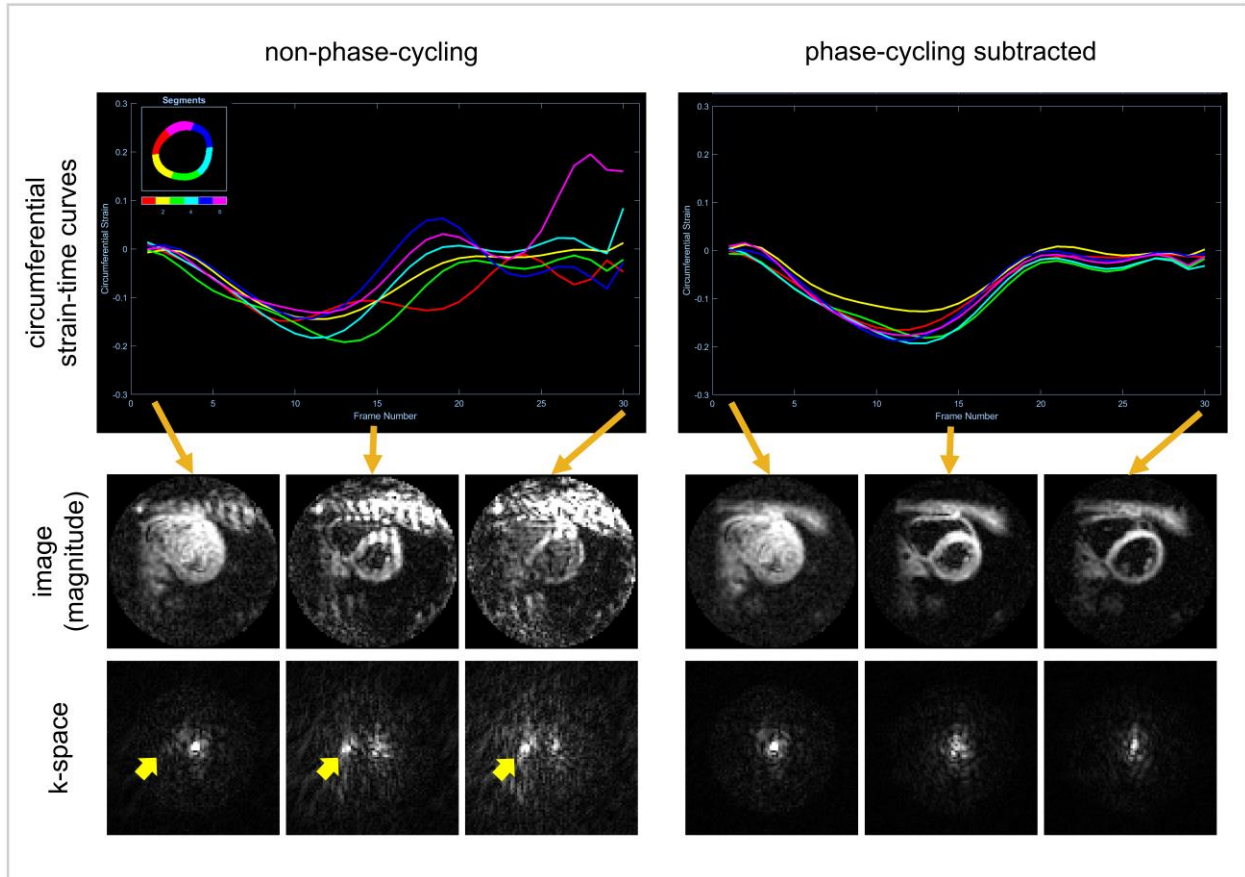


Figure 5.1 – Suppression of the T_1 -echo is essential prior to processing the DENSE images as T_1 -echo adversely affects the displacement measurements. Since the source of T_1 -echo is the relaxation of the longitudinal magnetization, it grows over time during each cardiac cycle and because of this, diastolic images are more affected. Examples of strain measurement from DENSE image before and after T_1 -echo suppression using phase-cycling and the corresponding magnitude and phase images from three different cardiac phases are shown.

Phase-cycling used for suppression of the T_1 -echo is in essence similar to active noise reduction method used in audio domain where noise is measured and an anti-noise signal is generated with a 180° phase shift so that the sum of noise and anti-noise is zero⁷. In phase-cycling, the phase shift in the undesired signal is induced by shifting the phase of second RF pulse in the DENSE pulse sequence¹. Phase-cycling method used in conjunction with the through-plane dephasing has been effective for suppression of the T_1 -echo. However, longer acquisition times due to the acquisition of additional data and susceptibility to motion are limitation of this method. The respiratory or subject's voluntary motion can cause contribution of different tissue in

formation of the T_1 -echo. Because of this reason, it is essential for the phase-cycling acquisitions to have the matched tissue position. For breath-hold scans, this means that the phase-cycled data has to be acquired during the same breath-holding. A typical DENSE protocol requires 14 heartbeat for in-plane displacement measurements including phase-cycling acquisitions. Although, healthy subjects might be comfortable with multiple breath-holds with this duration, it can be discomfoting in heart disease patient. This is especially important for heart disease subjects with lower heart rate as the breath-holds are longer.

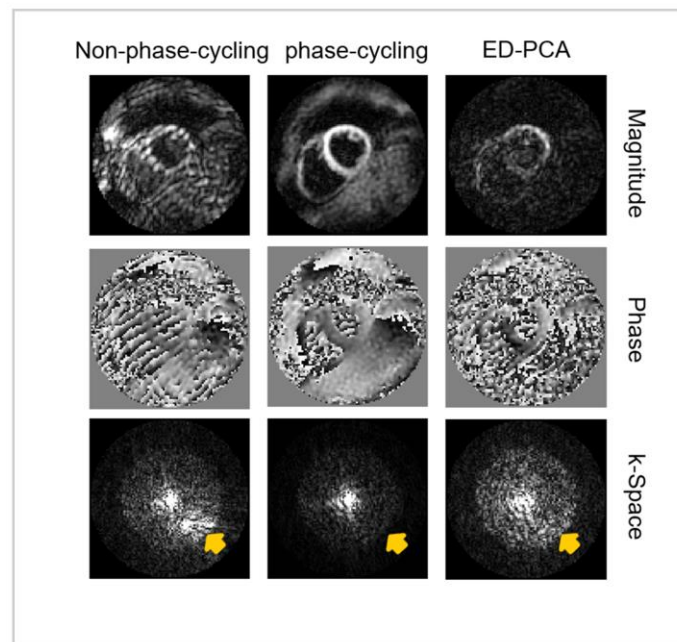


Figure 5.2 – Example magnitude and phase images in addition to k-space data showing the signal separation using ED-PCA method applied on non-phase-cycling images. The performance of ED-PCA is sub-optimal compared to phase-cycling method.

Alternative approach for T_1 -echo suppression include the use of higher displacement encoding frequency or signal separation approaches during post-processing. An appropriately high displacement encoding frequency modulates the T_1 -echo to a frequency outside the readout window⁶. However, higher displacement encoding frequency would induce more phase wrapping in the stimulated echo phase which could be problematic for post-processing of the data. In

addition, measurement sensitivity could decrease with the use of higher displacement encoding frequency. Signal separation methods based on principle component analysis or independent component analysis typically use strong priors⁸ about the signal which leads to sub-optimal performance. Figure 5.2 shows example non-phase-cycling DENSE image processed using the eigenvalue decompositions with PCA (ED-PCA)⁹. The ED-PCA method use the assumptions that the signal to be separates are stationary and non-stationary. While this assumption could approximately hold for the stimulated and T_1 echoes, the performance of the method was sub-optimal compared to the phase-cycling method.

5.2.2 Suppression of T_1 -echo using DAS-Net

DAS-Net is an effective alternative method for suppression of artifacts caused by T_1 -echo. DAS-Net can provide high-quality stimulated echo images from non-phase-cycling acquisitions. For breath-hold acquisitions, T_1 -echo suppression using DAS-Net reduced the scan time from 14 heartbeats to only 8 heartbeats. This reduction in breath-hold acquisition times can significantly reduce the overall scan time in clinical practices and facilitate the strain measurements using DENSE for heart disease patients.

DAS-Net could potentially be used for suppression of residual T_1 -echo artifacts when phase-cycling subtractions are imperfect. In diaphragm navigator-gated images for example, the T_1 -echo could originate from slightly different tissue when a wider acceptance window is used. This may lead to imperfect suppression of the T_1 -echo especially in diastolic frame as shown in Figure 5.3. DAS-Net could potentially suppress the residual artifacts in the reconstructed images. Another potential application of DAS-Net is the T_1 -echo suppressions in free-breathing images. Although match-making method was used in this work for such task, a retained version of DAS-

Net is a potential alternative for suppression of T_1 -echo when applied on per-segment free-breathing data.

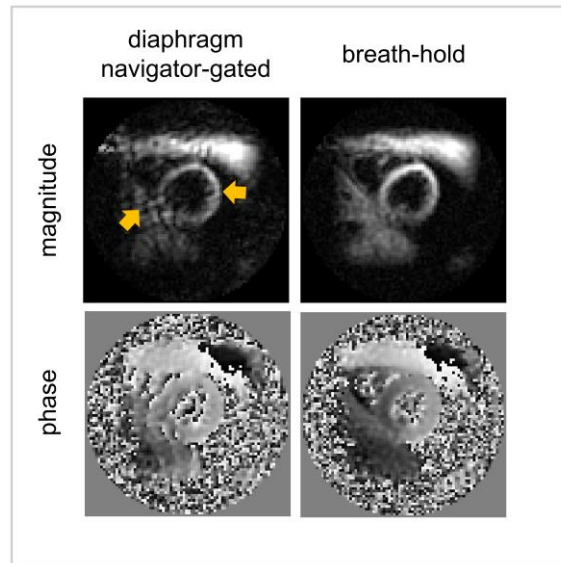


Figure 5.3 – Motion from various sources could lead to imperfect suppression of the T_1 -echo using phase-cycling in diaphragm navigator-gated images. DAS-Net could potentially be used after phase-cycling subtraction to suppress the residual T_1 -echo. Example diastolic images from a diaphragm navigator-gated data shows stripe artifacts - possibly due to imperfect phase-cycling subtractions.

For DAS-Net, a U-Net with 2-dimensional convolution kernels was used to process a single 2-dimensional plane at a time. Since cine DENSE data are basically 3-dimensional (2-dimensional images through time), extension of U-Net with 3-dimensional convolution kernels or recurrent connections, or other architectures such as V-Net¹⁰ incorporate spatio-temporal correlations and could potentially improve T_1 -echo suppressions.

Non-phase-cycling DENSE images used to evaluate DAS-Net were acquired using through-plane dephasing method which selectively induces dephasing onto the T_1 -echo and diminishes its magnitude. Although the through-plane dephasing method could be used for measurement of in-plane displacement with DENSE, this method cannot be used when for 3-dimensional displacement measurement. The T_1 -echo without through-plane dephasing will have

a larger magnitude and extend to a larger area in k-space. For this reason, application of DAS-Net with the current approach in training the model is limited to those cases where the through-plane dephasing of the T_1 -echo is used. A more generalized performance may require re-training the model with images from 3-dimensional displacement measurements or images acquired without through-plane dephasing. Figure 5.4 shows performance of DAS-Net for suppression of the T_1 -echo applied on a DENSE image acquired without the through-plane dephasing gradient.

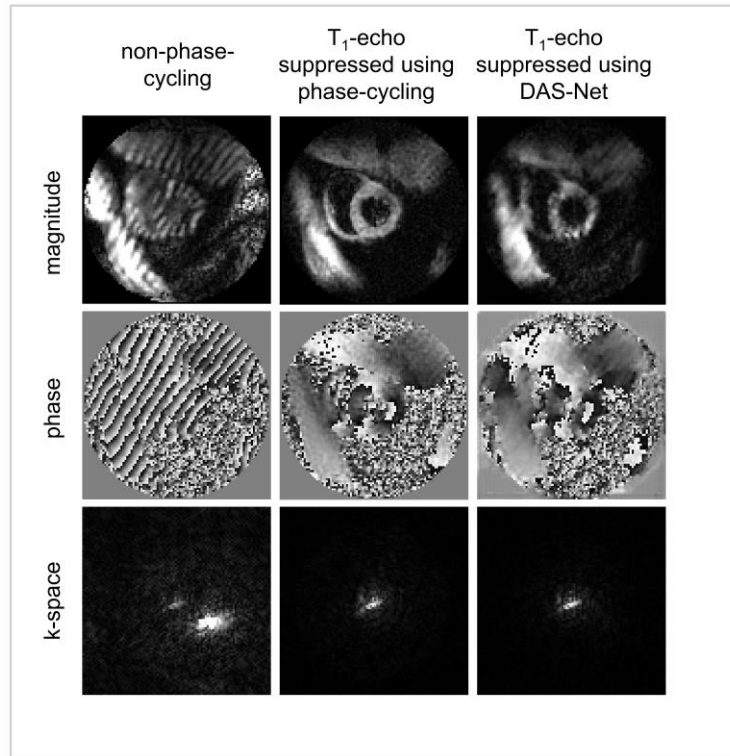


Figure 5.4 – DAS-Net eliminates the need for phase-cycling acquisitions. DENSE images used to train DAS-Net were acquired using through-plane dephasing gradient. Through-plane dephasing method cannot be used for three-dimensional (2-dimensional in-plane and one-dimensional through-plane) displacement measurement in DENSE. T_1 -echo suppression using DAS-Net is shown for a DENSE image acquired without the through-plane dephasing in addition to T_1 -echo suppression using phase-cycling.

5.2.3 Respiratory motion-induced phase shifts

The material displacement result in stimulated echo phase. Although phase shifts due to tissue motion (or deformation) is a desired parameter in DENSE measurements, the phase shift

due to respiratory motion result is undesired and leads to artifacts. In segmented DENSE acquisitions for myocardial displacement measurements, the phase shifts due to myocardial deformation is consistent when different segments of k-space are acquired. However, phase shifts due to respiratory motion vary for each segment during free-breathing acquisitions which leads to signal loss and phase corruptions in stimulated echo images. This artifact is unique to stimulated echo imaging.

The proposed model in Chapter 3 describes the encoding of the tissue motion due to respiration into the phase of the stimulated echo during the time between application of the displacement encoding pulses and the readout. Respiration also causes position shifts in the stimulated echo images. The in-plane position shifts can be estimated using the ste-iNAVs to correct the corresponding errors in k-space. However, the estimated motion may not be used to correct the corresponding phase shifts because: (1) the phase shifts originate from encoding of both in-plane and the through-plane motion as in-plane displacement encoding and through-plane dephasing gradients are both played during the application of displacement encoding pulses, (2) the motion estimation using ste-iNAV does not provide sufficient temporal resolution to accurately correct the phase shifts. The through-plane motion also leads to through-plane position shifts and the corresponding linear phase errors in k-space.

5.2.4 Motion compensations with DENSE-RESP-NET

The DENSE-RESP-NET was an effective method for compensation of signal loss and phase corruption due to respiratory-induced phase shift artifacts. Although these artifacts are negligible for systolic DENSE images, they significantly deteriorate the diastolic images. Both phase signal-to-noise ratio and strain analysis demonstrated that the DENSE-RESP-NET compensation provided more accurate diastolic measurements.

The accurate description of the artifacts using the model in Chapter 3 provided framework for simulation of phase shift artifacts and generation of training data for DENSE-RESP-NET. Alternative approaches for training the model may be to use pairs of free-breathing and breath-hold images. A major challenge with this approach is the unmatched position of heart in input and reference images. Possible solutions are (1) to use image registration algorithms to match the location of heart in the pairs of training data as a pre-processing step, (2) or to use semi-supervised learning methods¹¹.

The semi-supervised learning approach could be used when only a small set of training pairs have matched slices locations. The rest of the training images could be graded depending on the level of degradations due to the phase shift artifacts. The deep learning model can be augmented by inclusion of the additional layer (including fully connected layers) and trained using the graded images as a classification problem. Once the model is trained on a larger dataset, added layers could be removed and the model could be further trained using the small training set with matched slice locations. This approach of semi-supervised learning uses the concept of transfer learning that parameters of the initial layers in convolutional neural networks have smaller variations when the model is trained on different data sets or for different tasks. By training the model on a classification task, the trained initial layers could be used (transferred) to the motion compensation task. The limitation of this approach might be compromised performance compared to supervised learning approaches.

The respiratory-induced phase shift artifacts are not specific to self-navigated adaptive free-breathing DENSE. It can affect the diaphragm navigator-gated images as well, especially when the accept window is not accurately placed on the end-expiration position of diaphragm or when variabilities in respiration pattern shift the end-expiration baseline during acquisition. In

these situations, the signal loss and phase corruption can occur in diaphragm navigator-gated images as well. DENSE-RESP-NET could potentially compensate for these artifacts when used as an extra processing step in image reconstruction. Figure 5.5 shows example magnitude and phase diaphragm navigator-gated images affected by respiratory-induced phase shift artifacts in addition to DENSE-RESP-NET processed data.

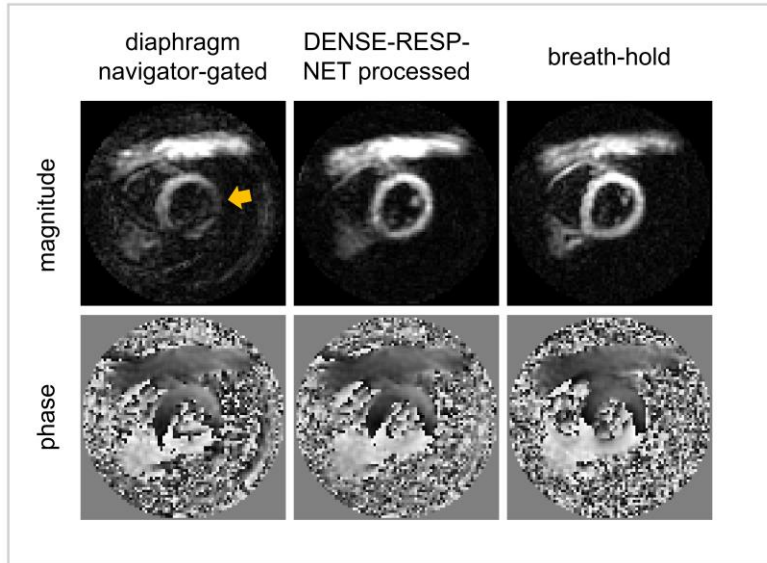


Figure 5.5 – Signal loss and phase corruption can affect the diaphragm navigator-gated images as well as self-navigated adaptive free-breathing images. Example magnitude and phase images affected by these artifacts and the application of DENSE-RESP-NET for motion compensation.

5.3 Limitations of this work

There are few limitations in this work. First, all the imaging was performed on 3T Siemens scanners. Many research and clinical studies are routinely performed on 1.5T scanner due to challenges with stronger magnets such as variabilities in electrocardiogram gating. A more comprehensive analysis of the techniques presented in this work will require inclusion of DENSE images from 1.5T scanners for training and evaluations. For example, DAS-Net trained on 3T DENSE images will most likely have a compromised performance if applied on 1.5T non-phase-cycling images. The T_1 -relaxation times are shorter at 1.5T which means that it can grow to a

larger magnitude when compared 3T. In addition, DENSE images exhibit lower signal-to-noise ratio at 1.5T due to relatively weaker bulk magnetizations. These factors can affect the performance of DAS-Net for T_1 -echos suppressions. For the same reason, evaluation of DENSE-RESP-NET on 1.5T self-navigated free-breathing images may be required. A more comprehensive and representative training data would include 1.5T DENSE images for development of the DAS-Net and the DENSE-RESP-NET. In addition, different vendors use different hardware when manufacturing their MR scanners and this might cause variabilities in the acquired images. DENSE images from various vendors would also be beneficial for evaluations of the deep learning models.

Second, only a single set of acquisition parameters are used for DENSE imaging. Variation in acquisition parameters may result in variations of image features such as resolution, signal-to-noise ratio, signal from other tissues than myocardium (such as blood pool) and etc. An important parameter to consider is the displacement encoding frequency. Although DAS-Net was evaluated for a range of displacement encoding frequencies, DENSE-RESP-NET was evaluated for only a single displacement encoding frequency. The magnitude and temporal variations of the respiratory-induced phase shift artifacts depends on the displacement encoding frequency and because of this, evaluation of DENSE-RESP-NET on DENSE images acquired using other displacement encoding frequency may be required.

Third, both DAS-Net and DENSE-RESP-NET were evaluated on short-axis DENSE images, but not long-axis images. For T_1 -echo suppressions, the characteristics of T_1 -echo in long-axis data may be very similar to those in short-axis images. However, the magnitude of the tissue displacement due to respiration varies in short-axis and long axis directions.

5.4 Future directions

Future work can potentially aim to (1) accelerate volumetric cine DENSE acquisitions by elimination phase-cycling, and (2) accelerate free-breathing cine DENSE acquisitions by combination of motion compensation and multi-band techniques.

In volumetric cine DENSE, the major source of artifacts is the T_1 -echo the conjugate stimulated echo. The phase-cycling approach requires three acquisitions to suppress artifacts attributed to the undesired echoes. The elimination of phase-cycling using DAS-Net in volumetric acquisitions can significantly reduce the acquisition times. In addition, volumetric acquisitions can be combined with compressed sensing method to further reduce the acquisition times. The intrinsic higher signal-to-noise ratio in volumetric DENSE images (compared to 2-dimensional acquisitions) can compensate for the reduction of signal-to-noise ratio due to compressed sensing under-sampling. DAS-Net suppression in conjunction with compressed sensing can potentially enable volumetric acquisitions in a single breath-hold.

The acquisition times in adaptive free-breathing is considerable compared to that of breath-hold acquisitions. In myocardial strain imaging, typically three slices are acquired to assess the ventricular function. The acquisition times for three slices with the current approach may be considerable. A potential approach to alleviate this problem is to combine the adaptive acquisitions with multi-band imaging techniques. In the multi-band acquisition approach, RF pulse is modified to excite multiple slices at the same time. The information corresponding to each slice is phase modulated with a different modulation factor. This approach can be combined with the residual T_1 -echo energy to find phase-cycled data at matched respiratory position. The reconstruction of multi-band images can be combined with motion compensation using the deep learning methods.

5.5 Conclusion

Strain imaging using cine DENSE is accurate and reproducible and provide automatic strain analysis. Application of DENSE for quantification of myocardial global and regional function is increasing. The deep learning methods developed in this work provided faster breath-hold acquisitions and enabled motion compensated free-breathing DENSE imaging with accurate measurements of systolic and diastolic parameters. Evaluation of the motion compensated free-breathing method in heart disease patients suggests that the developed method is promising for utilization in clinical practices.

5.6 References

1. Tsao J, Laurent D. N-SPAMM for efficient displacement-encoded acquisition in myocardial tagging. *Proc 13th Annu Meet ISMRM, Miami Beach, Florida, USA*. 2005;42(6):273.
2. Osman NF, Kerwin WS, McVeigh ER, Prince JL. Cardiac motion tracking using CINE harmonic phase (HARP) magnetic resonance imaging. *Magn Reson Med An Off J Int Soc Magn Reson Med*. 1999;42(6):1048-1060.
3. Cai X, Epstein FH. Free-breathing cine DENSE MRI using phase cycling with matchmaking and stimulated-echo image-based navigators. *Magn Reson Med*. 2018;80(5):1907-1921.
4. Cai X, Epstein FH. Free-breathing cine DENSE imaging. 2018. <https://patents.google.com/patent/US10830855B2/en>.
5. Epstein FH, Gilson WD. Displacement-encoded cardiac MRI using cosine and sine modulation to eliminate (CANSSEL) artifact-generating echoes. *Magn Reson Med*. 2004;52(4):774-781. doi:10.1002/mrm.20232

6. Zhong X, Spottiswoode BS, Cowart EA, Gilson WD, Epstein FH. Selective suppression of artifact-generating echoes in cine DENSE using through-plane dephasing. *Magn Reson Med An Off J Int Soc Magn Reson Med*. 2006;56(5):1126-1131.
7. Elliott SJ, Nelson PA. Active noise control. *IEEE Signal Process Mag*. 1993;10(4):12-35.
8. Hoshen Y. Towards unsupervised single-channel blind source separation using adversarial pair unmix-and-remix. In: *ICASSP 2019-2019 IEEE International Conference on Acoustics, Speech and Signal Processing (ICASSP)*. IEEE; 2019:3272-3276.
9. Zhang Q, Wang J, Wang RK. Highly efficient eigen decomposition based statistical optical microangiography. *Quant Imaging Med Surg*. 2016;6(5):557.
10. Milletari F, Navab N, Ahmadi S-A. V-net: Fully convolutional neural networks for volumetric medical image segmentation. In: *2016 Fourth International Conference on 3D Vision (3DV)*. ; 2016:565-571.
11. Yu Z, Chen L, Cheng Z, Luo J. Transmatch: A transfer-learning scheme for semi-supervised few-shot learning. In: *Proceedings of the IEEE/CVF Conference on Computer Vision and Pattern Recognition*. ; 2020:12856-12864.

Appendix: List of Publications

Peer-reviewed Journal Publications

Abdi M, Cai X, Epstein FH. (in preparation). Free-breathing DENSE using adaptive acquisitions and deep learning-based motion compensation. Target journal: *Magn Reson Med*.

Abdi M, Epstein FH. (submitted). Compensation for Respiratory-Motion-Induced Signal Loss and Phase Corruption in Self-navigated Free-breathing Cine DENSE using Deep Learning. *Magn Reson Med*.

Abdi M, Feng X, Sun C, Bilchick KC, Meyer CH, Epstein FH. (2021). Suppression of artifact-generating echoes in cine DENSE using deep learning. *Magn Reson Med*. 86: 2095– 2104.

Patents

Abdishektaei M, Feng X, Cai X, Meyer CH, Epstein FH. (2020). Method and System for Deep Convolutional Neural Net for Artifact Suppression in DENSE MRI. US 2020/0249306 A1.

Conference Abstracts

Abdishektaei M, Feng X, Meyer CH, Epstein FH. (2019). DAS-Net: A Generative Adversarial Net to Suppress Artifact-Generating Echoes in DENSE MRI. *International Society of Magnetic Resonance in Medicine, 27th Annual Meeting & Exhibition, Montreal, Canada*.

Abdishektaei M, Feng X, Cai X, Meyer CH, Epstein FH. (2019). A Deep Convolutional Neural Net for Artifact Suppression in DENSE MRI. *Society for Cardiovascular Magnetic Resonance, 22nd Annual Scientific Sessions, Bellevue, USA*.

Abdi M, Weller DS, Epstein FH. (2021), Respiratory motion in DENSE MRI: Introduction of a new motion model and use of deep learning for motion correction. *International Society of Magnetic Resonance in Medicine & SMRT Virtual Conference & Exhibition*.

Abdishektaei M, Feng X, Meyer CH, Epstein FH. (2020), Suppression of Artifact-Generating Echoes in Cine DENSE using Deep Learning, *International Society of Magnetic Resonance in Medicine & SMRT Virtual Conference & Exhibition*.